A Thesis Submitted for the Degree of PhD at the University of Warwick

Permanent WRAP URL:

http://wrap.warwick.ac.uk/177973

Copyright and reuse:

This thesis is made available online and is protected by original copyright.
Please scroll down to view the document itself.
Please refer to the repository record for this item for information to help you to cite it.
Our policy information is available from the repository home page.

For more information, please contact the WRAP Team at: wrap@warwick.ac.uk

warwick.ac.uk/lib-publications

Simulations of asymmetry in laser-driven implosions for Inertial Confinement Fusion

by

Alun Robert Rees

Thesis

Submitted to the University of Warwick

for the degree of

Doctor of Philosophy in Physics

Department of Physics

September 2022

Contents

List of Tables

List of Figures

Acknowledgements

Firstly, I would like to thank my supervisor, Tony Arber, for choosing me to undertake this PhD. He has been an excellent mentor and has gone above and beyond to teach, advise and support me throughout my research. Under his supervision, I have had opportunities to present my work internationally at prestigious conferences for which I am incredibly grateful. Above all, I thank him for his patience and kindness, it has been a privilege to work with him during my studies.

In addition, I give my sincere thanks and gratitude to Keith Bennett, who has been fundamental in getting this thesis completed. He has an incredible understanding of computer science and programming that was vital in the maintenance and development of the codes that I used during my studies. I would also like to give wholehearted thanks to Tom Goffrey who was an integral part of carrying out this work. I am incredibly grateful to Tom for always being willing to help me and for his support in finding solutions to the challenges that I faced. He has been a great friend and colleague throughout.

On a personal note, I would like to thank all of the people that encouraged me throughout my research and those who made it a more enjoyable experience. I cannot thank my parents enough for their unwavering love, support and encouragement. Without them I would not have completed this work. Huge thanks also go to other members of family, particularly my siblings; Rhiannon, Gareth, and Rachel, for their enthusiasm and kind words. I also want to acknowledge my late sister Cathryn, who inspired me to pursue this path and whose memory is a constant source of motivation.

I could not have undertaken this journey without my partner, Frances. She

has been my rock throughout and I cannot thank her enough for her encouragement, belief and kindness. During the final year of my study, I had the great fortune of getting engaged to Frances, which I consider to be one of the most wonderful outcomes of the past 4 years. A special thank you goes to her family: Lyndsay, Vaughan, Libby, Helen, and Anna who have all been incredibly supportive and helpful throughout.

From the beginning of this project I have been fortunate to meet and work with some exceptional people who have guided and influenced the direction of my work. Special thanks go to SJ Spencer, Duncan Barlow and Andrew Angus, who provided insightful discussions, technical support and deepened my understanding of the subject. I had the pleasure of collaborating with a number of great people from various institutions: Robbie Scott of CLF, Stuart Morris and Matt Khan of the University of York, as well as Gavin Crow and Ben Williams of AWE.

Finally, I would like to thank my friends for their support, encouragement and for providing welcome distractions from research. A big thank you goes to Osian Shelley, whose conversation always motivated me and reminded me of why I set out on this endeavour in the first place. Many thanks to the friends I have made at Warwick and the CFSA, in particular those that I shared an office with; Aisling, Gethin, Jack, Omstavan, Sam, Shahbaz, and Tish. I would like to acknowledge all the other people in my life; friends from Cardiff, Durham and York for their part in supporting me throughout what has been a challenging, turbulent, but rewarding experience.

Declarations

This thesis is submitted to the University of Warwick in my application for a Doctor of Philosophy degree. The work has been written by the author and not been submitted for any previous applications.

Original work is featured in Chapters 3, 4, and 5. The work presented in this thesis, which includes new implementations to a numerical code, and the generation and analysis of new data through simulation, was carried out by the author except in the cases specified. Plans to extend and publish the work presented in this thesis are set for 2023. Sources have been accredited with citations where figures and results have been reproduced.

This project has been financially supported by the University of Warwick, ESPRC, AWE, and CCPP.

UK Ministry of Defence © Crown Owned Copyright 2022/AWE

COVID-19 Impact Statement

The University of Warwick advises that “students may choose to submit a Covid-19 impact statement alongside their thesis”, and that “Covid-19 statements, not exceeding 600 words, should be submitted to the Doctoral College together with the thesis for examination.”

During the course of my PhD, the world was afflicted by the Covid 19 pandemic. This was an incredibly challenging time and was prominent during my 2^{nd}, 3^{rd} and 4^{th} years of research between March 2020 and January 2022.

Throughout the pandemic, there were obstacles that directly affected my work. The move to working from home meant that access to the computers needed to run simulations was disrupted. It also meant that communication with my supervisors was disrupted, particularly in the description of complex information and graphics. One of the research projects that was lined up as part of my research, to provide simulation support for a series of experiments planned at the Rutherford Appleton Laboratory, was abandoned due to the tragic death of the project lead, Professor David Nealy. In addition, all experiments were either postponed or cancelled entirely during the peak months of the pandemic.

Because of this cancellation, the route of my PhD was altered. My focus changed from running PIC simulations to running hydrodynamic simulations and developing *Odin.* Approximately 9 months of my studies involved working with the *EPOCH* code, testing the new Bremßtrahlung routine and simulating the generation of X-rays in laser foil interactions. I presented this work at the Central Laser Facility Christmas Meeting at Abingdon in 2019. The Bremßtrahlung routine is now implemented into the main code of *EPOCH.*

Abstract

Asymmetries in the implosion in the central-hotspot scheme of direct-drive ICF experiments arise as a consequence of laser nonuniformities such as beam power misbalance, mistiming and laser-target offset. Using the 2D RZ radiation-hydrodynamics code *Odin* [Bennett et al., 2021], a series of ignition-scale direct-drive simulations were conducted to quantify the impact of such nonuniformities on implosion performance for the experimental setup described by [Goncharov et al., 2010]. An applied $l = 1$ perturbation to the laser power was found to be increasingly detrimental to areal density, and other hotspot parameters, as its amplitude, a_p, was raised up to 5%. Laser-target offset, δy, over a range of 5-30μm, was found to have a similarly damaging impact on implosion performance and the results are in agreement with those presented in [Hu et al., 2010]. In both scenarios, this simulation setup showed some tolerance to low levels of nonuniformity, $a_p < 2\%$ and $\delta y < 15\mu m$. For these simulations to be possible, multiple features were added to *Odin* including 3D refractive ray-tracing with face-normal interpolation, *wedge* boundary conditions, and options to include artificial laser power perturbations and laser-target offset.

Simulations were conducted to find the impact of hot-electrons, generated as a consequence of laser-plasma instabilities, on ICF target compression. In the context of a symmetric implosion, we quantified the effect of hot-electrons with differing thermal distribution between 10-60keV, within the range of temperatures found in direct-drive experiments [Rosenberg et al., 2018]. Hot-electrons above 10keV were found to preheat the cryogenic DT fuel and damage the compression of the pellet. A thermal distribution of 30keV hot-electrons was found to reduce the areal density of the hotspot of the target by ∼27% compared to simulations without hot-electrons. Higher temperature populations were found to be more harmful to all metrics of implosion performance up to 40keV, beyond which measurements of hotspot areal density increased from 70% to 73% at 60keV, relative to the value found in a symmetric implosion in the absence of hot-electrons.

Simulations of laser nonuniformities with the inclusion of 30keV hot-electrons were carried out. Hot-electrons of 30keV were found to nullify the harmful impact of $l = 1$ laser power perturbations. In comparison to purely laser-driven simulations, the addition of hot-electrons in laser-offset simulations also showed some resilience to implosion performance with increasing offset. These results indicate that hot-electrons can smooth perturbations caused by non-uniform laser illumination.

Abbreviations

- **ALE** - Arbitrary Lagrangian Eulerian
- **CBET** - Cross Beam Energy Transfer
- **DT** - Deuterium-Tritium
- **EMW** - Electromagnetic Wave
- **EPW** - Electron Plasma Wave
- **HEDP** - High Energy Density Physics
- **IB** - Inverse Bremßtrahlung
- **ICF** - Inertial Confinement Fusion
- **LPI** - Laser-Plasma Instability
- **KH** - Kelvin-Helmholtz
- **NIF** - National Ignition Facility
- **MCF** - Magnetic Confinement Fusion
- **PIC** - Particle-in-Cell
- **RM** - Richtmeyer-Meshkov
- **RT** - Rayleigh-Taylor
- **SBS** - Stimulated Brillouin Scattering
- **SRS** - Stimulated Raman Scattering
- **SSD** - Spectral Smoothing by Dispersion
- **TPD** - Two Plasmon Decay
- **YOC** - Yield Over Clean

Chapter 1

Introduction

Fusion energy is one of the most interesting and complicated challenges in modern science. It is a multi-faceted problem that spans many branches of physics, engineering and material science. Throughout this thesis I intend to guide you through the complexities of the subject and to describe the contribution I have made to this field.

At the time of writing, Fusion has not yet been demonstrated as an energy source. There are a number of challenges to overcome before it is realised. Two of the key obstacles associated with direct-drive Inertial Confinement Fusion, are implosion asymmetry and hot-electrons. Both phenomena degrade the implosion performance, thereby reducing the number of fusion reactions and the energy that can be released. These issues have been studied in detail, both computationally and experimentally, for the current-day direct-drive and indirect-drive experiments. Present-day indirect-drive facilities are at ignition-scale, the most notable experiment is the National Ignition Facility, but direct-drive experiments are yet to reach this stage. For this reason, no significant work has yet been conducted into ignition-scale direct-drive experiments.

Contrary to current facilities, future ignition-scale direct-drive experiments will use higher laser energies and powers, and larger target capsules. In this thesis, I use a 2D radiation-hydrodynamics code, *Odin*, to investigate the impact of implosion asymmetry and hot-electrons and to quantify their impact on ignition-scale experiments, and to see whether or not facilities of this scale can offer more resilience.

1.1 The need for Fusion energy

Throughout our history, new sources of energy have propelled humanity forward and granted us access to advanced technologies and a better quality of life. One of the most significant changes occurred during the industrial revolution in which humanity utilised their knowledge of chemistry to harness the energy from coal, gas and oil buried in the Earth. Humanity is on the verge of another such energy revolution as it harnesses the energy of physical processes: wind, solar, tidal, and nuclear. Many of these sources are well-established and are driving our planet closer to renewable sources of energy. One of these sources, nuclear fusion, is yet to have its potential fully realised.

Nuclear energy utilises the energy stored in the nucleons of atoms and can be released by two methods: fission and fusion. Fission releases energy by deconstructing a heavy element into two lighter elements. Fusion, on the other hand, releases its energy as two lighter elements are fused together. As these nuclei are fused together they create a heavier nucleus, and release energy due to the mass defect of the resulting particles according to $E = \Delta mc^2$. Over the past 70 years, humanity has investigated fusion but have only utilised its energy for destructive purposes. In theory, nuclear fusion has the prospect of providing enough clean energy to sustain the entire Earth and a fuel source so abundant that it could last until the Sun becomes a red giant star. It is an incredibly difficult task that, as of yet, has not been achieved on the scale needed to become a viable energy source.

Humanity faces the greatest threat to its existence in climate change. The global increase in temperature will cause a multitude of problems for the Earth: more droughts and heatwaves, hurricanes will become stronger and more intense, the arctic will likely become ice-free, sea levels will rise by 1-8 feet by 2100 [Frederikse et al., 2020], and crop growth will be hindered by unseasonable weather. Projections estimate that 1.2 billion people could be displaced from their homes by 2050 [Frederikse et al., 2020] as sea levels rise and the local climate becomes inhospitable. Another study [Xu et al., 2020] suggested that the “barely liveable” hotspot zones around the world is currently 1% and is expected to increase to 19% by 2070. The movement of vast numbers of people will put huge pressure on resources and urban infrastructure. Ecological disasters are expected to affect every single country across the globe and natural disasters, such as forest fires and floods, are expected to become more frequent and more severe.

The Energy Information Administration (EIA) projects that there will be a 50% increase in energy consumption by 2050 [EIA, 2021] and the United Nations Department of Economic and Social Affairs predicts that the population will increase to 9.7 billion in this timeframe. Another factor that should be taken into consideration is that an estimated 2.4 billion people [W.H.O, 2021] still rely on burning solid fuels such as wood, coal, charcoal, and bio-waste. These people are predominately located in countries located in Africa, Asia, and South America – regions in which the populations are expected to rise most significantly in the next century. Given the exceptional increase in energy demand and for the Earth's resources, it is imperative that humanity can find a sustainable solution that can benefit and not impede future generations. Within these requirements, renewable energy provides the only viable option.

One of the most attractive prospects of fusion is the immense energy density it holds. Theoretically, a glassful of seawater could provide as much energy as a barrel of oil. Gram for gram, Deuterium, an isotope of Hydrogen that is used in fusion reactions, holds 130 million times more energy than TNT. In addition, seawater is an abundant resource on Earth: 70% of the Earth's surface is water, making it a cheap resource that is accessible to most countries. Deuterium occurs once for every 6,420 Hydrogen atoms, giving it an abundance of 0.0156%, but given the immense scale of the sea, there is plenty to utilise for fusion energy. Despite this, humanity has yet to gain net energy from fusion processes although significant landmarks have been achieved in various aspects. The most promising fusion experiments are the National Ignition Facility (NIF), located at the Lawrence Livermore National Laboratory (LLNL), and the International Thermonuclear Experimental Reactor (ITER) under construction in the South of France. At the time of writing, LLNL has a record 1.35MJ [Zylstra et al., 2022] release of energy and JET, currently the most advanced Magnetic Confinement Fusion (MCF) experiment until the completion of ITER, has a record energy release of 59MJ[Gibney, 2022][Clery, 2022].

Attempts to replicate fusion on Earth are hindered by our inability to replicate fusion found in the Sun's core, which is an example of a gravitationally confined fusion process. The temperature needed to achieve fusion reactions can be estimated as follows. For fusion to occur, two nuclei have to get sufficiently close such that they overcome their electrostatic repulsion and the strong nuclear force can override the Coulomb barrier to fuse them. The distance at which this change in dominant force arises is around, $d \sim 1 \times 10^{-15} m$, at which point the nuclei have a potential energy of:

$$U = \frac{e^2}{4\pi\varepsilon_0 d} \tag{1.1}$$

where e is the electron charge, and ε_0 is the vacuum permittivity. For fusion to occur, the ions need sufficient kinetic energy to overcome this Coulomb repulsion,

$$\frac{3}{2}k_B T > \frac{e^2}{4\pi\varepsilon_0 d} \tag{1.2}$$

where k_B is the Boltzmann constant, and T is the temperature of the ions. By substituting the appropriate values into equation (1.2) we find that it yields a necessary fusion temperature of $T \sim 10^9 \quad K$.

Thankfully, the threshold for fusion reactions to occur is not as high as this. It is not necessary for the entire population of reacting particles to overcome the Coulomb barrier for fusion to take place. In a distribution of particles, some particles in the tail will have sufficient energy to overcome the Coulomb barrier. In addition, quantum tunnelling provides an easier route for fusion reactions to occur, meaning that the necessary separation, d, to overcome is increased. These factors mean that most fusion experiments aim to achieve temperatures of $\sim 10^8 K$.

Throughout this chapter, and throughout this thesis, I will explain the complexities of fusion energy and the pitfalls that are stopping it from becoming a reality.

1.2 Fusion reactions

There are several light element fusion reactions: any element with an atomic number less than that of Iron ($Z = 26$) can participate in fusion reactions, but the reactions with the highest energy per nucleon release are those that involve Hydrogen and its isotopes. In addition to energy per nucleon, we must also consider the likelihood of that reaction occurring. The probability of a reaction taking place is proportional to its cross-section, σ, and these values vary between each isotope. These cross-sections have been measured experimentally [Miley et al., 1974] and we can determine which reactions are most promising for any future reactions. Figure 1.1 shows the cross-sections of the most promising reactions that will be utilised for fusion reactors.

The fusion reactions that are most desirable for experiments are those with the highest cross section. By this metric, Deuterium-Tritium (DT) reactions are best suited for energy production since it has the highest reactivity at the lowest temperatures. The DT reaction, along with its products and the energy release, is shown below:

$$\mathrm{D} + \mathrm{T} \quad \longmapsto \quad {}^{4}\mathrm{He}(3.5\,\mathrm{MeV}) + \mathrm{n}(14.1\,\mathrm{MeV}) \tag{1.3}$$

Unfortunately, Tritium is an isotope that does not exist naturally. It has a half-life of 13 years, and therefore it does not have a stable existence once it is formed. There exists however, a method in which we can obtain more Tritium from fusion reactions and the neutrons that are expelled. By placing a Lithium blanket around the reacting material, it is possible to create more Tritium through

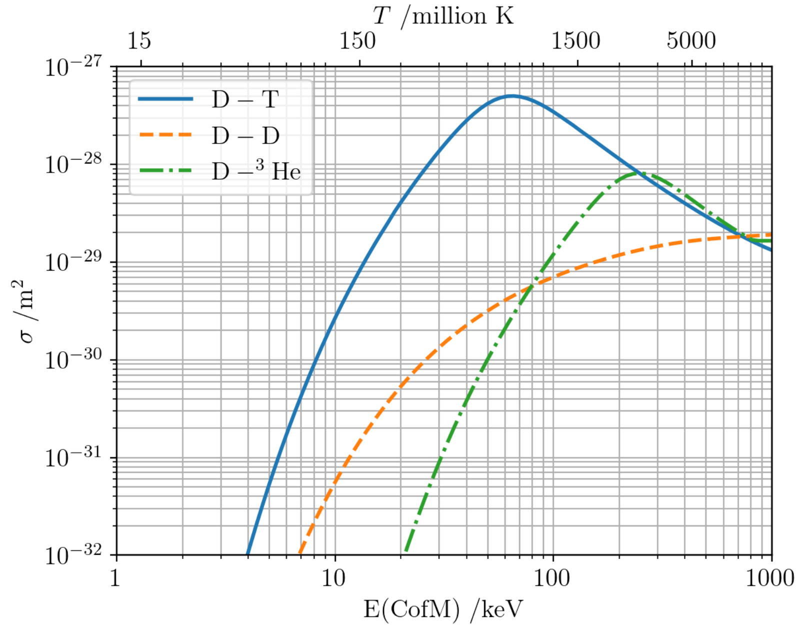

Figure 1.1: Fusion reaction cross-sections as a function of the incident particle energy, for the nuclear fusion reactions. Data provided by the International Atomic Energy Agency's (IAEA) Evaluated Nuclear Data File (ENDF) [Trkov et al., 2018].

the following reaction:

$$n + Li_6 \longmapsto T(2.75\,\text{MeV}) + {}^4\text{He}(2.05\,\text{MeV}) \tag{1.4}$$

There are approximately 89 million tons of lithium left on Earth which if used sustainably, and without significant amounts being diverted to the battery industry, could be utilised for thousands of years [GEO, 2022]. Future reactors will likely utilise the Deuterium-Deuterium reactions, as they also provide a relatively high cross section at lower temperatures and have the bonus of being a stable and abundant isotope of Hydrogen. There are two D-D reactions that can occur, both have approximately equal probabilities:

$$D + D \longmapsto {}^3\text{He}(0.82\,\text{MeV}) + n(2.45\,\text{MeV}) \tag{1.5}$$

$$D + D \longmapsto T(1.01\,\text{MeV}) + p(3.02\,\text{MeV}) \tag{1.6}$$

Standard Hydrogen reactions are not considered for fusion reactors because they rely on the proton-proton chain. The cross-section of this event occurring is so insignificant that they have not been measured experimentally and reactions have a minute probability [Phillips, 1999]. The only reason these reactions are sustainable in the Sun is because of the vast quantities involved and the confinement times of billions of years. These small cross sections are responsible for the longevity of our Sun and the stars across the Universe.

Fusion reactions require extreme conditions to occur; even "low" temperature reactions need temperatures on the order of kilo-electronvolts ($1\text{keV} = k_B/e \times 10^3 \simeq 11,604,525$ K). In nature, these conditions are sustained by the extreme environments of stars and planetary cores. On Earth, this is not possible, and we need to find different ways of replicating these conditions. There are two main avenues of investigation for fusion energy: magnetic confinement fusion (MCF) and inertial confinement fusion (ICF). Any avenue of fusion must bring the interacting nuclei sufficiently close together such that they can overcome the electrostatic repulsion and allow the nuclear force to become dominant, thereby allowing nucleosynthesis to take place. For the purposes of this thesis, we will focus on inertial confinement fusion. For further details on MCF, see [Huang and Li, 2018]. In the following section, the underlying principles of ICF will be described.

1.3 The Physics of ICF

This section will address relevant topics in the order that they appear from a fusion perspective; starting with the requirements of achieving fusion, the mechanisms for making this happen, and the phenomenon that appear during the process.

1.3.1 Fundamental Plasma Physics

In order to understand the state of matter in ICF experiments, we need to understand the fundamental equations that describe them. Plasma contains a sea of free electrons and comparatively heavy ions.

Maxwell's equations are generally presented as a set of four coupled partial differential equations that describe the properties and evolution of electromagnetic fields, $\vec{E}(\vec{x},t)$ and $\vec{B}(\vec{x},t)$.

$$\nabla \cdot \vec{E} = \frac{\rho}{\varepsilon_0} \quad \text{(Gauss' Law)} \tag{1.7}$$

$$\nabla \times \vec{E} = -\frac{\partial \vec{B}}{\partial t} \quad \text{(Faraday-Lenz Law)} \tag{1.8}$$

$$\nabla \cdot \vec{B} = 0 \quad \text{(No Magnetic Monopoles)} \tag{1.9}$$

$$\nabla \times \vec{B} = \mu_0 \vec{j} + \frac{1}{c^2}\frac{\partial \vec{E}}{\partial t} \quad \text{(Ampere-Maxwell Law)} \tag{1.10}$$

The vacuum permittivity and permeability are denoted by ε_0 and μ_0 respectively, c is the speed of light in a vacuum, ρ is the charge density and $\vec{j}$ is the current density.

By considering a slab of plasma in which an electron layer is displaced by a distance δ, we can derive the electron plasma frequency, ω_{pe}. The displacement creates two regions: one of negative charge, where the layer of electrons has moved to, and one of positive charge, where the electrons have left. This charge separation creates an electric field, E, which accelerates the electrons, of charge e, back to their original position with a force:

$$m_e \frac{dv}{dt} = -m_e \frac{d^2\delta}{dt^2} = -eE \tag{1.11}$$

Using Gauss' law (eq. 1.7), the electric field of this displaced electron layer can be derived as $E = \rho\delta/\varepsilon_0 = en_e\delta/\varepsilon_0$. This result yields the following equation:

$$-eE = \frac{e^2 n_e \delta}{\varepsilon_0}, \tag{1.12}$$

where n_e is the electron number density.

This solution takes the form of a simple harmonic oscillator, with a frequency ω_{pe},

$$\frac{d^2\delta}{dt^2} + \omega_{pe}^2 \delta = 0, \tag{1.13}$$

where,

$$\omega_{pe} = \left(\frac{e^2 n_e}{\varepsilon_0 m_e} \right)^{1/2} \tag{1.14}$$

The fundamental time and length scales associated with plasmas are given by the plasma frequency, ω_{pe}, and the Debye length, λ_D. The Debye length is the screening distance beyond which the electric potential of an ion is not experienced by other particles in the plasma.

$$\lambda_D = \frac{v_{th}}{\omega_{pe}} = \left(\frac{\varepsilon_0 k_B T_e}{e^2 n_e} \right)^{1/2} \tag{1.15}$$

In this equation $v_{th} = \sqrt{k_B T_e / m_e}$, is the thermal velocity, T_e is the electron temperature, and m_e is the mass of an electron.

1.3.2 The Lawson criterion

The Lawson criterion [Lawson, 1957] defines the threshold condition needed for fusion energy to have a positive net return when the power losses are accounted for. It also includes some of the output power which is fed back into the plasma to maintain the fusion reaction. This is only possible in MCF. If the energy feedback is ignored, then the Lawson criterion is known as the ignition criterion. Certain fusion experiments take place in a very short timeframe, $\sim ns$, therefore the particles (alpha particles and neutrons) do not have time to deposit their energy back in to the system. To derive the ignition criterion, we consider the losses, both radiative and convective, and the timescale on which they occur:

$$\tau = \frac{W}{P_{loss}} \tag{1.16}$$

The confinement time, τ, is the timescale on which energy is contained in the system and is defined by the ratio of the thermal energy, W, and the power losses, P_{loss} per unit volume of the plasma. The thermal energy of the plasma is defined as:

$$W = \frac{3}{2}k_B\big(n_eT_e + (n_D + n_T)T_{ions}\big) \tag{1.17}$$

Where n_i is the number density for that species of particle, and T_i is the temperature.

If we assume that the ions and electrons are in thermal equilibrium, i.e., that $T_e = T_i$, and that the plasma is quasi-neutral ($n_e \simeq Zn_i$) and $2n_e = n_D = n_T$, then we can simplify the above expression as:

$$W = 3n_ek_BT \tag{1.18}$$

Note that quasi-neutrality states that for a region of the plasma, greater in size than the Debye length, λ_D (eq. (1.15), there is no net charge imbalance.

The number of reactions occurring per unit volume is given by:

$$R = n_Dn_T\langle\sigma v\rangle = \frac{1}{4}n_e^2\langle\sigma v\rangle \tag{1.19}$$

where σ is the fusion cross section and v is the relative velocity of the ions.

The average cross-section over the Maxwellian velocity distribution is:

$$\langle\sigma v\rangle \sim \int vf(v)\sigma(v)dv \tag{1.20}$$

For the ignition state, we require that the rate of heating exceeds the power loss rate. The rate of heating per unit volume is defined as the product of the fusion rate, f, and energy per reaction, E_{DT} and must satisfy the condition:

$$fE_{DT} \geq P_{loss} \tag{1.21}$$

By applying the result of equation 1.19, we find:

$$\frac{1}{4}n_e^2\langle\sigma v\rangle E_{DT} \geq \frac{3n_e k_B T}{\tau_E}. \tag{1.22}$$

We can rearrange this to get the standard Ignition criterion, the threshold value for the product of the plasma electron density, n_e, and the energy confinement time, τ_E:

$$n_e\tau_E \geq \frac{12}{E_{DT}}\frac{k_B T}{\langle\sigma v\rangle} \tag{1.23}$$

substituting typical values for these parameters, a value of $n_e\tau \simeq 10^{15} scm^{-3}$ is found.

This equation highlights that the two most important parameters to consider for fusion reactions to take place during the confinement of a plasma are density and confinement time. It is these two variables that split humanity's efforts of achieving fusion energy on Earth. MCF seeks to sustain the plasma at a relatively low density ($n_e \sim 10^{14}\ cm^{-3}$) for extended periods of time ($\tau \sim 10s$) using a series of magnets to confine the plasma in a torus reactor known as a tokamak [Zohuri, 2017]. Whereas Inertial Confinement Fusion (ICF) seeks to confine the fuel to very high densities, ($n_e \sim 10^{26}\ cm^{-3}$), on the timescale of the inertial movement of the plasma, $\tau \sim 10^{-11}$ s. Note that these numbers assume a Lawson criterion of $n_e\tau \sim 10^{15}\ s\ cm^{-3}$.

1.3.3 Areal density

The criteria for having net positive energy from fusion reactions is described by the Lawson criterion, but for the purposes of ICF we can re-arrange this for a spherical target. Consider the disassembly time, τ_C, of the hotspot at peak compression. Assuming that the plasma is free to expand into a vacuum, the disassembly time can be approximated as [Martínez-Val et al., 1993]:

$$\tau_C \simeq \frac{R_f}{4c_s} \tag{1.24}$$

where R_f is the radius of the hotspot, and c_s is the speed of sound in the target. For fusion to occur, we need alpha heating to occur faster than the time it takes for the hotspot to disassemble. By substituting this value into the Lawson criterion equation, we get:

$$n_0\tau_C \simeq n_0\frac{R}{4C_s} = \frac{\rho}{m}\frac{R}{4c_s} \tag{1.25}$$

where n_0 is the electron number density. If we assume a standard value of $n_0\tau_C = 2 \times 10^{15}\ s/cm^2$ we can rearrange the equation to set a threshold value for the areal density, ρR of the hotspot:

$$(\rho R)_h \geq 0.3g/cm^2 \tag{1.26}$$

It is also necessary to consider the burn fraction, Φ, of the target and how efficiently it will release energy [Atzeni and ter Vehn, 2004]. To derive this quantity, we consider a 50-50 mixture of Deuterium and Tritium, and consider the rate at which fusion reactions, N_{fus} are taking place:

$$\frac{dN_{fus}}{dt} = \langle\sigma v\rangle_{DT} n_T n_D V(t) \tag{1.27}$$

where $V(t)$ is the volume of the burning fuel at time t. Assuming equal numbers of Deuterium and Tritium ions in the fuel mix, the total fuel number density is given by $n_0 \simeq 2n_T = 2n_D = \rho/m_f$, where m_f is the mass of the fuel. We can substitute these values into the equation above to simplify it,

$$\frac{dN_{fus}}{dt} = -\langle\sigma v\rangle_{DT}\Big(\frac{n_0^2}{4}\Big)V(t). \tag{1.28}$$

The number of fusion reactions that occur during the confinement time, τ_c is given by,

$$N_{fus} \simeq \langle\sigma v\rangle_{DT}\Big(\frac{n_0^2}{4}\Big)\frac{V_0 R_f}{4c_s} \tag{1.29}$$

And the burn fraction is given by,

$$\Phi = \frac{N_{fus}}{N_{DT}} = \langle\sigma v\rangle_{DT}\Big(\frac{n_0^2}{4}\Big)\frac{V_0 R_f}{4c_s}\Bigg/\frac{n_0 V_0}{2} \tag{1.30}$$

In the low burn regime, the burn fraction is,

$$\Phi = \langle\sigma v\rangle_{DT}\frac{n_0 R_f}{8c_s} \simeq \frac{\rho R_f}{H_B} \tag{1.31}$$

where H_B is the burn parameter,

$$H_B = \frac{8c_s m_f}{\langle\sigma v\rangle_{DT}}. \tag{1.32}$$

An approximate formula for the burn efficiency for inertial fusion applications, in which a large fraction of the fuel is burnt and fuel depletion is not neglected was found by Fraley *et al.* [Fraley et al., 1974]:

$$\Phi = \frac{\rho R}{H_B(T) + \rho R} \tag{1.33}$$

where $H_B(T)$ and has a value of 6.0 g/cm^2 at 30 keV. Note that for $\rho R = 0.3\ g/cm^2$, we only have a burn efficiency of $\Phi = 0.048$. Therefore, a higher areal density is desirable for fusion reactors. Experiments typically aim for a burn fraction of 1/3, meaning an areal density of $(\rho R) \simeq 3.0 \quad g/cm^2$ [Jacquemot, 2017].

1.3.4 Hotspot ignition

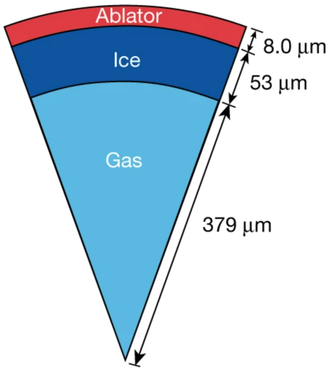

Figure 1.2: Schematic diagram of a typical target used for direct-drive laser fusion. It is a spherical capsule with a shell that consists of an outer CH plastic layer and an inner fuel layer of solid cryogenic DT. The centre of the target is filled with DT gas. Reproduced with permission from [Gopalaswamy et al., 2019].

In theory it is possible to ignite an entire ICF capsule, a scheme known as volume ignition. It is not efficient and cannot provide the necessary gain to balance out the low driver efficiencies of lasers and ion beam accelerators [Rosen, 1999]. To improve the gain and efficiency of ignition, experimentalists aim to achieve ignition using a method called“hotspot ignition”.

Hotspot ignition aims to heat a small region at the centre of the target to the conditions needed for ignition. Spherical targets are ideal because the convergence of the implosion results in better compression, compared to planar and cylindrical targets. Spherical implosions also result in a higher areal density, ρR, for a given change in target thickness.

Once the centre of the target has been compressed it forms a "hotspot", with a characteristic temperature profile, as shown in fig. 1.8. If the plasma has been sufficiently compressed to satisfy the $(\rho R_h) > 0.3\ g/cm^2$ and $T > 5\ keV$ conditions, then fusion will occur. The alpha particles produced from the fusion reactions in the hotspot will heat the surrounding gas DT. If the pressure is sufficiently high, a burnwave will propagate outwards through the DT ice layer of the target. The high density shell of DT ice and CH can provide a higher areal density, (ρR), resulting in a higher burn fraction, Φ, and more heating of the core.

1.3.5 Pellet Compression

Using our value of $\rho R = 3.0 g/cm^2$ to achieve a sufficient burn fraction of $\Phi = 1/3$, we can calculate the necessary mass of a DT spherical pellet needed.

$$M = \frac{4\pi}{3}\rho R^3 = \frac{4\pi}{3}\frac{(\rho R)^3}{\rho^2} \tag{1.34}$$

Substituting our values of ρR and using the density of uncompressed DT fuel, $\rho_{DT} = 0.21 g/cm^2$, we can calculate the mass of this pellet, $m = 2.6 \times 10^3 g$. Such a pellet would release an immense $2.95 \times 10^{14} J$ of energy. Energies of this scale would be catastrophic for any reactor attempting to contain it.

One of the key parameters determining the value of the pellet mass is the density of the DT, ρ_{DT}. If this value were increased, and assuming a fixed value of $(\rho R) = 3.0\ g/cm^2$, the mass of the pellet could be decreased dramatically. By compressing the target, we can increase its density and still satisfy the necessary criteria for fusion [Rosen, 1999]. For a manageable energy output on the order of 500 MJ, the mass requirement is reduced to a few *milligrams* and a corresponding target radius of $R \sim mm$. This requires a compression of $\rho_{comp} \sim \rho_0 \times 1000$. The benefit of using a spherical pellet means that the convergence ratio scales as R^3 as opposed to a cylindrical (R^2), or planar (R^1) compression. For our DT pellet, this equates to a convergence ratio, $CR \geq 20$.

Using the appropriate values of R and C_s, this yields a confinement time, $\tau \sim 10^{-9}s$. There are only a handful of technologies that are able to deliver energy on this timescale, the most useful of which is the laser. It is because of this, that the concept of Inertial Confinement Fusion (ICF) was born [Nuckolls et al., 1972].

1.4 Inertial Confinement Fusion

Inertial confinement fusion uses a driver, such as a laser or particle beam, to rapidly deliver energy to the fuel and cause it to implode and confine the plasma within a hotspot on the timescale of its thermal expansion. Within this definition then there are two main methods that are being investigated: laser direct drive, and laser indirect drive. Both schemes have many similarities but the coupling of the laser energy to the target differs. Note that particle beams have not yet demonstrated the energies or tunability needed to be utilised as drivers for ICF experiments [Kawata, 2021].

1.4.1 Direct-drive

Direct-drive laser fusion uses powerful lasers, up to a few PW, that work to compress a small, *mm* scale, spherical target. The laser beams interact directly with the capsule, ablating the outer CH layer, resulting in an inward force driving the compression of the target as shown in fig. 1.3. Note that the target design is discussed in further detail in section 1.4.3. The laser power profile is designed in such a way as to choose an appropriate adiabat, α, for the compressed material, and to deliver the main pulse at the most effective time. The adiabat is the ratio of the pressure and Fermi pressure,

$$\alpha = \frac{p}{p_F}, \tag{1.35}$$

where the Fermi pressure is given by [Schwabl, 2006]:

$$p_F = \mu\rho^{5/3} = \left[(3\pi^2)^{2/3}\hbar^2 \frac{Z^{5/3}}{5m_i^{5/3}m_e}\right]\rho^{5/3}. \tag{1.36}$$

The importance of the adiabat for ICF implosions is discussed in more detail in section 1.4.4. Within this scheme are many novel ideas of achieving maximum gain and neutron yield, such as shock-ignition [Scott et al., 2021] and shock-augmented ignition [Scott et al., 2020].

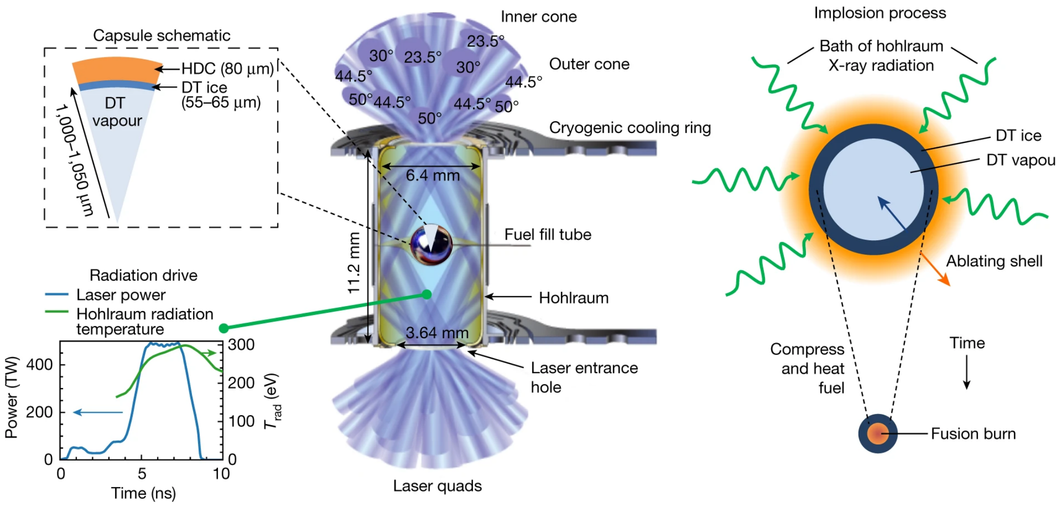

Figure 1.3: Centre, A typical indirect-drive target configuration with key engineering elements labelled. Laser beams (blue) enter the hohlraum through laser entrance holes at various angles. Top left, A schematic pie diagram showing the radial distribution and dimensions of materials in diamond (high-density carbon, HDC) ablator implosions. Bottom left, The temporal laser power pulse-shape (blue) and associated hohlraum radiation temperature (green). Right, At the centre of the hohlraum, the capsule is bathed in X-rays, which ablate the outer surface of the capsule. The pressure generated drives the capsule inward upon itself (an implosion) which compresses and heats the fusion fuel during the implosion process. Reproduced with permission from [Zylstra et al., 2022]

Most fusion involving lasers is done using a Neodymium glass laser (Nd:YAG - yttrium aluminium garnet) which has a transition wavelength of $\sim 1.06\mu m$, which is then frequency tripled, $\omega \mapsto 3\omega$, to a shortened wavelength of $\sim 351nm$ [Treichel et al., 2017]. Higher frequencies are desirable in ICF experiments since they have been shown to reduce undesirable effects such as laser plasma instabilities (LPIs), in addition to increasing desirable effects such as favourable collisional processes and deeper energy deposition [Kato, 1975]. LPIs are discussed in further detail in section 1.6.5.

Since the laser interacts directly with the target, there is a strong dependence on the illumination of the target. An ideal geometrical layout for the configuration of the beams has been derived [Murakami and Nishi, 2017] and is utilised on laser facilities.

1.4.2 Indirect-drive

Like direct-drive, indirect-drive fusion uses powerful lasers to compress a small spherical target. These targets are $\sim \times 1.5$ larger than direct-drive targets since the laser drivers used are more powerful and a thicker ablator is required for this method. As opposed to interacting directly with the target, indirect-drive uses an intermediary medium between the laser and the target as shown in fig. 1.3 [Lindl, 1995]. This is a small, high Z (typically Gold or depleted Uranium), hollow cylindrical canister known as a hohlraum. The lasers enter through *laser entrance holes* at the poles of the hohlraum and interact with its walls. The interaction between the laser and the high-Z material hohlraum causes X-rays to be released. The hohlraum fills with a theoretically uniform "bath" of X-rays that interact with the capsule and compress it in a similar manner to direct drive. X-rays have shorter wavelengths that are preferential to the longer wavelength lasers used in direct-drive for the compression of the capsule, as they can deposit their energy further into the target and can suppress the generation of laser plasma instabilities. By depositing the driver energy further into the target, it can be more efficiently converted to the kinetic energy of the imploding shell. If the X-rays are too energetic, they can permeate through the shell and preheat the fuel which reduces the compressibility of the target.

One of the obvious drawbacks of indirect-drive is that its use of an intermediary medium between the laser and capsule lowers the efficiency of the experiment. Although the conversion of the 3ω Nd:YAG laser to X-rays via the hohlraum can be as high as 80-90% [Olson et al., 2012], this is a significant loss when scaled up to industrial scale, and means that lasers have to be even more powerful to account for this loss. In addition, many of the X-rays do not hit the spherical fuel pellet and the efficiency of the experiment is further reduced.

The targets of indirect-drive experiments are larger than those utilised in direct-drive. These targets need a thicker ablator material which is doped with high-Z material such as Tungsten and Beryllium in order to absorb the M-band spectral lines emitted from the hohlraum [Wilson et al., 1998]. It is necessary to absorb the hard X-rays produced from these spectral lines since they preheat the target.

1.4.3 Target design

An ablative layer is added to the outer surface of an ICF pellet which helps to drive the implosion of the pellet as it is shed. Using this target design, the imploding shell can reach velocities of $v_{imp} \sim 300 - 500\ km/s$ [Craxton et al., 2015].

The material of choice is typically polystyrene (CH) as it can be manipulated to have a low surface-roughness, and as a hydrocarbon it allows for dopant atoms to be introduced to the material [Hu et al., 2008]. Doped ablators are useful for shielding against X-rays, and for increasing the effective density of the shell. CH is a well studied material, meaning its equation-of-state is known in great detail, which means we can accurately simulate this type of target [Clark et al., 2010, Gaffney et al., 2018].

Typically, a layer of cryogenic DT ice is placed on the inner surface of the ablator [Larsen, 1989]. The low temperature of the DT is needed to maximise the implosion and to make the compression as close to adiabatic as possible. High density DT ice surrounds an inner gas fill. This additional density of DT is needed to boost the (ρR) values obtained during experiments and to increase the number of fusion reactions. The combined DT ice and CH layers are known as the target's shell. A diagram showing a slice of a typical ICF capsule is shown in fig. 1.2.

The target has been designed with the low density gas in the centre so that the minimum ignition criteria, $(\rho R) > 0.3\ g/cm^2$ can be easily achieved. Once the centre of the target has ignited, a burnwave (also known as a detonation wave) propagates outwards, thereby triggering further fusion reactions. Note that burnwaves are only generated if a sufficiently large amount of alpha heating occurs behind the shock front [Christopherson et al., 2020]. Once the burnwave reaches the high density DT ice layer, this continues to trigger fusion reactions and allows the ρR value to increase to the necessary value for high fraction burn. If this criterion is not satisfied, a sub-sonic deflagration wave is launched. Deflagration waves cannot provide the necessary heating needed to ignite the remainder of the fuel.

1.4.4 Laser profile design

To achieve the high convergence ratio and high density needed for achieving ignition, it is necessary to consider the conditions of the plasma during the implosion. These criteria put a threshold on the increase in entropy during compression. For maximum compression an adiabatic implosion is needed, compression in which there is no change in entropy, $\Delta S = 0$. Experimentally, this is not possible as radiation preheat, electron preheat, shock-waves, and other sources of heat increase the entropy of the system. It is however, possible to minimise the change in entropy by accurately timing all of the hydrodynamic waves that are sent into the material by the laser.

The entropy of the system is correlated with the adiabat, α (eq. (1.35)). It is possible to shape the adiabat of the target by introducing a short, sharp burst of laser pulse to the target before the main pulse, known as a picket [Anderson, 2006]. A picket drives a shock through the shell of the target. Introducing pickets have been shown to reduce the impact of laser imprint (section 1.6.3) in the early stages of ICF implosions in comparison with main-pulse-only laser drives. Certain laser power profiles employ multiple pickets in order to further reduce the adiabat of compression [Goncharov et al., 2010]. Given a heat capacity ratio, $\gamma = 5/3$, and a planar target, the maximum compression of a monatomic gas is only 4, therefore the multiple shocks produced by the pickets allow further compression. Multiple pickets reduce the growth of shell non-uniformities that are driven by the Rayleigh-Taylor instability [Lindl and Mead, 1975].

1.4.5 Hydrodynamic Instabilities

Hydrodynamic instabilities provide a major obstacle for achieving optimal compression in ICF experiments. There are 3 instabilities of concern: Rayleigh-Taylor (RT), Kelvin-Helmholtz (KH), and Richtmyer-Meshkov (RM).

The most prominent of these instabilities is RT [Richtmyer, 1960], which occurs in a fluid at the interface between regions of different densities. If the denser fluid is accelerated towards the lighter fluid, then the RT instability can seed the growth of perturbations that exist on the surface. In ICF this scenario occurs at 2 stages during the implosion: the acceleration phase, and deceleration phase. These are discussed in further detail in section 1.4.6.

The growth rate of the RT instability in ICF is complex. A numerical solution for the growth rate, based on a self-consistent model, was found as [Takabe et al., 1985],

$$\gamma_{RT} = \alpha\sqrt{kg} - \beta k V_a \tag{1.37}$$

where k is the mode number of the perturbation, g is the acceleration, and V_a is the ablation velocity. α and β are both dimensionless constants that depend on the conditions of the plasma.

Note that the negative term on the RHS of eq. (1.37) shows that there is a stabilising factor ($\beta k V_a$), which if increased, will lower the growth rate of RT. This is known as ablation stabilisation, and the main parameter of interest is the ablation velocity, V_a. This can be controlled by the thickness and material of the ablative layer, and by the laser power profile.

The Kelvin-Helmholtz instability occurs when there is a velocity shear within a fluid or across the boundary of two fluids. The design of ICF experiments does not naturally allow this scenario to occur, but the onset of other instabilities, such as RT, mean that such velocity shears are introduced and become even more problematic due to the KH instability. For further reading on this instability, please see [Harding et al., 2009].

Richtmyer-Meshkov instabilities arise when a shock travels across a perturbed interface between two fluids. As the shock travels through this surface, it becomes distorted resulting in a pressure modulation in the shocked region of the fluid. As the shock is launched into the target, it has a rippled profile and corresponding pressure modulations, which increase in time through the ablative RM instability. For further information on this instability see the following publications [Goncharov et al., 2006, Aglitskiy et al., 2010].

1.4.6 Stages of Implosion

In order to successfully ignite an ICF capsule, a number of high-power laser beams compress the target, causing it to implode. Laser power profiles usually begin with a series of 1-3 low-intensity spikes that last $\sim 0.1ns$, known as pickets (as discussed in section 1.4.4). These pickets act to drive shock waves into the target, thereby compressing it slightly and determining the adiabat for the material during the main stage of compression. After the pickets, the laser power profile rises sharply to the main pulse in which the peak power, $I \sim 10^{15}\ W\ cm^{-2}$ is reached. This pulse is typically sustained for several nanoseconds.

The implosion of an ICF capsule consists of 4 main stages [Craxton et al., 2015]: interaction phase, acceleration phase, deceleration phase, and peak compression as demonstrated in fig. 1.4. Each of these stages for direct drive ignition will be discussed in further detail in the following subsections.

Interaction phase

At the beginning of the experiment, the outer CH layer is solid. The frequency tripled 3ω Nd:YAG laser interacts with it, heating it up. The energy of a single photon is approximately 3.5 eV and is insufficient to ionise the polystyrene layer. By considering the typical electric field strength, E_a, required to strip an electron from its atom, we can calculate the threshold intensity needed for ionisation, also known as the *atomic intensity*, I_a. At the Bohr radius, $a_B = 4\pi\varepsilon_0\hbar^2/(e^2 m_e) = 5.292 \times 10^{11} m$,

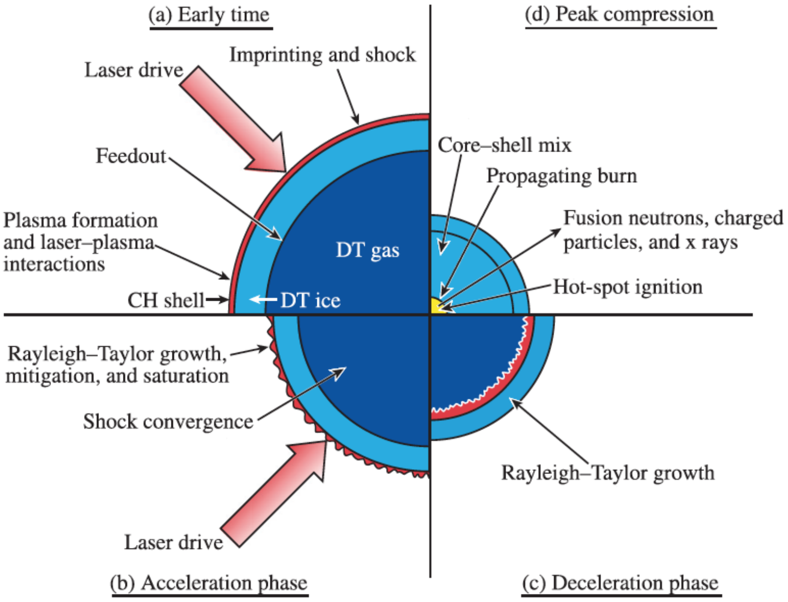

Figure 1.4: Schematic of the four main stages of a direct-drive target implosion. Reproduced with permission from [Craxton et al., 2015]

the electric field strength is:

$$E_a = \frac{e}{4\pi\varepsilon_0 a_B^2} \simeq 5.10 \times 10^9 \ Vm^{-1} \tag{1.38}$$

The strength of the electric field, is correlated with the atomic intensity by,

$$I_a = \frac{\varepsilon_0 c E_a^2}{2} \simeq 3.51 \times 10^{12} \ Wcm^{-2} \tag{1.39}$$

Typical laser systems currently operate at intensities above this threshold, with intensity values of $I \sim 10^{14} - 10^{15} \ Wcm^{-2}$. Therefore, multi-photon ionisation provides a route through which the material can be ionised. Multiple photons arriving at similar times can excite electrons to the energies needed to escape the CH atoms, thereby ionising the material. Note that Nd:YAG is the most utilised laser because it is reliable, well-studied and relatively cheap.

As the laser interacts with the now ionised material, the ablative layer rapidly moves away from the surface of the target and creates a low density plasma around the capsule, as shown in fig. 1.5. The ablated plasma expands further away from the initial surface as the experiment continues. The point at which the ablative layer is travelling away from the capsule is known as the ablation surface. Note that the laser travels through the ablated plasma before reaching the capsule and loses some of its energy through a variety of mechanisms.

Light travelling in a plasma is only able to reach as far as the critical density, n_{crit}; the point at which the frequency of the incident laser is resonant with the plasma frequency, $\omega_l = \omega_{pe}$.

$$n_{crit} = \frac{\varepsilon_0 m_e}{e^2}\omega_l^2 \tag{1.40}$$

Note that this is the case for electromagnetic waves propagating parallel to the surface normal. For rays that have a non-zero angle of incidence, θ_0, the maximum density to which they are able to reach is altered, since the waves are resonant when $\omega_p = \omega_l \cos\theta_0$. Therefore, the turning density of the plasma, n_{turn}, is defined as [Ascoli-Bartoli, 1965]:

$$n_{turn} = n_{crit}\cos^2\theta_0 \tag{1.41}$$

In addition to absorbing the energy of the laser, plasmas refract light as it passes through. The refractive index, η, of a plasma is a function of the frequency of the incoming laser, ω_l, and the electron number density, n_e, and is given by,

$$\eta = \sqrt{1 - \frac{n_e}{n_{crit}}}. \tag{1.42}$$

Characteristically, plasmas have a refractive index between 0 and 1, meaning that light is refracted away from the target normal as it passes through, before bouncing off its effective critical surface. This increases its overall path length and means that more of its energy is delivered to the plasma.

The laser transfers its energy to the electrons predominantly through inverse bremßtrahlung (collisional absorption). This is the process in which a photon is absorbed by an electron in the electric field of an ion. Inverse bremßtrahlung is the dominant mechanism through which the capsule absorbs the laser light. Other mechanisms of energy deposition from the laser to the plasma will be discussed in section 1.5.1. As the laser passes through the ablated plasma, some of the electromagnetic waves couple to the plasma waves and excite laser-plasma instabilities (LPIs) in the process. These are discussed in further detail in section 1.6.5.

Once this initial interaction between the laser and target has occurred, ionising the outer layer, and generating an ablation plasma in the process. The outward ablation causes a reactionary inwards force on the target, thereby beginning the compression phase.

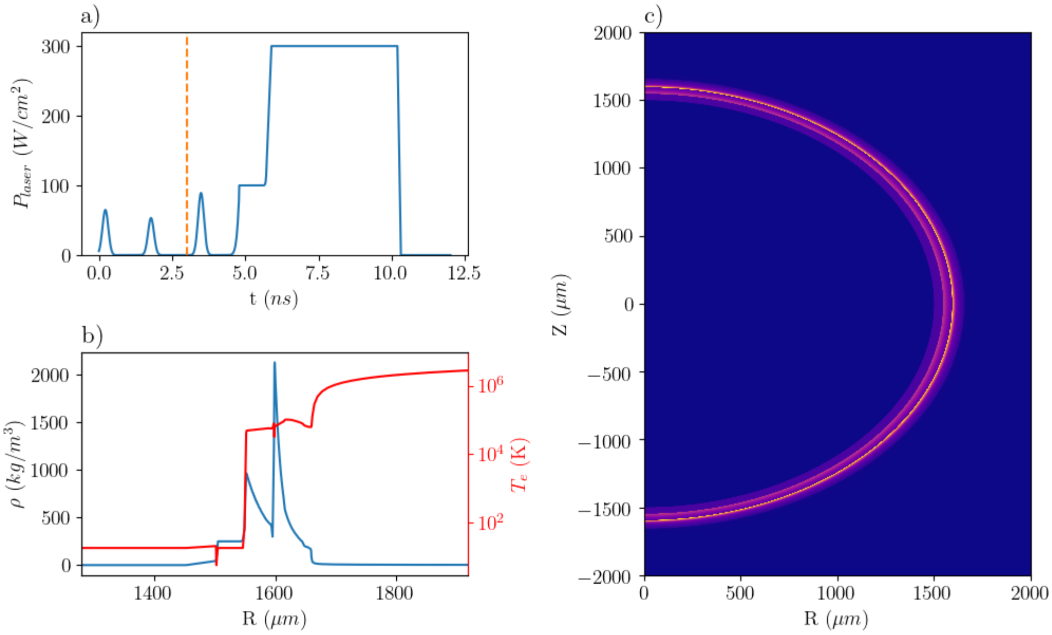

Figure 1.5: A snapshot from a 2D *Odin* simulation at $3.0ns$ showing the interaction stage of an ICF implosion and various aspects; a) laser power profile; b) lineout of the target density and electron temperature profiles; and c) a colour plot of the density profile of the target. Note that plot (c) has a fixed scale, to show the compression scale at the different stages of implosion, and plot (b) has a magnified scale to resolve the features of the imploding shell.

Acceleration phase

The acceleration phase is the first stage of compression. This is the reaction of the shell being accelerated inwards and occurs as a result of the sharp increase in laser intensity during the main pulse, as seen in fig. 1.6. A shock is launched that merges with the earlier shocks generated by the laser pickets. The laser pulse is designed such that this shockwave meets the others at the inner surface of the DT ice layer. Once the shock has reached this interface at the inner surface of the shell, a rarefaction wave moves outwards and the shell begins to accelerate inwards as shown in fig. 1.4(b). During this stage, hydrodynamic instabilities are of great concern. The Richtmyer-Meshkov instability amplifies the presence of any target modulations that exist from target fabrication or irradiation non-uniformities. In addition, the Rayleigh-Taylor instability makes the presence of any ablation surface perturbations, that typically arise from laser non-uniformities (as discussed in section 1.6.1), grow exponentially. The rate at which these ablation surface perturbations grow is dependant on the adiabat, α, of the compressed material. The higher the adiabat, the better the hydrodynamic stability of the implosion, but at the cost of implosion performance.

The laser intensity continues to increase until it reaches a peak value, $I \sim 10^{14} - 10^{15}\ Wcm^{-2}$. At some stage during the main pulse, the main shock overtakes the imploding shell, and reaches the centre of the target.

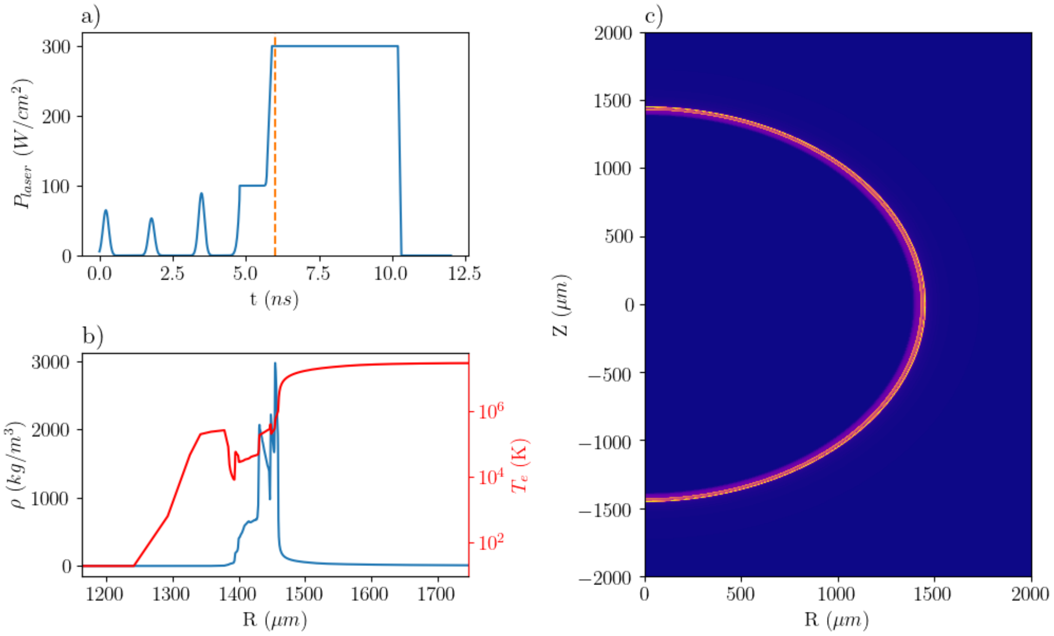

Figure 1.6: A snapshot from a 2D *Odin* simulation at $6.0ns$ showing the acceleration stage of an ICF implosion and various aspects; a) laser power profile; b) lineout of the target density and electron temperature profiles; and c) a colour plot of the density profile of the target. Note that plot (c) has a fixed scale, to show the compression scale at the different stages of implosion, and plot (b) has a magnified scale to resolve the features of the imploding shell.

Deceleration phase

Once the main shock wave has rebounded from the centre of the target, and interacted with the imploding shell, the deceleration phase has begun. An image of a simulation showing typical density and electron temperature profiles is shown in fig. 1.7. The interaction of the shock with the imploding shell, slows the compression down. As the shell decelerates, its kinetic energy is converted into thermal energy and heats the DT fuel. The kinetic energy of the shell, which is proportional to the square of the implosion velocity, i.e $E_K \propto v_{imp}^2$, determines the temperature of the hotspot. Compression of the fuel is dependant on the adiabat and the temperature of the material through compression, a lower adiabat enables higher compression.

During the deceleration phase, the acting force on the shell is outwards, thereby switching the direction of the effective gravity, g. Manufacturing imperfections are amplified by the Rayleigh-Taylor instability, and can be detrimental for achieving optimal compression. As previously mentioned, a higher adiabat can be used to reduce the growth of hydrodynamic instabilities.

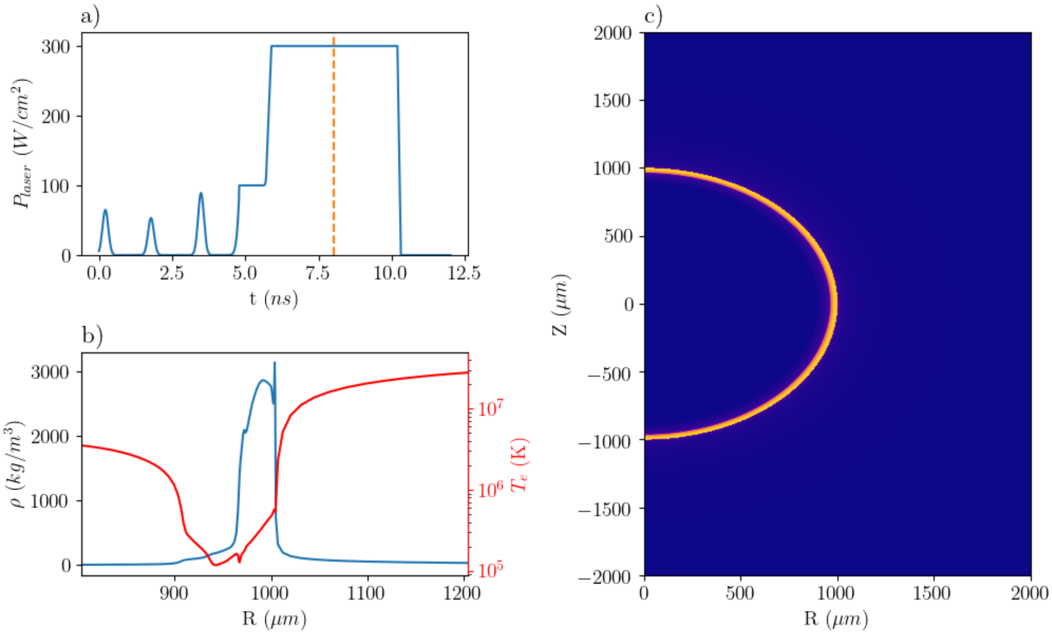

Figure 1.7: A snapshot from a 2D *Odin* simulation at 8.0ns showing the deceleration stage of an ICF implosion from a simulation and different aspects; a) laser power profile; b) lineout of the target density and electron temperature profiles; and c) a colour plot of the density profile of the target. Note that plot (c) has a fixed scale, to show the compression scale at the different stages of implosion, and plot (b) has a magnified scale to resolve the features of the imploding shell.

Peak Compression

Now that the kinetic energy of the imploding shell has been converted to internal energy of the fuel, the temperature of the core increases rapidly. The temperature profile in fig. 1.8 shows a spike at the centre of the target, showing the characteristic hot spot region that is expected from conventional ICF implosions.

If the temperature and density are sufficient, as defined by the Lawson criteria, then ignition will occur and fusion reactions will be taking place in the core. The alpha particles generated by the fusion reactions will deposit more energy in the hotspot of the target, thereby allowing more fusion reactions to take place. If there is a sufficient build up of pressure that can be maintained for long enough, an outwards burn wave will propagate through the high density DT layer, heating the remainder of the fuel and igniting further fusion reactions. If the pressure is not sufficiently high, a sub-sonic deflagration wave will be generated instead.

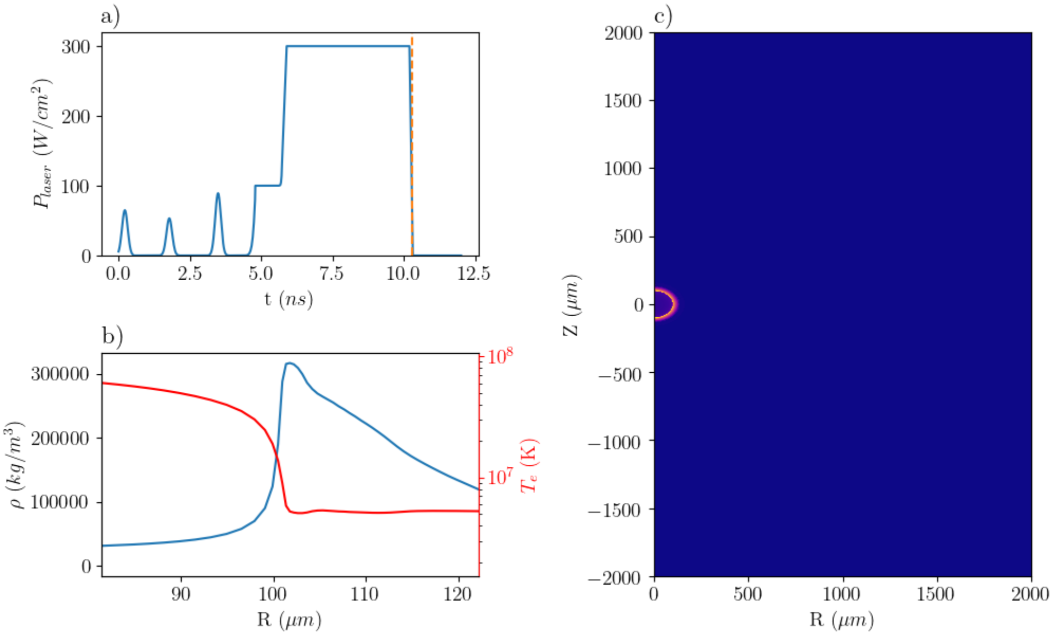

Figure 1.8: A snapshot from a 2D *Odin* simulation at 10.3ns showing the peak compression stage of an ICF implosion from a simulation and different aspects; a) laser power profile; b) lineout of the target density and electron temperature profiles; and c) a colour plot of the density profile of the target. Note that plot (c) has a fixed scale, to show the compression scale at the different stages of implosion, and plot (b) has a magnified scale to resolve the features of the imploding shell.

1.5 Laser Energy Delivery

Once the laser has interacted with the solid CH layer of the target, it will ionise the outer surface and form an ablative plasma cloud. The laser will no longer be able to deposit its energy directly on the surface of the target and will instead reach as far as the critical density, n_{crit}, since the plasma does not allow electromagnetic waves with a frequency, ω, below the plasma frequency, ω_{pe}, to propagate. At the critical density, electromagnetic waves will be reflected or absorbed by resonant absorption. The critical density can be found from the dispersion relation of an EMW in an unmagnetised plasma:

$$1 - \frac{\omega_{pe}^2}{\omega^2} - \frac{k^2c^2}{\omega^2} = 0 \mapsto \omega^2 = k^2c^2 + \omega_{pe}^2 \tag{1.43}$$

where k is the laser wavevector, c is the speed of light in a vacuum, and ω_{pe} is the electron plasma frequency as described in eq. (1.14).

The use of 3ω Nd:YAG lasers in ICF experiments is needed to deliver energy further into the capsule since the critical density is inversely proportional to the square of the laser wavelength. Energy deposition is predominantly done through inverse bremßtrahlung. This mechanism deposits energy most efficiently at higher densities where the collision rate is higher. For the majority of the implosion, the highest densities are found near the critical surface. Shorter wavelengths also aid the energy coupling of the laser to the ablation surface since the distance to the critical surface is reduced. One of the drawbacks of this reduced distance between the critical and ablation surfaces is that thermal conduction cannot smooth laser non-uniformities. Therefore beam smoothing is particularly important for direct drive experiments.

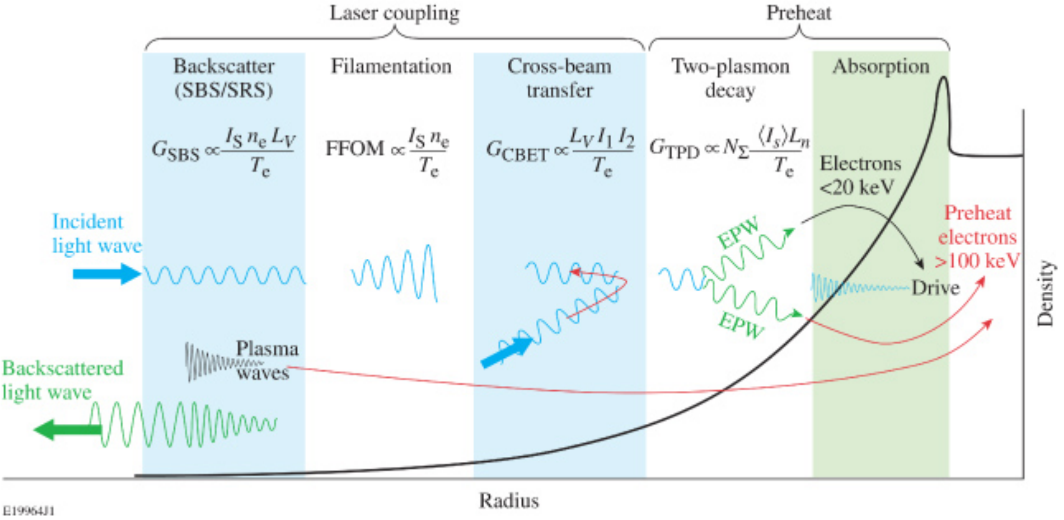

Figure 1.9: Schematic of the direct-drive density profile and potential laser–plasma interactions encountered by incident direct-drive beams. As a result of the relatively low single-beam intensities (I_s), direct-drive experiments are most susceptible to the laser-beam instabilities that are driven by multiple laser beams (e.g. CBET, TPD). Reproduced with permission from [Froula et al., 2012].

1.5.1 Laser energy coupling

To estimate the energy needed to compress an ICF capsule to ignition conditions, we can consider the change in internal energy, ΔU, done during adiabatic compression:

$$\Delta U = P\Delta V \tag{1.44}$$

where P is the pressure at peak compression, and ΔV is the change in volume of the target. Since the compression ratio of ICF implosions is so high, we can assume that the initial volume of the target is substantially larger than the final volume and that $\Delta V = V_{init}$. The pressure of the target at peak compression can be estimated as $P \simeq n_e k_B T_e$. Using parameter values of $n_e \sim 10^{26}\ m^{-3}$, $\Delta V \sim (10^{-3})^3 m^3$ and $T_e \sim 10\ keV$, we approximate the energy needed for compression as $\Delta U \sim kJ$. This is a relatively low energy requirement and can easily be achieved by current laser systems. There are however, complications to consider.

Not all the energy of the laser goes into driving the compression of the target. Some rays will miss the target and most will be reflected off of the critical surface before they can deposit all of their energy. A substantial fraction of the laser is diverted to other avenues. Initially, the outer layer of the target is solid, therefore the first stage is to heat this outer layer. As the outer layer is heated, it becomes ionised, predominantly through multi-photon ionisation, and eventually becomes a plasma [Haines et al., 2020]. Laser energy is also lost to:

- Laser-Plasma instabilities
- Cross-Beam Energy Transfer
- Conversion to 3ω
- Kinetic energy of the ablator

Inverse Bremßtrahlung

For short wavelength lasers, with $\lambda < 0.5\mu m$, the dominant mechanism for energy deposition is inverse bremßtrahlung. This mechanism is responsible for the choice of using 3ω Nd:YAG lasers, since the conversion of laser energy to the ICF capsule is more efficient at this wavelength [Betti and Hurricane, 2016]. In addition, lower wavelengths reduce LPIs and increase hydrodynamic efficiency.

In a plasma, we can consider a sea of free electrons and ions. Electrons in the plasma oscillate in response to the electric field associated with the laser light. Such oscillations promote Coulombic collisions between ions and electrons, thereby converting the laser energy to thermal energy: this is known as inverse bremßtrahlung. Essentially, a scattered electron, in the field of an ion, absorbs energy from the laser.

As the laser light is absorbed by the plasma through inverse bremßtrahlung then the intensity, I, decreases along z according to the differential equation:

$$\frac{dI}{dz} = -\kappa_{ib} I \tag{1.45}$$

where κ_{ib} is the absorption coefficient given by,

$$\kappa_{ib} = \frac{\nu_{ei}(n_c)}{c} \frac{n_e^2}{n_c^2} \left(1 - \frac{n_e}{n_c}\right)^{-1/2}. \tag{1.46}$$

In this equation, ν_{ei} is the electron-ion collision frequency. If we consider the absorption coefficient over a fixed length, l, we can solve the above differential equation using:

$$\alpha_{ib} = \frac{I_{in} - I_{out}}{I_{in}} = 1 - \exp\Big[- \int_0^l \kappa_{ib} dz \Big] \tag{1.47}$$

For the case of an exponentially decaying density profile, $n_e = n_{crit} \exp[-z/l]$ as expected in the case of an ablated plasma, the absorption coefficient is [Kruer, 2003]:

$$\alpha_{ib} = 1 - \exp\Big[- \frac{8}{3} \frac{\nu_{ei(n_c)} l}{c} \Big] \tag{1.48}$$

Resonance absorption

In an underdense plasma ($n_e < n_{crit}$), the dominant form of energy deposition from the laser is inverse bremßtrahlung, but near the critical density the laser can also deposit energy via resonance absorption (RA) [Li et al., 2019]. Through this mechanism, a p polarised electromagnetic wave tunnels to the critical density and couples with a longitudinal electron plasma wave. In this context, p-polarised waves are waves that have an electric field component that is perpendicular to the plane of the interface. In an ICF experiment, rays are refracted by the ablative plasma prior to reaching the critical surface, thereby changing the angle in which the electric field is propagating and making resonance absorption possible.

Early analytic theories of the resonance absorption fraction are given by [Denisov, 1956]:

$$f_{ra} = \frac{1}{2} \phi^2(\tau) \tag{1.49}$$

where ϕ is amplitude of the tunnelled electric field,

$$\phi(\tau) = 2.1\tau e^{-\frac{2}{3}\tau^3}. \tag{1.50}$$

The parameter τ is defined as,

$$\tau = (2\pi L/\lambda_0)^{1/3} \sin\theta, \tag{1.51}$$

where L is the scale length of the critical surface, and λ_0 is the wavelength of the incoming laser.

According to theory, normal incident light should not be able to deposit its energy through resonance absorption, but this is not the case experimentally. It was postulated that the critical surface of an ICF capsule is rippled and allows for a wider range of angles of incidence to effectively deposit their energy through RA [Estabrook et al., 1975]. PIC simulations of this scenario predicted an overall energy deposition of $\sim 15\%$ from the laser due to RA [Estabrook et al., 1975].

As will be discussed later in the laser-plasma instability section (section 1.6.5), the energy of the resonantly excited electromagnetic waves generated from RA can be transferred to hot electrons through Landau damping or wave breaking [Forslund et al., 1975].

1.6 Problems in ICF

At the time of writing, ICF as a source of energy has yet to be realised. Although significant advances have been made in the past decade since the National Ignition Facility began operating, there are still significant challenges that need to be overcome to make fusion viable as described below.

1.6.1 Implosion asymmetry

One of the most damaging issues that limits experiments from reaching their theoretical potential is the asymmetry of the implosions. These asymmetries reduce the (ρR) and T values that are achieved during peak compression, meaning that fewer fusion reactions are able to take place. Therefore, for the purposes of efficiency alone, high implosion symmetry is a desirable attribute to strive for in ICF experiments. Significant drive asymmetry can lead to mixing of materials within the capsule, which can stimulate hydrodynamic instabilities which are fatal for achieving successful implosions [Christensen et al., 2004, Regan et al., 2005]. These non-uniformities can generally be categorised into macroscopic and microscopic non-uniformities, and will be discussed in further detail in the following sections. Significant progress has been made in reducing the sources of asymmetry, however it is still an issue that needs to be resolved.

1.6.2 Macroscopic Non-Uniformities

Successful direct-drive implosions require a high level of irradiation uniformity, to minimise the seeding of hydrodynamic instabilities, which will be described in further detail later in this section. The threshold beyond which irradiation non-uniformities become problematic is as low as 1% rms [Li et al., 2004]. Irradiation uniformity is dependent on a number of factors, including: number of beams, beam geometry, lens f number (the ratio of a lens' focal length and its diameter), beam intensity profile, applied beam smoothing, and coronal plasma conditions.

A model to estimate the magnitude and mode number of irradiation non-uniformities from overlapping beams is described by [Skupsky et al., 1984]. In their calculations, the beams are assumed to have identical, circular intensity profiles in which all beams point towards the centre of the target. This estimate in energy deposition irregularities can be decomposed into its spherical harmonics,

$$\sigma_l = \left|\frac{E_l}{E_0}\right| \left[(2l+1)\sum_{k,k'} P_l(\vec{\Omega}_k \cdot \vec{\Omega}_{k'})\frac{W_k W_{k'}}{W_T^2}\right]^{1/2}. \tag{1.52}$$

And the total rms standard deviation across all l modes, σ_{rms}, is defined as:

$$\sigma_{rms} = \left(\sum_{l\neq 0}\sigma_l^2\right)^{1/2}. \tag{1.53}$$

Note that the $|E_l/E_0|$ term describes the energy deposition from a single beam, E_l, in comparison with the total energy of the laser system, E_0, and contains information about several aspects of the beam including; focus position, f number, beam profile, and target conditions. The terms included in the square brackets are derived from geometrical factors of the beams and contain details such as the number and orientation of the beams (Ω_k) and the beam energies (W_k). The sum is over all beams in the system, and the total energy of the laser is given by $W_T = \sum W_k$, and P_l is a Legendre polynomial.

Although it is possible to obtain a fairly high level of irradiation uniformity, $\sigma_{rms} < 1\%$, with only twenty beams as shown in fig. 1.10, there is an increase in uniformity when more beams are used.

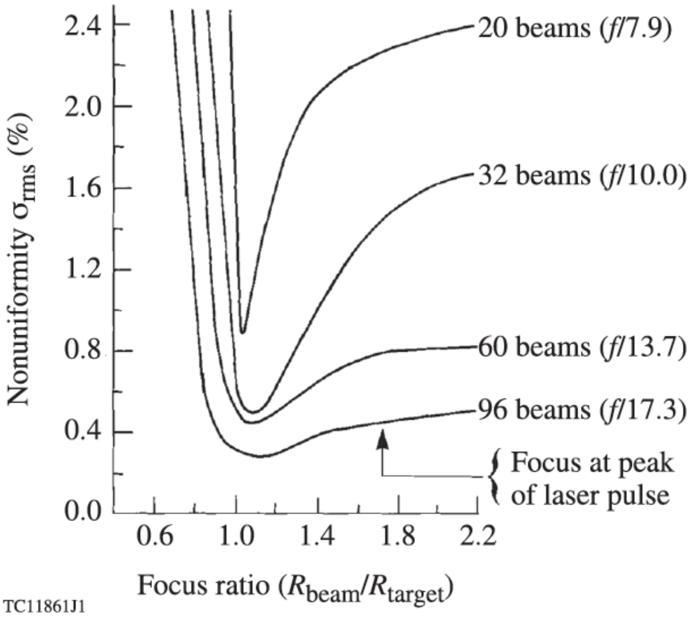

Figure 1.10: Nonuniformity as a function of focus ratio for various numbers of overlapping beams placed uniformly around the sphere. The f numbers of the beam cones are chosen such that the beam cones occupy a total solid angle fraction of 2%. Reproduced with permission from [Craxton et al., 2015, Iwan, 1984]

Laser-target offset

A target chamber of an experimental ICF facility is usually of the order of $\sim 8m$ and can have as many as 192 beams (as is the case at NIF) directed towards a target at its centre. Each laser has a small but finite value in the accuracy of its positioning and its direction. In addition, directly before the experiment begins the DT (or D_2) gas needs to be injected into the target through a mounting stalk. This adds some offset and uncertainty to the positioning of the capsule.

Both factors mean that there is an offset between the laser system and the target they are directed at. If the energy of the laser is not delivered directly then this could introduce a low-mode ($l = 1$) asymmetry to the implosion as well as introducing hydrodynamic instabilities to the implosion. Research conducted by Hu *et al.* using the experimental OMEGA beam configuration suggests that the threshold where offset becomes problematic is 30 μm [Hu et al., 2009].

Laser mistiming

In theory, all laser beams deliver their energy at the same time, however, in practice we know that this is not the case. Although these deviations in timing are small, and have a current specification of $\sim 30ps$, they can have a significant impact on illumination uniformity and seed modulations in the target surface density. Mistiming works to heat certain regions of the target, and imprint laser non-uniformities early than other regions. Although generally considered a source of low-mode modulations ($l < 10$), Smalyuk *et al.* have shown that laser mistiming can also seed high-mode modulations [Smalyuk et al., 2005].

Target smoothness

The importance of target illumination uniformity is also preset in the manufacturing of the targets. Deviations in the thickness of the layers can have a huge impact on the energy deposition and the hydrodynamics of its implosion. Manufacturers are able to manipulate the ablator shell to high levels of smoothness, however the DT ice layer is more problematic [Larsen, 1989]. This region of the shell, on either side of this material needs to be maintained at a constant temperature, at sensitivity levels of $1mK$ [Harding, 2005]. If the DT ice is not maintained at the cryogenic temperature, some of the ice can melt and slump the layer, leading to an increase in thickness. As a result, this layer is prone to surface roughness which can seed hydrodynamic instabilities. Hu *et al.* found that an ice-roughness $\sigma_{rms} < 3\ \mu m$ is required for successful implosions [Hu et al., 2009].

1.6.3 Microscopic Non-Uniformities

Non-uniformities within the beam are often described as microscopic. The perturbations within beams occur as a result of the optics system and the measures taken to mitigate larger scale non-uniformities. In the following section, we outline the implementation of phase plates, spectral dispersion, and polarisation smoothing and their effect on the in-beam intensity profile.

Speckles

The original intensity profiles from the laser as it travels through a circular lens is an Airy pattern. This introduces a low mode perturbation in the energy deposition of the laser as seen in fig. 1.11(a). Lateral thermal conduction works to smooth non-uniformities such as these. The theory behind this was first introduced by

Bodner, [Bodner, 1981], and is known as the “cloudy-day effect”. Perturbations in the ablation pressure, δP, decay exponentially through thermal conduction,

$$\delta P \sim \exp\left(-kD_{ac}\right) \tag{1.54}$$

where k is the wavenumber of the perturbation, and D_{ac} is the distance between the ablation front and the critical surface. Low-mode perturbations ($k < 20$) are problematic and take longer to be smoothed by thermal conduction. eq. (1.54) shows that larger wavenumber, k, perturbations are more strongly damped by thermal smoothing. To remove the large scale variation in the intensity distribution, phase plates are introduced to the beamline [Kato et al., 1984].

As the high-power Nd:YAG laser is frequency tripled, the phase variation in the beam is also tripled, leading to greater distortions and amplitude modulations in the intensity profiles. Phase plates are used to mitigate the effects of these phase variations. The spatial coherence of the beam is broken and it is discretised into beamlets by the phase plate which introduces random phase changes across the plate. Note that current ICF facilities, such as Omega, utilise continuous phase plates, in which the applied phase variation is continuous across the surface [Kessler et al., 1993]. The resulting intensity distribution from applying continuous phase plates to the beamline are shown in fig. 1.11(b).

Once the laser has passed through the phase plates, the large scale variations in intensity profile have been replaced with a highly modulated speckle structure superimposed upon it, thereby achieving the desired result of increasing the perturbation wavenumber, k. This speckle structure is a result of interference between the beamlets due to their phase differences. The high intensity of speckles can cause small-scale perturbations and further excite LPIs. To suppress the problematic effects of speckles, ICF facilities utilise smoothing by spectral dispersion (SSD) [Skupsky et al., 1989].

Bandwidth is introduced to the laser using an electro-optical modulator (EOM). An EOM works by applying an electric field across a crystal (such as lithium niobate), which changes its refractive index in the process. The change of refractive index alters the propagation time of the light as it passes through the crystal, which is directly proportional to the phase. This has the effect of creating sidebands to a monochromatic laser. This bandwidth means that the beams have a phase distribution that changes with time, which combined with the phase plates means that the time-averaged intensity profile of the beam is smoothed. In essence, spectral dispersion works by projecting multiple spectral components, with speckle patterns that are shifted at different times, on top of each other, thereby smoothing the overall intensity pattern and reducing the appearance of individual speckles, as shown in fig. 1.11(c). Note that the OMEGA laser facility at the Laboratory for Laser Energetics, University of Rochester operates with a 2D SSD with a 1-THz bandwidth, and has a non-uniformity of $\sigma_{speckle} \approx 1\%$, which is at the threshold needed for successful ICF compression [Regan et al., 2005]. The improvement in intensity uniformity by applying 2D SSD can be seen in fig. 1.11(d).

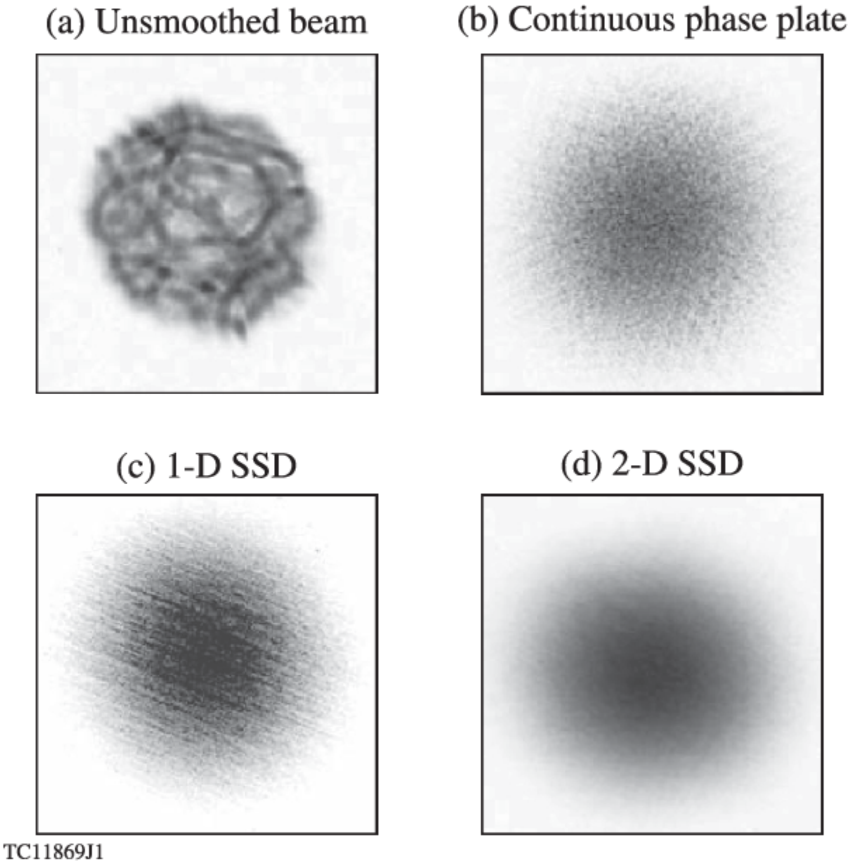

Figure 1.11: Equivalent-target-plane images, integrated over a $\sim$ 1ns pulse width, of a single frequency-tripled OMEGA beam with four levels of smoothing: (a) unsmoothed; (b) continuous phase plate, no bandwidth; (c) bandwidth in one modulator (1D-SSD); (d) bandwidth in both modulators (2D-SSD). Reproduced with permission from [Craxton et al., 2015].

Another method for smoothing the beam intensity distribution is polarisation smoothing [Boehly et al., 1999]. By employing a wedge of birefringent material, such as potassium dihydrogen phosphate (KDP), after the frequency-tripling crystal, the beam can be split into two orthogonal polarisations. The wedge is needed in order to deflect the two different polarised components by varying angles. Since orthogonal polarisations do not interfere with each other, it has the effect of generating two independent speckle patterns and the uniformity of the intensity pattern is reduced by a factor of $\sqrt{2}$. The aim of polarisation smoothing is to smooth out modes of non-uniformity that are not smoothed by SSD.

Laser imprint

Although the methods above improve laser uniformity and reduce the time-averaged intensity of speckles, the illumination within each beam is not completely uniform and causes deviations in symmetric compression. Although dynamic, the small variations in intensity from speckles still exists and are "imprinted" to the target at the early stages. This non-evenly illuminates the capsule and induces small-scale perturbations on the target surface which can evolve through the Rayleigh-Taylor instability during the acceleration phase of compression (see section 1.4.5).

Thermal smoothing of perturbations is described by eq. (1.54). At early times, the distance between the ablation front and critical surface, D_{ac}, is very small and means that small-scale non-uniformities such as those seen in speckles, cannot be smoothed by thermal conduction and are imprinted on the surface of the target. These wavelengths are in the high-gain region of the RT instability and grow very rapidly to distort the ablation surface. As the experiment continues, the distance between the ablation front and critical surface increases, thereby improving thermal conduction smoothing and speckles are not as problematic at this stage.

1.6.4 Asymmetry Overview

Each of these sources of asymmetry are damaging to implosion performance and their impacts have been study to varying degrees. Li *et al.* found that the rms variation in areal density, ρR, was proportional to the rms variation of on-target laser intensity, I, with,

$$-\frac{\delta\rho R}{\rho R} \approx \frac{1}{2}(C_r - 1)\frac{\delta I}{I}, \tag{1.55}$$

where C_r is the capsule convergence ratio [Li et al., 2004]. Further experimental and computational results have confirmed similar results as well as the impact on ion temperatures in asymmetric implosions [Johnson et al., 2018].

All studies of implosion asymmetry in direct-drive have been based on experimental results from OMEGA, or simulations of corresponding laser energies and capsule size. Studies of asymmetries on larger, ignition-scale experiments are centred on the National Ignition Facility (NIF) and model the asymmetries associated with indirect-drive fusion [Casey et al., 2021]. Eventually, direct-drive facilities will be scaled up to NIF size, and it will be important to understand whether these asymmetries become more or less harmful to implosion performance.

1.6.5 Laser Plasma Instabilities

In the coronal plasma of an ICF target, the laser loses a fraction of its energy to Laser-Plasma instabilities through wave coupling. Figure 1.9 shows an overview of the various wave phenomena that occur in the coronal plasma of an ICF capsule. To understand how waves propagate in a plasma it is necessary to consider their dispersion relation. Linear analysis of the hydrodynamic equations of an unmagnetised plasma can be used to derive the dispersion relations of three waves, electromagnetic, electron-plasma (Langmuir waves), and ion-acoustic [Kruer, 2003]. For electromagnetic waves (EMWs) the dispersion relation is given by,

$$\omega_{EMW}^2 = \omega_{pe}^2 + c^2k^2, \tag{1.56}$$

where ω_{pe} is the electron plasma frequency, and c is the speed of light.

The electron-plasma wave (EPW) dispersion relation is dependent on the thermal velocity, v_{th} (eq. (1.15)), and is known as the Bohm-Gros relation,

$$\omega_{EPW}^2 = \omega_{pe}^2 + 3k^2v_{th}^2, \tag{1.57}$$

And the ion acoustic wave's (IAWs) dispersion relation is,

$$\omega_{IAW} = c_sk. \tag{1.58}$$

where c_s is the sound speed.

These relations are plotted in fig. 1.12. The point at which the EPW and EMW dispersion relations intersect at $k \mapsto 0$, and $\omega \mapsto \omega_{pe}$ determines the critical density, n_{crit}. Beyond this density, EMWs can no longer propagate. At the critical density, EMWs deposit their energy through resonance absorption or are reflected and decay into evanescent waves.

The interaction of a high power laser, such as those utilised in ICF experiments, with a plasma seeds three-wave instabilities. Higher order instabilities do occur in experiment, but the most significant are three-wave. Note that such wave interactions are subject to the wave-vector matching conditions, $\vec{k_0} = \vec{k_1} + \vec{k_2}$, which implies, $\omega_0 = \omega_1 + \omega_2$. Some of the laser energy is reflected away from the target by the Stimulated Brillouin scattering (SBS) and Stimulated Raman Scattering (SRS) instabilities. Some of the laser energy can be redirected from the incoming laser to a reflected wave by Cross-Beam Energy Transfer (CBET), which is a form of SBS that occurs under certain conditions. In addition, hot electrons that preheat the target can be generated through the Two Plasmon Decay (TPD) and SRS instabilities. A summary of these laser plasma instabilities is given in Table 1.1. Note that for all of these instabilities, we assume small non-linear coupling, i.e each of the waves has an angular frequency and wavevector that locally satisfy the linear dispersion relations shown in equations 1.58, 1.59, and 1.60.

Instability	**Condition**	**Coupling equation**
Stimulated Brillouin Scattering	$\omega_p < \omega_0 < 2\omega_p$	$\omega_0 = \omega_s + \omega_{ia}$
Stimulated Raman Scattering	$\omega_0 > 2\omega_p$	$\omega_0 = \omega_s + \omega_e$
Two Plasmon Decay	$\omega_0 \simeq \omega_p$	$\omega_0 = \omega_{e1} + \omega_{e2}$

Table 1.1: Table showing the angular frequency, ω, conditions and coupling equations of the most common laser-plasma instabilities; SRS, SBS, and TPD, found in ICF experiments. Note that the angular frequencies of the waves are denoted by: ω_p for the plasma; ω_0 for the incoming laser; ω_s for the scattered electromagnetic wave; ω_{ia} for the ion acoustic wave; and ω_e for the electron plasma waves.

SBS occurs when an incoming electromagnetic wave interacts with an ion acoustic wave to produce a scattered electromagnetic wave. In ICF experiments, the ion acoustic wave is generated through the beating of the incident and scattered electromagnetic waves which occurs because of the nonlinearity of the ponderomotive force. The ponderomotive force is experienced by a charged particle in an oscillating electric field, and causes it to move towards the region of weaker electric field. For further information on this instability, see [Kruer, 2003].

When SBS is seeded by reflected light, it is known as Cross-Beam energy transfer. When there is a spectral dispersion in the frequencies of interacting electromagnetic waves, this can seed the SBS instability. In the reference frame of the ablated plasma, light that has been reflected from the critical surface of the target, is Doppler shifted by the moving shell resulting in spectral broadening, meaning that there is a small variation between the reflected and incident light. Because of this variation, CBET works to transfer energy from the incoming laser, to a scattered EMW via an ion-acoustic wave. On the OMEGA experiment, it is estimated that between 10% to 20% of the laser energy is lost to CBET [Igumenshchev et al., 2010].

Stimulated Raman Scattering occurs when an incoming electromagnetic wave interacts with an electron plasma wave to generate an electromagnetic wave. This instability is limited to densities below the quarter-critical density since the matching conditions allow only for the interaction of the EMW with EPWs of frequencies $\omega_0 > 2\omega_p$, corresponding to electron densities of $n_e < n_{crit}/4$. Experimentally, SRS is found at densities between 0.15-0.25n_{crit} [Rosenberg et al., 2018]. Collisional damping can work to suppress SRS, however this is not prominent in direct-drive coronal plasmas.

The TPD instability occurs when an electromagnetic wave decays into two electron plasma waves, which have a corresponding frequency that is half of the incoming laser frequency, $\omega_p = \omega_0/2$. Given the relation between the plasma frequency and density (as described in eq. (1.14)), the region of the coronal plasma that this is possible, is near the quarter-critical density, $n_{crit}/4$, and is restricted by Landau damping, as mentioned in the following section.

In the region of a Maxwellian particle velocity distribution near the phase velocity of the incoming laser, v_{ph}, electron plasma waves (generated by SRS and TPD) can be accelerated. The electric field of the incoming electromagnetic wave applies a force to particles in this region of the distribution function to have a velocity equal to the phase velocity of the EMW. This has the effect of flattening the velocity distribution function around v_{ph}. Provided that the gradient of the velocity distribution is negative, more energy will be gained by the particles than lost during this velocity shift. This process is called Landau damping and creates a population of suprathermal electrons. Hot electrons preheat the target and reduce the compressibility of the fuel.

1.6.6 Suprathermal Electrons

During the laser interaction with the ablated coronal plasma, laser plasma instabilities (section 1.6.5) and resonance absorption (section 1.5.1) transfer energy from the target to electron plasma waves. These electron plasma waves can be Landau damped resulting in the release of high energy electrons, also known as suprathermal electrons. These electrons can penetrate beyond the critical surface, thereby preheating the centre of the target, where the DT fuel is. This preheating makes the fuel less compressible, and deteriorates the implosion of the capsule. To diagnose these hot electrons, the X-rays generated through bremßtrahlung are measured. Typical hot electron measurements from ICF experiments, typically find thermal distributions with temperatures between 20-40 keV [Rosenberg et al., 2018].

Research conducted on the impact of suprathermal electrons (with $T_h = 55keV$ and $E_h = 13kJ$) in shock ignition, a scheme of direct-drive inertial fusion in which the laser power profile has a large spike in intensity towards the end of the drive, found that a 35% decrease in peak areal density [Barlow et al., 2022].

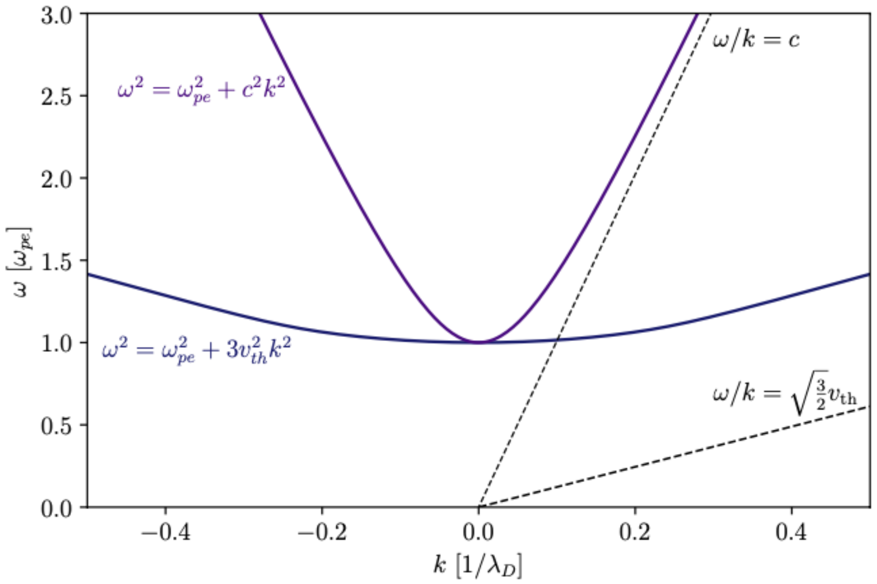

Figure 1.12: Dispersion relations for electromagnetic waves and electron plasma waves in a non-magnetised, hot plasma with T_e = 5keV, n_e =0.1n_{crit}. The limits are chosen such that $k_{EPW}\lambda_D < 0.5$, which is required for equation 1.59 to be valid. Reproduced with permission from [Spencer, 2021].

1.7 Scope of this Thesis

As described in the latter sections of this introduction, implosion asymmetry and hot electrons are two of the most significant barriers preventing ignition in ICF. Significant study has been conducted into quantifying and mitigating the impact of these problematic phenomena, but have solely focused on OMEGA scale experiments. Eventually, direct-drive experiments and facilities will be scaled up for ignition, meaning a larger target and higher laser energies. Using simulations conducted with the 2D radiation-hydrodynamics code, *Odin*, the author has set out to study the impact of implosion asymmetry and hot electrons on experiments of this size and to quantify their impact on a series of implosion performance metrics such as areal density and hotspot temperature.

In the next five chapters, we present the methodology and work conducted by the author as part of their PhD research. Note that this introductory chapter is not original but provides background descriptions which help to illustrate and put into explained context the remainder of this thesis. The content of the subsequent chapters is as follows:

Chapter 2 The next chapter outlines the computational methodology utilised to carry out the research presented in this thesis. A brief description of computational hydrodynamics is given before a more in-depth explanation of radiation-hydrodynamic codes and the code used for the simulations presented in this work, *Odin*, is presented.

Chapter 3 In this chapter, we describe the improvements implemented to the *Odin* radiation-hydrodynamics code during the course of this PhD. Examples of these improvements include a 3D refractive ray-tracing model.

Chapter 4 Here we describe the various sources of implosion asymmetry in inertial confinement fusion experiments. A computational investigation quantifying the impact of these various sources of asymmetry is given using the reference case of the simulation conducted in Craxton *et al.*

Chapter 5 As a continuation to Chapter 4, we investigate the effects of hot electrons on implosion performance and of sources of implosion asymmetry while hot electrons are present.

Chapter 6 The final chapter of this thesis summarises the findings of the author. An overview of results is given before a discussion of the limitations of the work and avenues of future investigation.

Chapter 2

Methods

This chapter introduces the radiation-hydrodynamic code *Odin*, a 2D RZ radiation-magnetohydodynamics ALE code [Mihalas and Mihalas, 1984]. Using *Odin*, I carried out a number of ICF simulations designed to investigate the impact of laser asymmetries. The fundamental equations and formulation of this code, and some of its unique features are described throughout this chapter.

2.1 Hydrodynamics

The evolution of an ideal fluid is described by the Euler equations, each of which represent the conservation laws of; mass; momentum; and energy and are given by:

$$\text{[Mass]} \quad \frac{\partial \rho}{\partial t} + \nabla \cdot (\rho \vec{u}) = 0 \tag{2.1}$$

$$\text{[Momentum]} \quad \frac{\partial \vec{u}}{\partial t} + \vec{u} \cdot \nabla \vec{u} + \frac{\nabla p}{\rho} = \vec{g} \tag{2.2}$$

$$\text{[Energy]} \quad \frac{\partial e}{\partial t} + \vec{u} \cdot \nabla e + \frac{p}{\rho} \nabla \cdot \vec{u} = 0 \tag{2.3}$$

where ρ is the fluid mass density, $\vec{u}$ is the velocity vector, p is the fluid pressure, g is the external force vector, and e is the specific internal energy.

For an ideal gas, the specific internal energy, e, the thermodynamic pressure, P, and the heat capacity ratio, $\gamma = C_P/C_V$, are linked by the ideal gas equation:

$$e = \frac{P}{\rho(\gamma - 1)} \tag{2.4}$$

The ideal gas equation above, provides an equation-of-state (EoS) - a closure relation for the Euler equations, which does not bring in a new dependence for the parameters.

In reality, the equation of state is more complicated than the ideal gas equation. Many radiation-hydrodynamic codes use tabulated EoS tables, with experimental data, in order to accurately represent the materials.

Radiation-hydrodynamic codes, have the added feature of being able to model radiation throughout the fluid. This is vital when simulating inertial confinement fusion experiments.

2.1.1 Eulerian Method

The Eulerian method discretises the fluid and has a grid of cells which are fixed in space, throughout the simulation, and allow the fluid to flow through it [Benson, 1992]. In a purely Eulerian code, the grid is fixed, and typically orthogonal, meaning that the physics is simple to calculate. Additionally, a fixed grid means that any simulations are robust and not prone to tangling or any grid distortions. This is a desirable feature for running simulations of systems that are turbulent or prone to distortions.

Despite its many advantages, a fixed grid introduces numerical diffusion, lowering the accuracy of the results. It means that any sharp features, such as the interface between two materials, are smoothed out and spread over multiple cells, thereby artificially mixing the materials. This smoothing is also problematic for resolving shocks in the fluid. Since the grid is fixed for all times during the simulation, it means that the resolution of the domain has to be sufficiently high across the entire domain to account for the movement of the fluid as it evolves. Eulerian simulations of ICF experiments will also perform material interface reconstruction. Both of these factors can add substantial computational cost to Eulerian simulations.

2.1.2 Lagrangian Method

Similarly to the Eulerian method, the Lagrangian method discretises the fluid using a domain of cells. Whereas the Eulerian method uses a fixed grid, the cells of a Lagrangian mesh move with the fluid [Benson, 1992]. By treating the fluid in this manner, the code is less diffusive and does not smooth out any features of the fluid through advection. The moving grid has the advantage of providing a time-dependent resolution to the region that requires it, limiting the computational cost when compared with an equivalent Eulerian simulation. In addition, by aligning the mesh with material interfaces, as is standard for Lagrangian hydrodynamics, they are automatically tracked throughout simulations.

The disadvantage of the Lagrangian method is that the movement of the mesh with the fluid means that the grid can become highly sheared and then tangle. As the grid becomes more distorted or compressed, the distance between neighbouring cells can decrease. According to the Courant-Friedrichs-Lewy (CFL) condition (discussed in section 2.1.3), this decrease in distance leads to a corresponding decrease in timestep, thereby increasing the compute time and cost of the simulation. If the grid is too distorted, the simulation can no longer run.

Mesh movement with the fluid, means that the grid can take an arbitrary shape. Solving physics for an arbitrary grid can become complicated and increase computational cost [Shashkov and Steinberg, 1996]. Despite their complexity, Lagrangian codes are still desirable because they obtain accurate results and minimise any numerical effects.

To implement the Lagrangian method, it is necessary to convert the Euler equations into the Lagrangian frame. This is done by using the Lagrangian derivative,

$$\frac{Df}{Dt} = \frac{\partial f}{\partial t} + \vec{u} \cdot \nabla f, \tag{2.5}$$

where f is a general scalar parameter. This transformation yields the following equations:

$$\text{[Mass]} \quad \frac{D\rho}{Dt} + \rho \nabla \cdot \vec{u} = 0 \tag{2.6}$$

$$\text{[Momentum]} \quad \rho \frac{D\vec{u}}{Dt} + \nabla P = 0 \tag{2.7}$$

$$\text{[Energy]} \quad \rho \frac{De}{Dt} + P \nabla \cdot \vec{u} = 0 \tag{2.8}$$

2.1.3 CFL Condition

The Courant-Friedrichs-Lewy (CFL) condition [Courant et al., 1986] is a condition for the stability of numerical methods that model convection or wave phenomena. As such, it plays an important role in Computational Fluid Dynamics and is relevant to the stability of this code.

Formally, the CFL condition is defined as: "*the full numerical domain of dependence must contain the physical domain of dependence*" [Laney, 1998]. Therefore, the CFL condition expresses that the distance that any information travels during the timestep length must be lower than a spatial discretisation as determined by the set of numerical equation being solved.

Generally, the Courant number (C), the physical parameter used to implement the CFL condition, is described by the following equation:

$$C = a \frac{\Delta t}{\Delta x} \tag{2.9}$$

where Δt is the timestep, Δx is the length between mesh elements, and a, is the velocity magnitude described by,

$$a = c_s + v \tag{2.10}$$

where v is the velocity of the fluid element and c_s is the sound speed in an ideal gas:

$$c_s = \sqrt{\frac{\gamma P}{\rho}} \tag{2.11}$$

It follows that for any explicit simple linear advection problem, the Courant number, C, must be equal to or smaller than 1, otherwise, the scheme would be unstable according to von Neumann stability analysis. Von Neumann analysis is a method of evaluating the stability of finite difference schemes which use linear partial differential equations [Charney et al., 1950].

Using this restriction on the Courant number, C, it is possible to calculate a timestep value for which the simulation is stable. Note that the CFL condition has to be valid across the entire spatial domain for each timestep, therefore we must consider the points at which it might fail - high velocities (large a), and small distance between neighbouring cells (small Δx). Therefore, we use the following equation to calculate the timestep for the j^{th} iteration:

$$\Delta t^j = C\frac{min(\Delta x^j)}{max(a^j)} \leq \frac{min(\Delta x^j)}{max(a^j)} \tag{2.12}$$

This condition sets a lower criterion for the stability of the dynamics, and when other phenomena are considered such as shock waves and artificial viscosity, then a more restrictive condition must be put in place. This can usually be solved by significantly lowering the Courant number. In *Odin*, a multiplier below unity is applied to ensure the timestep is sufficiently small.

Shock Viscosity

It is not possible to resolve a shock discontinuity in a first-principles physics code with a finite resolution. Due to the sharp gradients involved this creates distinct numerical oscillations in predictions due to overshoots if the shock is not effectively considered. This was originally addressed by von Neumann and Richtmyer [von Neumann and Richtmyer, 1950] who developed a quadratic viscosity formulation to smear the shock across multiple cells. The method was intended to complete the Rankine-Hugoniot jump conditions [Zel'dovich and Raizer, 2012] and remain negligible away from shocks.

The shock viscosity provides a means of modelling discontinuous shocks by smearing it across a rapidly varying but continuous transition region while maintaining the Rankine-Hugoniot jump conditions.

Since the original form of artificial viscosity was first described by von Neumann and Richtmyer, several alternative forms of artificial viscosity have been developed. The original equation for artificial viscosity, q, was given by [von Neumann and Richtmyer, 1950]:

$$q_{nl} = c_2 \rho (\Delta \mathbf{v})^{\mathbf{2}} \tag{2.13}$$

where c_2 is a constant of order unity, ρ is the density and $\Delta \mathbf{v}$ is the change in velocity. Note that the q value is zero in the case where $\Delta \mathbf{v} < \mathbf{0}$.

One of the most successful forms of artificial viscosity was developed by Kuropatenko [Kuropatenko, 1963], and later by Wilkins [Wilkins, 1980], which contains linear and non-linear components and is given by:

$$q_{Kur} = \rho \left\{ c_2 \frac{(\gamma+1)}{4} |\Delta \mathbf{v}| + \sqrt{c_2^2 \left(\frac{\gamma+1}{4} \right)^2 (\Delta \mathbf{v})^2 + c_1^2 c_s^2} \right\} |\Delta \mathbf{v}| \tag{2.14}$$

where γ is the heat capacity ratio, c_1 is a constant which is usually set to unity, and c_s is the sound speed of the medium. Note that $c_1 = c_2 = 1$ gives the solution for an ideal gas.

To implement the artificial viscosity, it is necessary to add the q term whenever pressure, P, is included, i.e $P \mapsto P + q$. This transforms the hydrodynamic equations and sound speed such that it is now defined by:

$$c_s = \sqrt{\frac{\gamma (P+q)}{\rho}} \tag{2.15}$$

Note that this will lower the value of each timestep iteration, Δt.

2.2 Arbitrary Lagrangian Eulerian Codes

Some hydrodynamic schemes exist that adopt the beneficial properties of both Lagrangian and Eulerian schemes. There are subtle but important differences in their application, which will be discussed in this section.

2.2.1 Lagrangian Remap codes

One scheme of hydrodynamic codes that offers the benefits of both Eulerian and Lagrangian methods is the Lagrangian remap. Codes of this type work by running each timestep in Lagrangian mode, before remapping the fluid variables back to the original grid [Arber et al., 2001]. It has the advantages of Lagrangian simulations: reduced numerical diffusion, better estimation of material mixing, and is able to resolve physical features within the fluid, in addition to the robustness and simple physics calculations associated with the Eulerian scheme.

In remapping to its original grid, the computational cost is increased and is carried out after every single timestep. Remapping also adds numerical diffusion, reducing the numerical accuracy of simulations. It shares the same issues as a fully Eulerian grid and needs sufficient resolution at all points across the domain to account for the movement of the fluid with time.

2.2.2 Arbitrary Lagrangian Eulerian methods

The Arbitrary Lagrangian-Eulerian (ALE) method is similar to the Lagrangian remap scheme, in that it utilises a Lagrangian step for each timestep and has the ability to remap [Caramana et al., 1998, Benson, 2013]. Where it differs, is that the remap is optional and only carried out if deemed necessary due to the distortion of the grid, or complexity of the physics calculations. In addition, the remap can be to an arbitrary grid, not only the original grid. Reducing the number of times the grid is remapped means that the computational cost is less, and that the mesh can take an arbitrary shape and resolve any features. This has the added benefit of reducing numerical diffusion.

Simulations of this scheme run for as long as possible in Lagrangian mode, adopting all of its advantages. When the need arises for the grid to remap, i.e when it becomes distorted or the distance between cells is too small, then the mesh can be remapped and the simulation can continue to run. The grid does not have to return to its original position, and can remap to the grid from the latest timestep, thereby maintaining the time-dependent resolution. This allows us to run reliable simulations that would otherwise be impossible to run in Lagrangian mode. This makes ALE codes a suitable candidate for running ICF simulations in which distortions are expected. It is for these reasons that *Odin* was designed as an ALE code.

2.3 Odin

Odin is a 2D radiation-magnetohydrodynamics code [Mihalas and Mihalas, 1984] that utilises Arbitrary Lagrangian-Eulerian mesh refinement [Benson, 1992, Bennett et al., 2021]. The code was first developed by Tom Goffrey for his PhD thesis [Goffrey, 2014], and he, along with Keith Bennett and Tony Arber, currently maintains and continues to develop the code at the University of Warwick. *Odin*'s progress is the result of a UK collaboration between the Rutherford Appleton Laboratory, University of York, Imperial College, and the University of Warwick. Remapping can be applied dynamically during simulations or statically from a restart file. Simulations can be run with a Cartesian grid, but for ICF capsule simulations, then a cylindrical coordinate system is used with area weighting [Burton et al., 2013].

The code is single-fluid but can populate multiple materials within the fluid. The ions of the various materials, and electrons can have distinct temperatures. Note that for the hydrodynamic calculations, the pressure and density of the cells consider the contribution of both ions and electrons; $p = p_i + p_e$ and $\rho = \rho_i + \rho_e$. The figure below provides an illustration showing the locations of hydrodynamic variables in a computational cell.

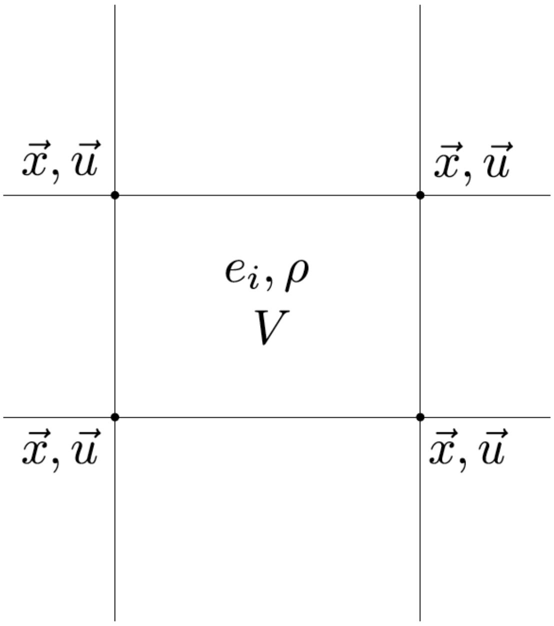

Figure 2.1: Hydrodynamical variable placement on a staggered grid. Reproduced with permission from [Goffrey, 2014].

There are a number of advanced features that Odin has which make it a suitable code for ICF simulations such as:

- 3D hot-electrons with energy deposition and scattering
- Radial laser ray-tracing with energy deposition
- Flux limited thermal conduction
- Multigroup radiation transport
- Tabulated equation-of-state and atomic data
- Magnetohydrodynamics

In ICF implosions, energy is transported around the capsule through two main mechanisms: thermal conduction and radiation transport. Energy transport is crucial for transporting laser energy that has been deposited by IB, to the ablation surface, and is also of great importance at peak compression when the hotspot transfers some of its energy to the surrounding cold fuel. These two mechanisms and their implementation for *Odin* will be discussed in further detail in the following sections. The overall energy transport within the system for electrons in the Lagrangian frame is given by:

$$M\frac{D\tilde{e}_e}{Dt} = -\tilde{P}_e\int \vec{u}\cdot d\vec{S} - \int Q\cdot d\vec{S} + \frac{dE_{eq}}{dt} + \frac{dE_{laser}}{dt} + \frac{dE_{hot}}{dt} \tag{2.16}$$

where $\tilde{e}$ and $\tilde{P}_e$ are the mass-averaged internal energy and pressure of the electrons, respectively, and $\vec{u}$ is the fluid velocity of the mass in each cell element, and Q is the energy flux, given by,

$$Q = -\kappa(T)\nabla T. \tag{2.17}$$

where κ is the thermal conductivity, and ∇T is the temperature gradient. The energy terms on the RHS of equation eq. (2.16) are as follows: E_{eq} is the equalisation energy passed between ions and electrons, E_{laser} is the energy deposited by the laser, E_{hot} is the energy deposited by the hot-electrons. Note that the laser and hot-electron energy deposition is only considered for electrons in *Odin*, therefore the ion energy transport equation will not have these terms.

2.3.1 Hot-Electron Model

The hot-electron model in *Odin* utilises a hybrid method that treats the electrons as kinetically modelled macro-particles, and was developed by Duncan Barlow and Keith Bennett [Barlow, 2021]. A population of electrons is generated by diverting some chosen fraction of the laser energy, near the quarter critical density (this is also specified by the user), to hot-electrons, thereby mimicking the mechanism of LPIs, as dicussed in section 2.3.1. These particles are mono-energetic or Monte-Carlo sampled on a thermal distribution of user-defined temperature. An example of this sampling is shown in fig. 2.2. The electrons are free to travel through the quasi-neutral fluid, and deposit their energy to cells as they travel through them. The path tracking allows the electrons to be traced in both $2D$ and $3D$, this process will be discussed in further detail in section 2.3.2. Although these generated electrons break charge and particle conservation, we ignore these effects. A list of the input deck parameters relevant to the hot-electrons is shown in section 2.3.1.

Input parameter	**Value**	**Default**	**Use**
use_uniform_electron_spread	Boolean	False	Include electrons
use_paths_2d	Boolean	True	2D electrons
use_paths_3d	Boolean	False	3D electrons
use_radial_electrons	Boolean	False	Electrons pointed at $R = 0$
use_electron_scatter	Boolean	False	Electron scattering
electron_reflect	Boolean	False	Reflect electrons at domain edge
electron_angular_spread	Numeric	0.1	Spread of electron beam
nelectrons_per_group	Numeric	100	Electrons generated per ray
electron_time_start	Numeric	0.0	Start time
electron_time_stop	Numeric	-1.0	End time
electron_laser_reduction	Numeric	10(%)	Energy lost from laser to LPIs
electron_energy_percent	Numeric	5(%)	Laser energy converted to electrons
electron_temperature_kev	Numeric	30(keV)	Distribution temperature
electron_energy_cutoff	Numeric	150(keV)	Max electron temperature
electron_start_angle	Numeric	0.7854	Initial angle of electrons
electron_start_spread	Numeric	-1.0	Initial angular spread
electron_ne_ratio	Numeric	0.25	Density at which electrons created

Table 2.1: Table of the *Odin* input deck parameters that are relevant to the ray-tracing routine.

Energy deposition of the electrons is discretised per cell, and calculated by the stopping power per unit distance travelled according to [Robinson et al., 2014, Seltzer and Berger, 1984]

$$\frac{dE}{dr} = -\frac{n_e e^4}{4\pi\varepsilon_0^2 m_e v} L_d, \tag{2.18}$$

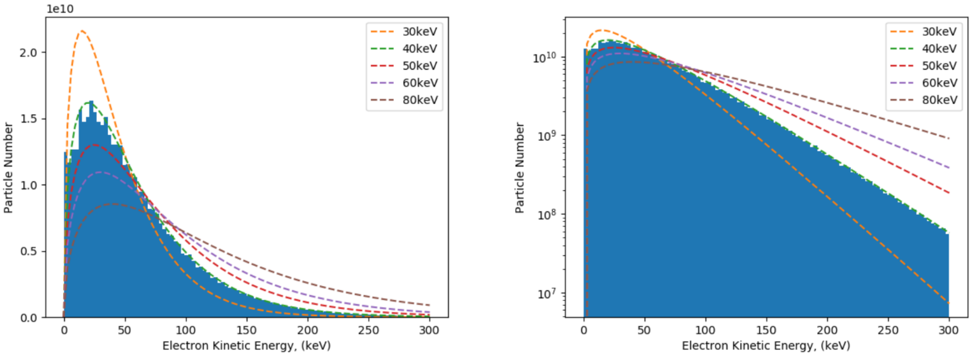

(a) (b)

Figure 2.2: (Left) Linear and (Right) logarithmic particle distributions. The histogram represents a 40 keV thermal hot-electron emission distribution using Odin's uniform sampler between 0 and 300 keV with 10,000 paths, each path is mono-energetic. Uniform sampling spreads the paths uniformly in energy space (initial electron energy) and uses particle weighting from the probability distribution function. Reproduced with permission from [Barlow, 2021].

where L_d is the drag factor, a dimensionless parameter defined by:

$$L_d = \ln\left(\frac{pv}{\sqrt{\gamma+1}\hbar\omega_p}\right) - \frac{\ln 2}{2} + \frac{9}{16} + \frac{(1/2)\ln 2 + 1/16}{\gamma^2} - \frac{\ln 2 + 1/8}{\gamma} \qquad (2.19)$$

where γ is the Lorentz factor, E, p, and v are the fast electron's energy, momentum, and velocity respectively. The reduced Planck constant is shown as, $\hbar = h/2\pi$, n_e is the background electron number density of the plasma and ω_p is the plasma frequency. Note that the drag factor, L_d would be denoted as the Coulomb logarithm, $\ln\Lambda$, in the classical limit of electron energies. For equation 2.19 to hold for ionised material, the kinetic energy of the hot-electrons must be greater than the thermal energy of the plasma, i.e $m_e v_h^2 >> kT_e$. Low energy electrons which do not satisfy this criterion deposit their total energy quickly, therefore it is not unreasonable to maintain the form of L_d shown in eq. (2.19).

As the hot-electrons are generated, charge conservation is momentarily broken by a forward current, j_h. To return to equilibrium, a return current, j_b, must be generated such that [Robinson et al., 2014],

$$j_h + j_b \simeq 0. \qquad (2.20)$$

Note that large magnetic fields are not generated by these currents, since they cancel out each other locally. Magnetic fields are not considered by *Odin*'s hot-electron routine, but if implemented would effect the energy deposition. Considering a plasma with a typical restivity of $\eta \sim 10^{-7}\ \Omega m$ and a return current of $j_b \sim 10^{12}\ A$, a resistive electric field is generated with a magnitude of,

$$E \simeq -\eta j_b \simeq 10^5 V m^{-1}, \tag{2.21}$$

and leads to subsequent Ohmic heating,

$$\frac{P}{V} = -\eta j_h^2 = 10^{17} W m^{-3}. \tag{2.22}$$

This translates to heating material at solid density by $\sim 1J/mg$. This is insignificant compared to the $\sim 1kJ/mg$ that is contributed by the kinetic energy of the hot-electrons. Therefore, it is not considered necessary to include the contributions of the return current on the energy of the plasma [Barlow, 2021].

The functionality of scattering has been added to the hot-electron routine. As the plasma properties are discretised by the mesh of the simulation domain, so is the scattering. The change in *rms* scatter angle per unit distance travelled, $d\langle\theta^2\rangle/dr$, from interactions within a fully ionised plasma is given by [Robinson et al., 2014],

$$\frac{d\langle\theta^2\rangle}{dr} \simeq \frac{n_e e^4}{2\pi(\varepsilon_0 p v)^2}\left[(Z+1)L_s - \frac{1}{2}\ln\frac{\gamma+3}{2}\right] \tag{2.23}$$

where L_s is the scattering number, of ions, given by,

$$L_{s-i} \simeq \ln\frac{2\lambda_D p}{\hbar} - 0.234 - 0.659\frac{v^2}{c^2}. \tag{2.24}$$

This equation holds when $\left(\frac{2\lambda_D p}{\hbar}\right) \gg 1$. An image of scattering, hot-electrons being generated from an incoming ray is shown in fig. 2.3. For further information on the hot-electron routine in *Odin*, the author refers the reader to [Barlow, 2021, Robinson et al., 2014]

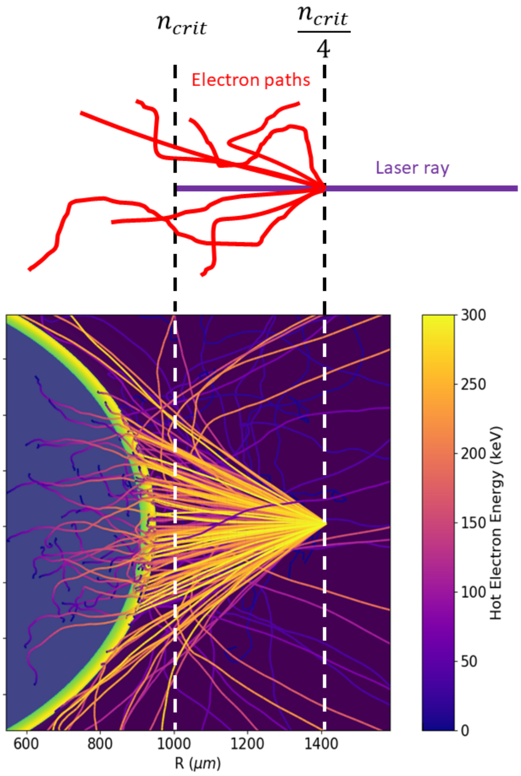

Figure 2.3: Above: Schematic demonstrating how hot-electrons are generated from laser rays at the quarter critical surface. Below: Odin diagnostic showing the density of a solid plastic target (colour bar not shown) with electron paths emitted from a single ray overlaid. The colour axis refers to the hot-electron path energy. Reproduced with permission from [Barlow, 2021].

2.3.2 Path Tracking

The path tracking of particles (rays and hot-electrons) can be performed in both 2D and 3D, and updates the trajectory at cell or mesh interfaces respectively. Although the paths have the ability to move in 3D, note that the hydrodynamics of simulations run with *Odin* are restricted to 2D. To track particles in 3D, the original 2D cylindrical RZ grid is rotated 2π about the z-axis. This creates a mesh of hexahedrons (irregular cuboids), with a user-defined azimuthal resolution or with a default value that is dependant on the original cell resolution, $N_\phi = (N_r N_z)^{1/2}$, where N_r, and N_z are the number of cells in the r, and z directions respectively. In the rotation of the domain, cylindrical symmetry is assumed, and the replicating cells share the same properties and shape of the original 2D domain. Effectively, each cell in the RZ *Odin* grid represents a discretised torus, and any energy deposition from the rays to the torus, collapses to the 2D cell.

The path tracking operates with shared memory in OpenMPI because the calculations can not be easily parallelized on distributed memory. Note that for radially moving particles, there are near-identical results in 2D and 3D simulations (as discussed in further detail in section 3.3.3). Since the particle trajectories are only updated at mesh interfaces, there is a strong dependence on the resolution of the domain for accurately tracking the particles [Atzeni et al., 2009]. Since high density regions are typically well-resolved for hydrodynamic simulations, the ray trajectories are typically less affected by this dependence. For electrons that are able to traverse the critical surface, this resolution becomes more important and can mean inaccurate energy deposition if not handled properly.

2.3.3 Radial Ray-tracing

To replicate the energy deposition of a laser, a simplified radial ray-tracing model was implemented. The routine generates a population of macro-particle rays, that carry a fraction of the laser energy for each timestep. These rays travel radially inward and deposit energy via inverse bremßtrahlung in the underdense plasma, as described by eq. (1.45), and at the critical surface a user-defined amount of energy is deposited to replicate resonance absorption, before being reflected outwards once more. Note that this raytracing model does not include refraction, or allow for any other configuration other than rays travelling towards the centre of the target. Radial rays provide idealised energy deposition for the laser.

2.3.4 Thermal conduction

Odin solves the non-linear conduction equation for electron and ion thermal conduction,

$$c_v \frac{\partial T_{i,e}}{\partial t} = \nabla \cdot \kappa_{i,e} \nabla T_{i,e} \tag{2.25}$$

where the diffusion coefficient, $\kappa_{i,e}$ is given by:

$$\kappa_{i,e} = \kappa_0 T_{i,e}^{2.5} \tag{2.26}$$

This value of κ_0, has units of $Jm^{-1}s^{-1}K^{-1}$, and is obtained using the following equation [Braginskii, 1965]:

$$\kappa_0 = \frac{12\pi^{3/2}\varepsilon_0^2 k_B^{7/2}}{\sqrt{2m_e}e^4 \ln \Lambda} \tag{2.27}$$

where $\ln \Lambda$ is the Coulomb logarithm.

Odin uses isotropic electron thermal transport coefficients, which were first described by Spitzer and Härm [Spitzer and Härm, 1953], and later improved on by Braginskii [Braginskii, 1965] and Manheimer *et al.* [Manheimer et al., 2008]. They define the thermal conduction in terms of thermal flux, Q_x, and in 1D the non-linear conduction equation is given by:

$$\rho c_v \frac{dT}{dt} = -\frac{d}{dx} Q_x \tag{2.28}$$

where c_v is the specific heat capacity, $c_v = (\partial e/\partial T)_v$. The thermal flux can be solved to yield the following equation:

$$Q_x = -\kappa(T)\frac{d}{dx}T \tag{2.29}$$

where κ is a constant defined by,

$$\kappa(T) = f(Z)\frac{nk_B^2 T_{i,e}\tau_c}{m} \tag{2.30}$$

τ_c is the collision time,

$$\tau_c = \frac{12\varepsilon_0^2}{ne^4 \ln \Lambda}\sqrt{\frac{(m_e(k_B T)^3}{2}} \tag{2.31}$$

and $f(Z)$ as specified using the approximation [Epperlein and Short, 1991]

$$f(Z) = 13.6\frac{Z + 0.24}{Z + 4.24} \tag{2.32}$$

The Braginskii equation describes the classical model of thermal conduction, but *Odin* uses Larsen flux-limited thermal conductivity, κ', as described by Olson *et al.* [Olson et al., 2000],

$$\kappa' = \frac{1}{\sqrt{\frac{1}{\kappa^2} + \left(\frac{1}{f_0 f_{fs}}|\nabla T|\right)^2}}. \tag{2.33}$$

Here f_{fs} is the free-streaming flux, described by,

$$f_{fs} = v_{th} n k_B T, \tag{2.34}$$

and f_0 is the flux limiter as set by the user. Typically for direct-drive simulations, this has a value of ~0.05 [Craxton et al., 2015]. Simulation results are highly sensitive to the value of the flux limiter [Goncharov et al., 2008].

2.3.5 Radiation transport

Radiation transport describes the way in which energy is coupled between the plasma and radiation. The electrons, and to a lesser extent ions, absorb energy from the incoming laser through inverse bremßtrahlung. Similarly, electrons in the plasma can lose energy through bremßtrahlung emission. It is essentially another method through which energy can disperse through the target. *Odin* uses multigroup diffusion to treat these energy transfers. The transport equation is a mathematical description of the conservation of photons and in its general form is given by:

$$\left(\frac{1}{c}\partial_t + \vec{n}\cdot\nabla\right)I = \eta - \chi I \tag{2.35}$$

where I is the specific intensity of radiation of a given frequency, $\vec{n}$ is the direction vector of the light, η is the emissivity and χ is the opacity of the material the radiation is travelling through. Values of opacity and emissivity are tabulated by radiation frequency, electron density, and temperature to give fast approximations to the transport equation.

2.3.6 Magnetohydrodynamics

In an electrically conducting fluid, such as a plasma, magnetic fields can induce currents. Equally, currents moving in the fluid can generate magnetic fields. By considering Maxwell's equations of electromagnetism and the Euler equations of fluid dynamics, we can derive the equations of magnetohydrodynamics (MHD) as used in *Odin*.

The Cauchy momentum equation for the bulk ion motion of a quasi-neutral fluid is given by,

$$\rho\left(\frac{\partial}{\partial t} + \vec{v}\cdot\nabla\right)\vec{v} = \vec{J}\times\vec{B} - \nabla p \tag{2.36}$$

where $\vec{J}$ is the current density vector, $\vec{B}$ is the magnetic field vector, and p is the plasma pressure. The presence of a magnetic field, $\vec{B}$, within a plasma gives rise to the Lorentz force, $\vec{J}\times\vec{B}$, which can modify the hydrodynamic response of an imploding ICF capsule and takes the form,

$$\vec{J} \times \vec{B} = \frac{\vec{B} \cdot \vec{\nabla} \vec{B}}{\mu_0} - \nabla \left(\frac{B^2}{2\mu_0} \right) \tag{2.37}$$

MHD is an important consideration for magnetised ICF [Walsh et al., 2020] and also for the Biermann battery effect [Biermann, 1950] in which magnetic fields are self-generated, due to $\nabla T_e \times \nabla n_e$, during the interaction phase of indirect drive ICF experiments [Walsh and Clark, 2021, Ridgers et al., 2021]. Self-generated magnetic fields were initially of concern for direct-drive ICF experiments, however experimental measurements showed that overlapping beams suppress these magnetic fields [Willi et al., 1981], and in the case of uniform symmetric irradiation, they are unlikely to be of concern [Craxton et al., 2015].

2.3.7 Tabulated EoS

Odin has the option to run simulations using an ideal equation-of-state, or to use tabulated data taken from models such as FEOS [Faik et al., 2018], Sesame [Barnes and Lyon, 1988] and Propaceos [MacFarlane et al., 2006]. *Odin* uses the tables as a look-up during calculations, and picks values according to the plasma conditions. These tables use a combination of experimental data and theoretical models that can accurately represent the reaction of the materials under extreme conditions compared with an ideal EoS.

The ideal EoS does not accurately describe the response of materials in extreme circumstances such as those experienced in ICF experiments. To highlight the difference between using the ideal EoS and tabulated data, we ran simulations with identical initial conditions, but with different methods of handling the EoS. Note that the target under consideration here consists of DT and CH as described in section 1.4.3. The results are shown in fig. 2.4.

The comparison between the ideal EoS and tabulated EoS simulation shows a difference in the shock velocity and the timing of peak compression. By 9.5 ns, nearing peak compression, there is a separation of $\sim 30\mu m$ between the shock profiles. Such a difference can be crucial in designing a laser power profile for shock convergence.

2.3.8 Cell-mass Matching

When initialising the grid for Lagrangian simulations, it is important to set a cell mass density profile such that there are no significant jumps between neighbouring

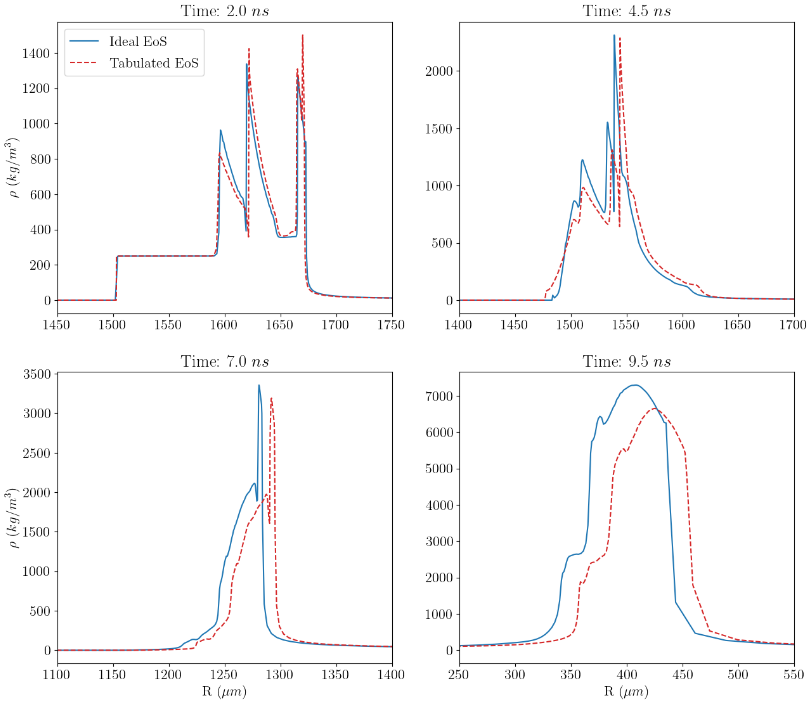

Figure 2.4: Snapshots taken from a 2D *Odin* simulation of a typical ICF implosion, using an ideal EoS (solid blue line) and a FEOS tabulated EoS (dashed red line), shown at 4 different times.

cells. For ICF simulations, this criterion is complicated by the varying densities of the materials involved. ICF capsules have a comparatively high density shell consisting of CH and DT ice, that surround a low density DT gas region as shown in fig. 1.2.

Literature stating the importance of cell-mass matching is extremely limited, and the author failed to find a reliable reference on the subject. It is an important feature of hydrodynamic codes, and without consideration, a poor cell-mass distribution can lead to artificial heating. It is likely that this occurs as a result of the simulation losing its second order accuracy. Non-centred differencing in mass-space is not 2^{nd} order accurate in *Odin*'s predictor-corrector scheme, however this is not the case for other differencing schemes.

The results of some simulations with poor mass-matching, as initialised in Figure 2.4 showed the symptoms of numerical heating with a strengthened shock travelling through the target as shown in Figure 2.5.

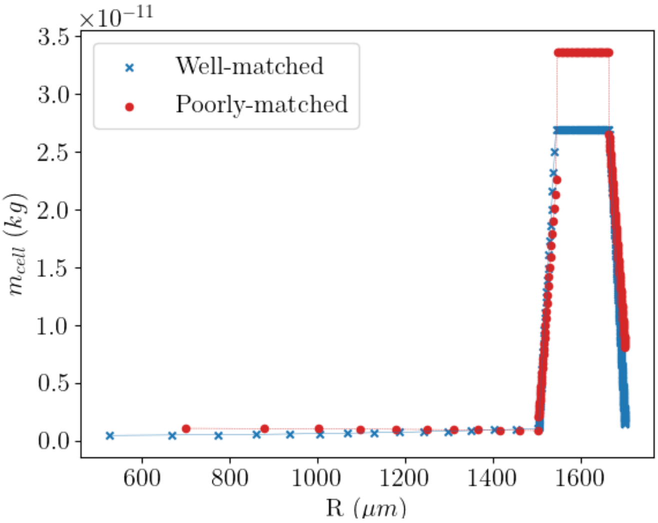

Figure 2.5: The initial radial cell mass profile for domains with well-resolved (blue crosses) and poorly-resolved (red circles) cell mass-matching.

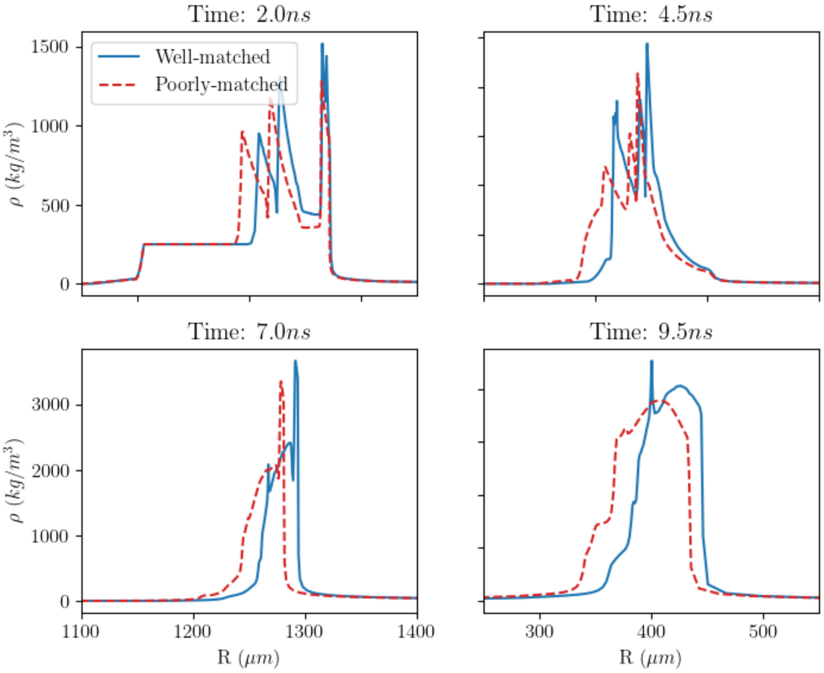

Figure 2.6: Snapshots taken from a 2D *Odin* simulation of a typical ICF implosion, using poor mass-matching (dashed red line) and good mass-matching (solid blue line), shown at 4 different times.

Chapter 3

Improvements to Odin

This chapter describes the new features and improvements implemented into the 2D radiation-magnetohydrodynamics ALE code *Odin* [Goffrey, 2014, Bennett et al., 2021] in order to conduct the necessary simulations for studying implosion asymmetry. These features were added collaboratively by the author and the *Odin* development team. The implemented features of refractive ray-tracing, wedge boundary conditions, and artificial laser non-uniformities will be discussed in the following sections.

The ray-tracing scheme was initially developed by the author as a post-processing diagnostic tool for *Odin*, that was independent of the source code. Its ability to refract rays through a plasma made it a desirable feature to include as part of the core code of *Odin*. This was implemented in the source code by Keith Bennett using a methodology similar to the electron path tracking routine. Throughout its development, the author tested the performance of the routine and communicated any issues and possible solutions.

Wedge boundary conditions were suggested for implementation by Tony Arber. Derivation of the transformations needed for applying these boundary conditions at the ghost cells of the grid domain was completed by the author. A first implementation was completed by the author, before improvements were made by Tony Arber. These boundary conditions were benchmarked against *Freyja*, a 1D radiation-hydrodynamics code developed by Tom Goffrey.

Functionality for adding artificial laser non-uniformities to the laser power was implemented solely by the author, with guidance to improve its functionality given by the *Odin* development team.

3.1 Motivation and Literature review

As discussed in Chapter 2, *Odin* is a 2D ALE radiation-magnetohydrodynamics code that is able to obtain predicted results for hydrodynamic test scenarios and has been used to study the effect of hot electrons in ICF experiments [Barlow, 2021, Barlow et al., 2022]. To improve the functionality of the code and to make it better adapted to ICF simulations, certain changes and improvements have been made. Namely the addition of a more accurate ray-tracing scheme to replace the existing radial ray scheme. The new ray-tracing scheme would have to be 3-*dimensional*, deposit energy via inverse bremßtrahlung and resonance absorption and to refract and reflect according to the plasma density. The routine would also allow the generation of hot electrons to simulate the effects of LPI in the coronal plasma of an imploding capsule, as was done with the previous ray-tracing routine as discussed in section 2.3.3. As a final addition to study the effect of laser non-uniformities, some adaptations will be added to the laser setup to replicate these sources such as laser offset, and l-mode modulations [Craxton et al., 2015].

3.1.1 Ray-tracing

Ray-tracing is an essential function in radiation-hydrodynamics codes to calculate the spatial energy deposition from a laser driver. In essence, ray-tracing schemes represent laser beams by using multiple infinitely-thin rays. There exist a number of different methods for implementing ray-tracing schemes into hydrodynamic codes, but most are based on the underlying principles of geometrical optics. In general, ray-tracing schemes work by discretising laser beams into rays whose paths, denoted by $\vec{r}(s)$, obey the Eikonal equation [Temporal et al., 2001]:

$$\frac{d}{ds}\left(\eta_{ref}\frac{d\vec{r}}{ds}\right) = \nabla\eta_{ref} \tag{3.1}$$

where s is the path length of the ray, and η_{ref} is the refractive index of the medium that the ray is travelling through. One of the key assumptions of geometric optics is that η_{ref} is quasi-static and that the laser propagation time is negligible compared with the hydrodynamic evolution of the medium.

The difficulty of choosing an appropriate ray-tracing scheme is balancing the accuracy of the scheme with its computational efficiency [Kaiser, 2000]. Geometric optics offers a more accurate description of lasers which captures several of the key physical effects: refraction, reflection and energy deposition. It is an approximation of the full wave equation and does not include diffractive effects or treat beam properties such as polarisation and electromagnetic fields [Mazzucato, 1989, Ding et al., 2020]. Such a scheme is utilised in the LARED-H hydrodynamic code [Qinghong et al., 2011]. Geometrical optics ray-tracing techniques need to have a sufficient number of rays-per-cell to accurately represent the beam and to capture the energy deposition of the laser to the target.

Advanced ray-tracing models that go beyond geometrical optics and consider the intensity, polarisation and spectrum are an area of active research and are constantly being developed. For ICF simulations it would be ideal for simulations to be able to model the laser speckle intensity distribution to accurately demonstrate the back and side scattering of light that arises from wave mixing processes [Ruyer et al., 2022]. One scheme of ray-tracing that is able to capture these aspects of lasers is Paraxial Complex Geometric Optics (PCGO) [Kravtsov and Berczynski, 2007] and has been effective in modelling the laser losses from CBET [Colaïtis et al., 2016]. PCGO models the laser as a Gaussian beam and calculates the diffraction as it travels through the inhomogeneous plasma. All methods that involve Gaussian beams lead to a series of ordinary differential equations; a system of comlex linear equations of the paraxial ray approximation and a complex nonlinear Riccati equation [Theaker and Gorder, 2013]. Another model of ray-tracing that has been successful in capturing wave mixing processes is Monte Carlo variation of the stationary ray-tracing method, which uses a probability distribution to model the creation and annihilation of rays that happen due to scattering and other energy exchange processes [Debayle et al., 2019].

These advanced methods provide a much closer physical description for the lasers in ICF experiments, but come at a computational cost and are not without fault. Given the various sources of error that exist within radiation-hydrodynamic codes, such as: the resolution of tabulated data; equation-of-state, opacity and emissivity tables used for radiation-transport; thermal conduction calculations; the accuracy of the hydrodynamic calculations and the other approximations that are used to simplify the complex equations, the benefit of implementing such complicated ray-tracing schemes has not been quantified [Baldwin et al., 1999]. As such, it was decided in the interest of computation and cost-effective simulations that we would implement a more basic ray-tracing scheme closer to the classic methods.

3.1.2 Wedge Boundary Conditions

For simulations in which the laser energy deposition across the capsule is uniform, the results are pseudo-1D and it is not necessary to conduct the simulations using the full domain. In this scenario, symmetric boundary conditions can be applied

[Denton and Hu, 2009], which allows a small segment or *wedge* of a capsule to be simulated. This significantly reduces the computational cost of simulations and can produce identical results, as demonstrated later in fig. 3.12.

In addition, *wedge* boundary conditions have benefits over “no-slip” boundary conditions [Day, 1990], in which the domain is fixed along a certain axis. For ICF simulations in which a RZ domain is used, no-slip boundaries are used to fix the poloidal angle of the grid. Such a property means that the *wedge* can be arbitrarily resolved, and high-mode perturbations, such as speckles, can be simulated. A full description of the implementation of these boundary conditions is given below.

3.1.3 Laser Non-Uniformities

To simulate the laser non-uniformities as outlined in section 1.6.1, a routine can be implemented to the ray-tracing interface of a hydrodynamics code. Such features have been implemented into the 2D radiation-hydrodynamic code DRACO, and have been used to study the effects of various sources of non-uniformity in inertial fusion experiments [Denton and Hu, 2009, Hu et al., 2010].

3.2 Ray-tracing

3.2.1 Implementation

The ray-tracing routine was implemented using the assumptions of geometric optics in a manner similar to that as described in [Temporal et al., 2001]. Rays are treated as a species of particle that are free to move throughout the domain during each timestep, under the assumption that the ray propagation time is negligible compared to the hydrodynamic evolution of the fluid. Initially, the rays are outside the computational domain and are projected to the grid edge, as described later in section 3.2.2.

Once inside the domain, the ray deposits its energy through inverse bremßtrahlung in each cell, and its trajectory angle is updated at cell interfaces according to the plasma conditions using the vector form of Snell's law (eq. (3.2)), which is valid for 2D and 3D rays. To propagate to the next cell, the routine conducts a scan of neighbouring cells before choosing a trajectory to the cell that has the smallest distance. This is described in further detail in section 3.2.2. The indices of the new cell are used to obtain the plasma parameters (T_e, ρ, n_e and η) needed to calculate the energy deposition and update the trajectory angle. This process repeats itself until either the ray has left the domain, or it has deposited all of its energy.

For the regions of the domain where the electron number density has a specific value, some processes are triggered. If the ray reaches the critical density, n_{crit}, this activates both the reflection of the ray and additional energy deposition through resonance absorption. At the quarter critical density, $n_{crit}/4$, *Odin* uses a fraction of the rays energy to generate a population of hot electrons to mimic the mechanism of LPIs. In reality, LPIs are generated over a larger range of densities that extend up to the quarter-critical density, and also at the critical surface as discussed in section 1.6.5.

Snell's Law

The direction, θ of a ray travelling through media of differing refractive indices, η is described by the common form of Snell's law:

$$\eta_1 \sin(\theta_1) = \eta_2 \sin(\theta_2) \tag{3.2}$$

where η_i is the refractive index of the medium, and θ_i is the angle of trajectory, relative to the surface normal, of the ray travelling through its respective media. For plasma, the refractive index, η is a function of the electron number density, n_e, and the critical density of the incoming laser, n_{crit} (defined in eq. (1.40)):

$$\eta = \sqrt{1 - \frac{n_e}{n_{crit}}} \tag{3.3}$$

The vector form of Snell's law, as implemented into *Odin* is separated into its refractive and reflective versions [Glassner, 1989]. The equation for refraction is given by,

$$\vec{v}_{refract} = \left(\frac{\eta_1}{\eta_2}\right)\vec{l} + \left(\frac{\eta_1}{\eta_2}\cos\theta_1 - \cos\theta_2\right)\vec{n} \tag{3.4}$$

and the reflective form is shown below,

$$\vec{v}_{reflect} = \vec{l} + 2\cos\theta_1\vec{n}. \tag{3.5}$$

In these equations, $v_{re\vec{f}ract}$ and $v_{re\vec{f}lect}$ are the new direction vectors of the refracted and reflected ray, respectively, θ_1 is the angle of incidence with respect to the surface normal, and θ_2 is the angle of refraction with respect to the surface normal. $\vec{l}$ is the normalised incoming light vector and $\vec{n}$ is the normalised plane normal vector as shown in fig. 3.1.

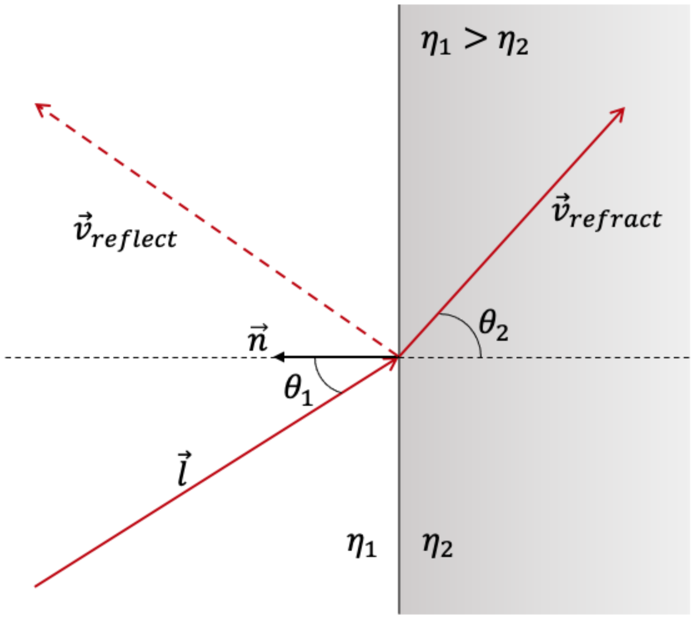

Figure 3.1: A schematic diagram depicting Snell's law. The incoming light vector is denoted by $\vec{l}$ and the corresponding refracted and reflected light vectors are shown by $\vec{v}_{refract}$ and $v_{reflect}$, along with their angles θ. In this scenario, the medium shows a plasma where the refractive index on the left hand side of the interface, η_1 is greater than the refractive index on the right, η_2.

3.2.2 Routine setup

The ray-tracing is controlled through the input deck. The key parameters are shown in Table 3.1. A discussion of these parameters and their functionality will be giving in the remainder of this subsection.

Projection into domain

The routine has two settings for the initial ray geometry at the remote laser ports. Either the rays are spread uniformly around the domain, using a specified number of rays per cell (polar angle), such that all regions of the capsule experience equal intensities of rays, or the ray positions (x, y, z) and direction vectors (l_x, l_y, l_z) can be read from a *.txt* file.

In both geometries, the initial positions must be positioned significantly further out than the extent of the domain to allow for the expansion of the grid domain during the ablative phase of the implosion. If the initial positions of the rays are within the domain, they are re-positioned ×10 further outwards, conserving their

Input parameter	**Value**	**Default**	**Use**
beam_lambda	Numeric	3.51×10^{-7}	Set laser wavelength
use_paths_2d	Boolean	True	2D ray-tracing
use_paths_3d	Boolean	False	3D ray-tracing
use_ray_refraction	Boolean	True	Ray refraction
use_ray_reflection	Boolean	True	Reflection at the critical surface
rays_on_face_centre	Boolean	False	Cell-centred rays
nrays_per_cell	Numeric	1	Number of rays per cell
nrays	Numeric	1	Total number of rays
resonant_absorption_fraction	Numeric	0.15	Fraction of energy for RA
use_laser_deposition_filter	Boolean	False	Binomial filtering
laser_deposition_weight	Numeric	0.5	Filter weighting
use_face_normal_interpolation	Boolean	True	Interpolate face normal

Table 3.1: Table of the *Odin* input deck parameters that are relevant to the ray-tracing routine.

position angle and direction vector in the process. At this new position, the rays must be projected to the outer surface of the domain, no energy is lost or deposited by the ray until it is within the grid domain.

For this, a projection routine was added. It works in two stages: an initial line-sphere intersection, followed by a line-plane intersection. The initial line-sphere intersection assumes a sphere that is 1% larger than the extent of the domain, and is done by setting the equation of a sphere, equal to that of a line. The equation of a sphere is given by,

$$|\vec{x}-\vec{c}|^2 = r^2 \tag{3.6}$$

where $\vec{x}$ is a point on a sphere, $\vec{c}$ is the centre point of the sphere, and r is its radius. The equation of a line is,

$$\vec{x} = \vec{o} + d\hat{u} \tag{3.7}$$

where $\vec{x}$ is a point on the line, $\vec{o}$ is the origin point, d is the distance along the line from the origin, and $\hat{u}$ is the normalised direction vector of the line. Assuming a centre point, $\vec{c}$, at the origin and equating both equations yields the following result,

$$d = -\frac{(\hat{u}\cdot\vec{o})}{|\hat{u}|^2} \pm \frac{\sqrt{\Delta}}{2|\hat{u}|^2} \tag{3.8}$$

where,

$$\Delta = (2(\hat{u} \cdot \vec{o}))^2 - 4(|\vec{o}|^2 - r^2). \tag{3.9}$$

This determines the nature of the line-sphere intersect and has the following results,

- If $\Delta < 0$, then no solutions exist (no intercept).
- If $\Delta = 0$, then exactly one solution exists.
- If $\Delta > 0$, two solutions exist.

Note that in the case where two solutions exist for the intersection between the line and sphere, the routine will choose the solution with least distance. If the ray intersects with the sphere, it will be projected to that position, and a final line-plane intersection will be carried out.

The planes under consideration for intersection are only on the outer surface of the domain. Note that for a 3D domain, the original 2D R-Z grid is rotated around the azimuthal direction and has a finite number of cells in this direction N_ϕ which are connected by straight lines. This means that the 3D grid differs from a perfectly spherical grid, as shown in the figure below. By iterating across the grid domain in poloidal and azimuthal directions, the routine will find a cell that corresponds with the nearest point of intersection for the ray to the grid domain. The ray is projected to this plane on the outer surface of the domain and its initial indices are determined. Subsequent rays use the indices of the previously projected ray intersect and check if indices also match their intersect. The check consists of calculating the cross products of the ray vector with the face normals of the vertices within the cell. If all cross products have the same value sign (±), then the ray lies within the cell. However, if this check fails, the ray is displaced by a small amount to ensure that the missed projection is not due to rounding errors, and the scan is repeated. The methodology of line-plane intersections is described in the following subsection.

Path Update

Once the rays have entered the domain, they will be refracted by the plasma according to eq. (3.4) and eq. (3.5). Their paths can only be updated at cell interfaces, and the accuracy of the scheme relies on the resolution of the refractive index. From a ray-tracing perspective, the benefit of using a Lagrangian mesh is that the cells at more dense regions of the target are tightly packed as a result of hydrodynamic compression and also for the purposes of cell-mass matching. This implies that the critical surface of the plasma is likely to be well-resolved during the ablation of the target.

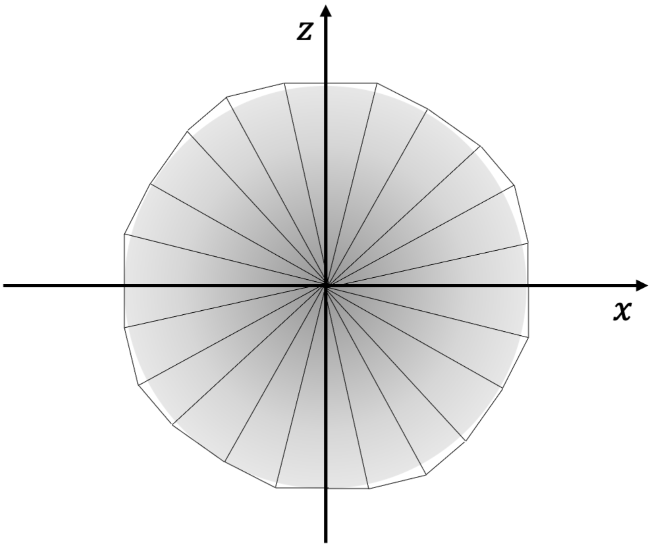

Figure 3.2: A rotated 2D $R - Z$ *Odin* grid rotated in the azimuthal as seen from above (the $\vec{y}$ direction). Note that the cells are connected by straight lines and differ from a perfectly spherical domain.

As the rays travel to the next cell in their trajectory, a local scan of line-plane intersections, with cells of indices ±1 from the current i (radial), j (poloidal) and k (azimuthal) indices of the ray is conducted. The distance, d of a line-plane intersection is given by,

$$d = \frac{(\vec{p_0} - \vec{l_0}) \cdot \vec{n}}{\vec{l} \cdot \vec{n}} = |d\vec{S}| \tag{3.10}$$

where $\vec{p_0}$ is a point on the surface of the plane, l_0 is the starting point of the line (ray), $\vec{l}$ is the direction vector of the line, $\vec{n}$ is the face normal of the place, and $d\vec{S}$ is the direction vector of the intersection. The intersect with the shortest positive distance yields the correct cell for the ray to travel to. An example of how a 3D ray might travel through a planar domain is shown below in fig. 3.3.

Energy deposition

As discussed in section 1.5, a laser delivers its energy to a plasma through inverse bremßtrahlung (IB), resonance absorption, and coupling to hot electrons. The rays deposit energy through IB into cell volumes along their trajectory as described in section 2.3.3. At the quarter-critical density, $n_{crit}/4$, a fraction of the laser energy is used to generate a population of hot electrons with a user-defined temperature and angular spread (as discussed in section 2.3.1). Once the rays reach the critical density,

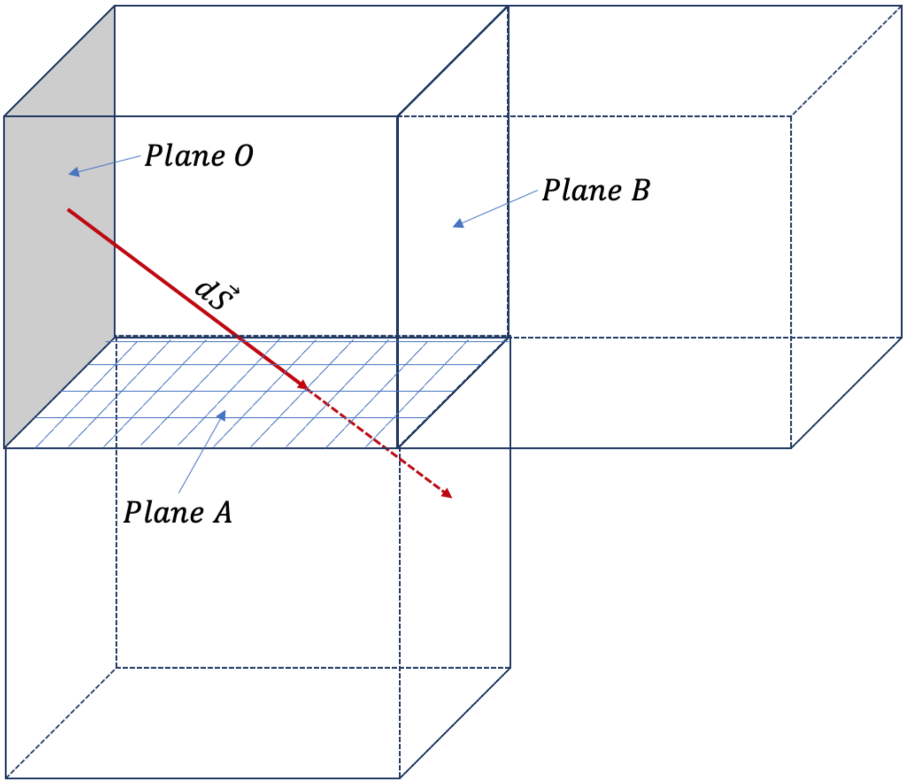

Figure 3.3: An image showing a ray travelling through a 3D planar domain. For a ray travelling from plane O, the routine would find two intersections, once at Plane A and again for Plane B. In this scenario, the routine would choose the path of least distance, to *Plane A*, as highlighted by $d\vec{S}$.

they will deposit a user-specified fraction of their remaining total energy, which is typically set to 0.15 [Estabrook et al., 1975], to replicate resonance absorption.

Face-Normal Interpolation

In ICF simulations that use a cylindrical coordinate domain when using several rays per cell, rays that are positioned away from the centre of the cell are more significantly refracted since their angle of incidence is overestimated with respect to the face normal at the centre of the cell interface. The reason that this occurs is because the *Odin* grid discretises a curved target, and cell nodes are connected by straight lines that cannot replicate the changing surface normal of a sphere. At each cell interface, the rays accumulate a small displacement in their trajectory. As they approach the critical surface, the discrepancy can become so large that rays overlap each other and focus into channels that no longer accurately represent the trajectory of a beam. This effect is known as artificial filamentation and an example is shown in fig. 3.4. As the rays travel in these focused channels, they preferentially deposit their energy in certain cells and can seed numerical perturbations. Note that this is not an issue for planar target simulations.

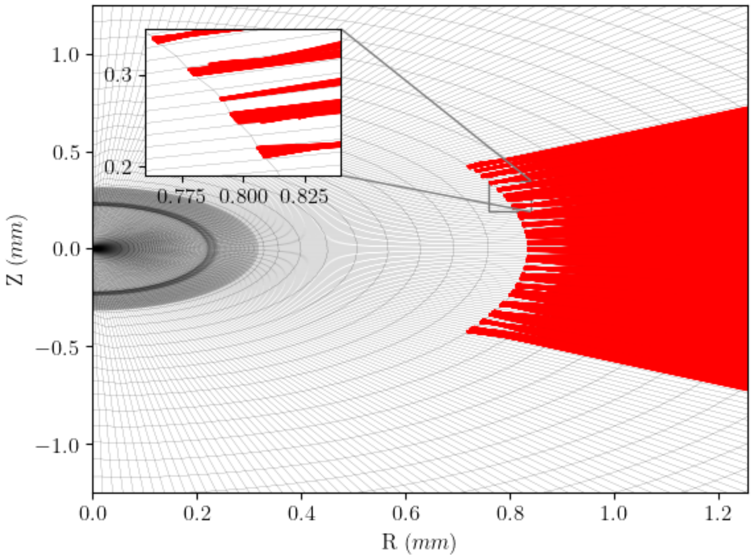

Figure 3.4: A snapshot from an *Odin* simulation, showing artificial filamentation of a fraction of the rays. An inset figure shows a zoomed image of the area of interest.

To avoid artificial filamentation it must be ensured that rays trace their physical path. The reason that the rays are focusing is because the normalised plane vector, $\vec{n}$, is only correct for rays that are orthogonally incident to the centre of the cell plane. Rays that are off-centre will have a higher angle of incidence that causes them to refract more quickly. For a curved target, the face normal is constantly changing in the poloidal direction and rays are refracted accordingly, but for computational domains the resolution is limited, and the face normal along the outer surface is discretised meaning that ray trajectories entering between two defined face normals will have an incorrect trajectory. In *Odin*, cells are joined by straight lines, so it does not fully replicate a spherical target.

To correct this, it is necessary to calculate the effective face normal vector that would arise for a ray at that position on a curved surface, *i.e* face normal interpolation. For a ray that lies off-centre in a given cell, the neighbouring face normal vectors, $\vec{n_j}$ and $\vec{n_{j+1}}$, are stored, and the relative distance of the ray between the two normals is calculated. This distance is used to obtain an interpolated value for the face normal, $\vec{n_{j'}}$, that is calculated using a normalised distance between the two neighbouring cell normals. This allows rays to travel the path that they would in any curved shape target as shown in fig. 3.5. Note that the discretisation of a curved surface also means that the rays enter the cells at a shifted location, but this difference appears to be insignificant in comparison to artificial filamentation and is ignored.

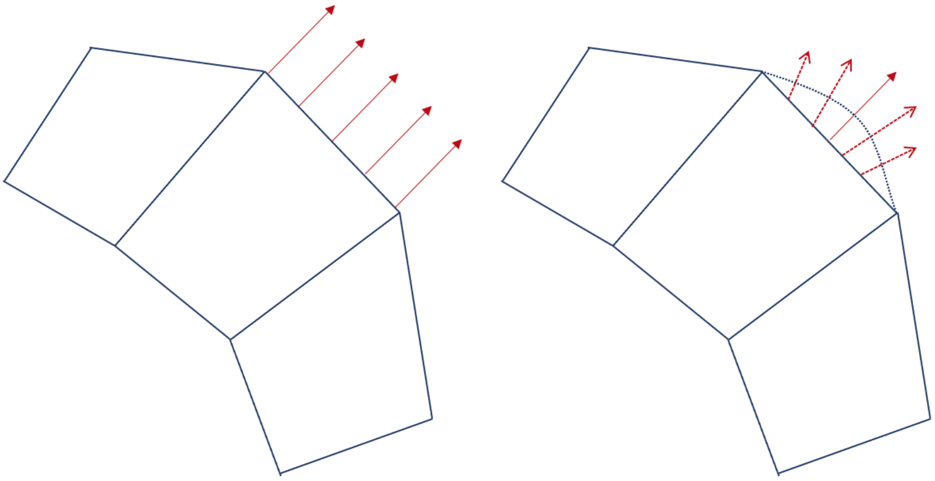

Figure 3.5: A schematic diagram showing the effective impact of applying face-normal interpolation. The left hand side shows the handling of face-normals prior to interpolation, and the right hand side shows the effective face-normal afterwards.

Binomial Filtering

In simulations where few rays are used (<5 rays per cell) to represent the beams, laser energy deposition will preferentially heat cells that experience a higher flux of rays. If such low ray resolutions are necessary, perhaps for computational efficiency, the energy deposition can be smoothed over neighbouring cells using binomial filtering to replicate the statistical effects of using a higher ray resolution.

To negate the effects of this preferential heating, we implemented a Binomial filtering energy deposition. Binomial (or Gaussian) filtering is the process of spreading a signal or parameter over a number of neighbouring cells/pixels as shown in fig. 3.6. The filter is applied by changing the original energy deposition, $E^0_{i,j}$, in a cell with

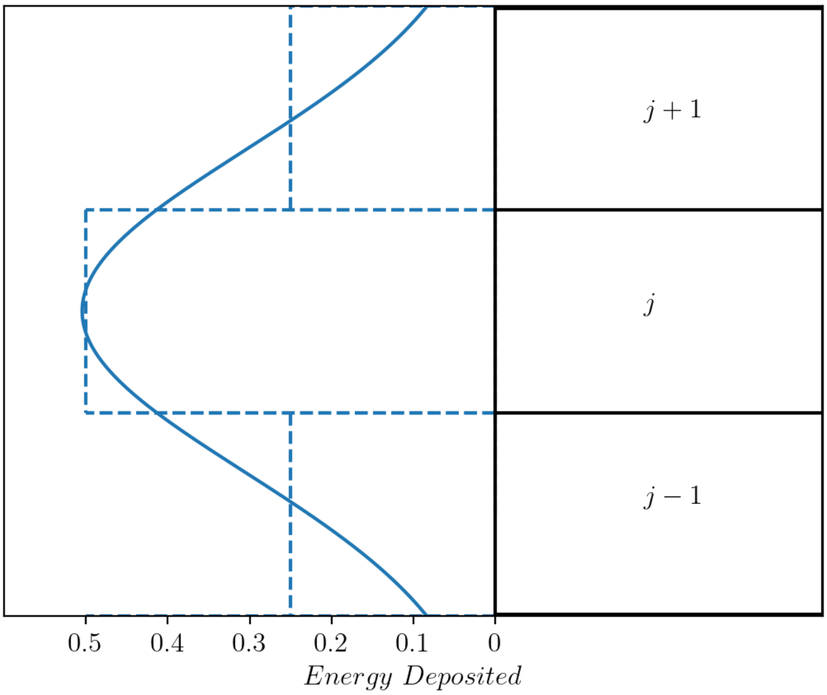

Figure 3.6: A 1D graphical representation of energy smoothing due to Binomial filtering.

indices (i, j), to a new value, $E_{i,j}$, using a Binomial weighting, W,

$$E_{i,j} = \frac{1}{1+2W}\Big(E^0_{i,j} + W(E^0_{i,j-1} + E^0_{i,j+1})\Big). \tag{3.11}$$

Note that this equation only represents Binomial filtering in 1D, it can also be applied in 2D where laser energy deposition is also smoothed radially. Typically W is set to 0.5.

3.2.3 Performance

In this subsection we will present the accuracy of the ray-tracing scheme in terms of trajectories.

Refraction

The best way of quantitatively assessing the accuracy of ray trajectories in this scheme is to look at their refraction in a given test case. To check the trajectories against an analytic solution, we set up a test case of a planar slab of plasma with a linear number density profile that only varies in the x direction,

$$n_e(x) = n_{crit}(1.0 - x) \quad (x \in [0, 1]) \tag{3.12}$$

where n_{crit} is the critical density of the plasma as shown in eq. (1.40).

For this linear density plasma, it is possible to calculate an analytic formula for the ray path. Starting with Snell's law (eq. (3.2)), the product of the refractive index, η, and the sine of the angle of incidence, $\sin(\theta)$, is defined by a constant, k.

$$\eta \sin(\theta) = k \tag{3.13}$$

We consider a ray entering a medium with an angle of incidence of θ, that sketches out an arbitrary triangle with sides dy and dx. In this scenario, it follows that $\tan(\theta) = dy/dx$. Or, equivalently,

$$\frac{dy}{dx} = \frac{\sin(\theta)}{\cos(\theta)} = \frac{\sin(\theta)}{\sqrt{1 - \sin^2(\theta)}} \tag{3.14}$$

Now we can substitute in eq. (3.13):

$$\frac{dy}{dx} = \frac{\frac{k}{\eta}}{\sqrt{1 - \left(\frac{k}{\eta}\right)^2}} = \frac{k}{\sqrt{\eta^2 - k^2}} \tag{3.15}$$

Note that the refractive index is a function of the number density, which, in our test case, is a function of x only. Therefore, we can write it as:

$$\eta(x) = \sqrt{1 - \frac{n_e(x)}{n_{crit}}} \tag{3.16}$$

$$\eta(x) = \sqrt{1 - \frac{n_{crit} \times (1 - x)}{n_{crit}}} = \sqrt{1 - (1 - x)} = \sqrt{x} \tag{3.17}$$

We substitute this function of $\eta(x)$ into eq. (3.15),

$$\frac{dy}{dx} = \frac{k}{\sqrt{x - k^2}} \tag{3.18}$$

Integrating between the initial coordinates of the ray (x_0, y_0), and some point along its trajectory, (x, y),

$$\int_{y_0}^{y} dy = k \int_{x_0}^{x} \frac{dx}{\sqrt{x - k^2}}, \tag{3.19}$$

which has the solution:

$$y(x) = C \pm 2k\sqrt{x - k^2}. \tag{3.20}$$

C is an integration constant, which describes the mid y point of the ray during its trajectory and it is determined by the initial position of the ray (x_0, y_0), i.e.

$$C = y_0 - k\sqrt{x_0 - k^2} \tag{3.21}$$

Mathematically, the square root term describes the inward and return paths of the ray, *i.e* one will be positive and the other negative.

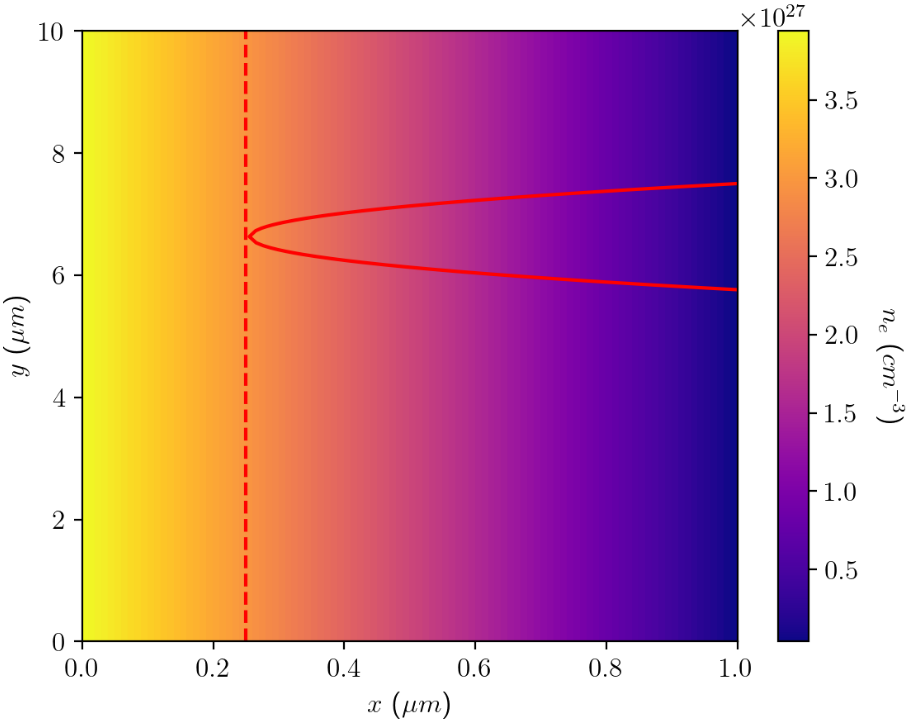

Figure 3.7: A colour map showing a ray travelling through a planar material with a linear density profile as described in eq. (3.12). The ray refracts as it travels through the medium, and changes direction at the turning point as calculated in eq. (3.22). A dotted line is plotted at the turning point.

The furthest extent of x can be evaluated by re-arranging the above equations and inserting some initial conditions. For a ray with initial conditions, $x_0 = 1.0$,

$y_0 = 7.5$, and $\theta_0 = \pi/6$ the turning point is given by:

$$x_T = \frac{k^2}{2} = 0.25 \tag{3.22}$$

Note that the turning point is independent of the initial y-coordinate, which is expected given that the density is only a function of x. For normal incidence ($\theta = 0$), the ray reaches the critical density, and the effective turning point in this scenario is called the critical surface. Otherwise, the ray refracts as it travels through the plasma and reaches a turning point that is dependent on its angle of incidence as shown in fig. 3.7.

The ability of this routine, which refracts at interfaces, to accurately trace the path of the ray is dependent on the resolution of the domain and its density profile. There can be a tendency for rays to refract before the critical surface. Figure 3.6 shows the results of an investigation to the accuracy of the scheme and its ability to reflect a ray at the turning point of a planar plasma, with a linear density profile as described above, for grid resolutions between N_x =100-1000. The markers (blue) show the average error of the routine for a given grid resolution for a range of angles of incidence between 1°-50°, and the shaded (grey) region shows the extent of those errors. The scheme shows reasonable accuracy for low resolutions, and is able to find the critical surface to $\sim 2\%$ at $N_x = 100$. Low resolutions show a larger range of error, with a maximum error of $\sim 12\%$. Large errors in turning point occur for higher angles of incidence where the ray refracts over a shorter scale length. This error decreases with better resolution, with the most significant relative improvement occurring in the change from $N_x = 100$ to 200. In addition, the extent of the errors at each resolution, shown as the shaded region, converges to smaller values as the resolution increases. At angles of incidence of 0°, the ray travels in a straight line and reflects off the critical surface so that case is not a fair test for the refractive capability of the routine. The error in turning point was calculated as $\alpha_{turn} = (x - x_{turn})/x_{turn}$.

For the majority of ICF simulations run with *Odin*, the grid would be polar as shown in fig. 3.9. Unfortunately, an analytic solution to the ray path in cylindrical coordinates for a radial density profile cannot be found, so it was not possible to quantify the accuracy of the scheme in these conditions. Numerical solutions for ray trajectories in this reference frame have been investigated for certain conditions [Montes and Hubbard, 1979].

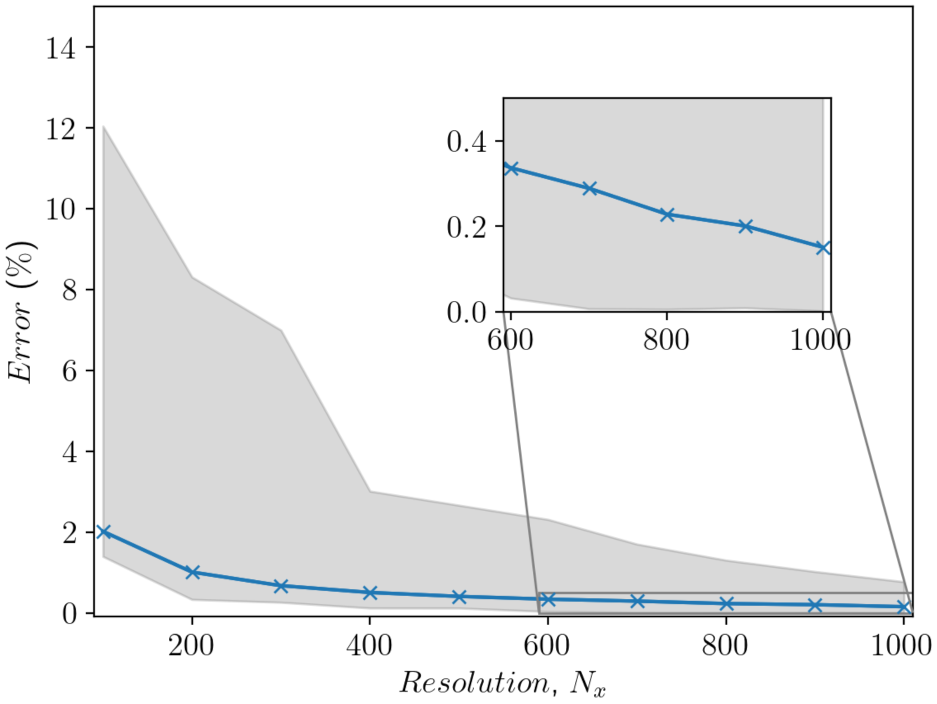

Figure 3.8: The turning point error of the ray-tracing scheme in the planar, linear density test case of eq. (3.12), tested for a range of angles of incidence between $\theta = 1° - 60°$. Note that the blue line highlights the average error for the scheme at that resolution, and the shaded grey region shows the extent of the minimum and maximum errors. An inset plot shows a zoomed region of the error values for $N_x = 600 - 1000$.

Energy Deposition

The majority of energy deposition is done through inverse bremßtrahlung which can be calculated analytically (eq. (1.45)) given the density and temperature of the plasma that the ray is propagating through. For 2D ray-tracing, the energy of the rays is weighted by a cosine factor that replicates deposition to a 3D target. By comparing with the analytic solution, the energy deposition of the ray-tracing is in good agreement, with a deviation $\Delta E < 1\%$. Note that energy deposition is dependent on the resolution of the grid domain. A simulation study conducted on *Odin* suggests that for typical ICF simulations with a radial domain of $1mm$, deposition is fairly accurate beyond 200 radial cells, and the results converge beyond 300 radial cells.

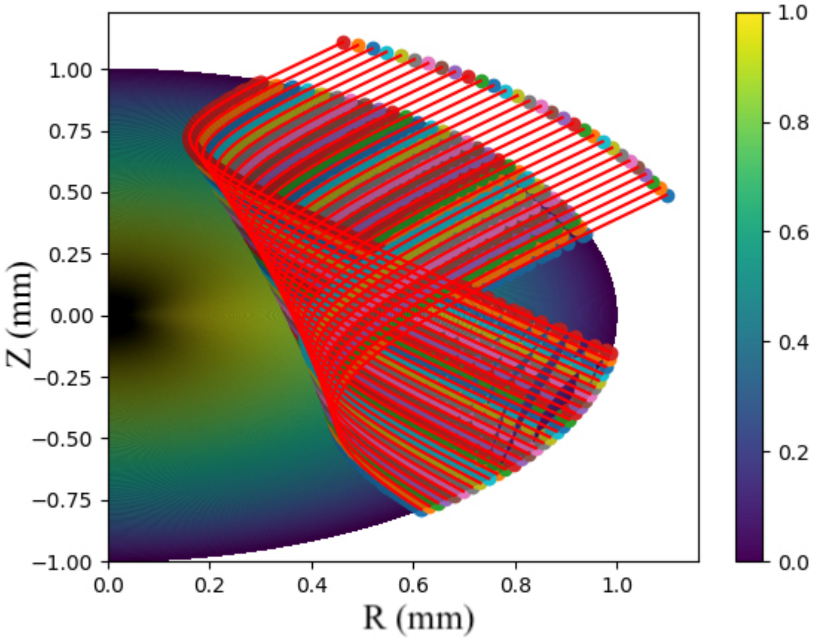

Figure 3.9: The refraction of rays in a linear density capsule in *Odin*. All rays have identical direction vectors but are positioned at varying poloidal angles of the capsule, therefore giving each ray a different angle of incidence and trajectory. Note that the density *colormap* is normalised with the critical density value shown as 1.

3.3 Wedge Boundary Conditions

3.3.1 Implementation

For simulations of uniform implosion, or high l-mode perturbations ($l > 100$), running an entire hemispherical simulation is unnecessary and adds additional computational cost and time. To use a grid domain that only uses a small segment of a spherical target, we developed a boundary condition that allowed the user to run a simulation with a thin "wedge" domain. These boundary conditions allowed the grid to be located at any position around the capsule (in solid angle), and with only 3 poloidal cells needed for *Odin*'s thermal conduction to be included due to the 9-point stencil it uses.

The boundary conditions mirror the cell properties from the lowest poloidal cell to the highest poloidal ghost cell, and vice versa. This leaves the cells free to move and rotates the grid parameters accordingly. Note that this is applied over all radial cells, so we drop notation for this index. For simplicity, we consider a small wedge domain with 2 poloidal cells, each with an angular resolution of $\Delta\theta$, (as shown in fig. 3.10) we can derive the transformations needed for these boundary conditions. Note that we use the notation $y_1 = y(ny-1)$, $y_0 = y(ny)$, and $y = y(ny+1)$.

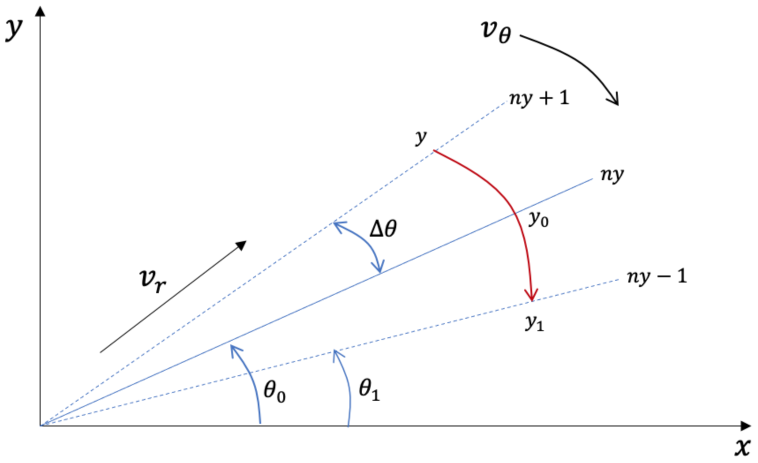

Figure 3.10: A schematic diagram showing the positions and indices of the parameters associated with wedge boundary conditions. v_r is the radial velocity of the cells, v_θ is the angular velocity, and $\Delta\theta$ is the angle between neighbouring cells, e.g $\theta_0 - \theta_1$.

The rotation of a 2D point (x_1, y_1) by an angle α is given by,

$$\begin{pmatrix} x \\ y \end{pmatrix} = \begin{pmatrix} \cos\alpha & -\sin\alpha \\ \sin\alpha & \cos\alpha \end{pmatrix} \begin{pmatrix} x_1 \\ y_1 \end{pmatrix} \tag{3.23}$$

Where (x, y) are the coordinates of the rotated point, and for wedge boundary conditions, $\alpha = 2\Delta\theta = 2\theta_0 - 2\theta_1$. Using the trigonometric identities, we can obtain expressions for $\cos\alpha$ and $\sin\alpha$ in terms of x and y, needed for the upper boundary conditions. We have,

$$\cos\alpha = \cos(2\theta_0 - 2\theta_1) = \cos 2\theta_0 \cos\theta_1 + \sin 2\theta_0 \sin 2\theta_1 \tag{3.24}$$

and,

$$\sin\alpha = \sin(2\theta_0 - 2\theta_1) = \sin 2\theta_0 \cos 2\theta_1 - \cos 2\theta_0 \sin 2\theta_1 \tag{3.25}$$

Using appropriate substitutions and trigonometric identities, such as $\cos\theta_i = x_i/r_i$

and $\sin\theta_i = y_i/r_i$, we can obtain the following expression for eq. (3.24) and eq. (3.25):

$$\cos\alpha = \frac{(x_0^2 - y_0^2)(x_1^2 - y_1^2)}{r_0^2 r_1^2} - 4\frac{x_0 y_0 x_1 y_1}{r_0^2 r_1^2} \tag{3.26}$$

and

$$\sin\alpha = 2\frac{x_0 y_0}{r_0^2}\frac{(x_1^2 - y_1^2)}{r_1^2} - \Big(\frac{x_0^2 - y_0^2}{r_0^2}\Big)2\frac{x_1 y_1}{r_1^2} \tag{3.27}$$

A similar treatment can yield the rotation values for the lower wedge boundary conditions.

For the cell velocities at the boundaries, we must also consider the rotation and the transformation from Cartesian to cylindrical coordinates. Note that the ghost cells will have the same v_r as the cells within the domain, but v_θ is dependant on the position, θ, of the ghost cells. v_θ can be calculated as,

$$v_\theta = v_x \sin\theta - v_y \cos\theta. \tag{3.28}$$

Here,

$$v_x = v_r \cos\theta_1 - v_\theta \sin\theta_1 \tag{3.29}$$

and

$$v_y = v_r \sin\theta_1 + v_\theta \cos\theta_1. \tag{3.30}$$

Note that these equations are applicable for both the upper and lower boundary ghost cell velocities.

3.3.2 Routine Setup

Initialising *wedge* boundary conditions is done in the input deck. Both input parameters for the y-boundary conditions, **ybc_min** and **ybc_max**, need to be set to **wedge**. Once that is applied, all other aspects of *Odin* will change accordingly. Wedge boundary conditions allow for the use of both 2D and 3D, for rays and electrons routines. A comparison between a typical *wedge* simulation domain and a full hemispherical capsule is shown in fig. 3.11. The simulation results are dependant on domain size and resolution, as discussed in the following section.

3.3.3 Performance

To test the implementation of the *wedge* boundary conditions and its ability to reproduce uniform implosion results, we conducted a series of simulations using different dimensional arrangements in *Odin*. We simulated a 1D simulation with 3

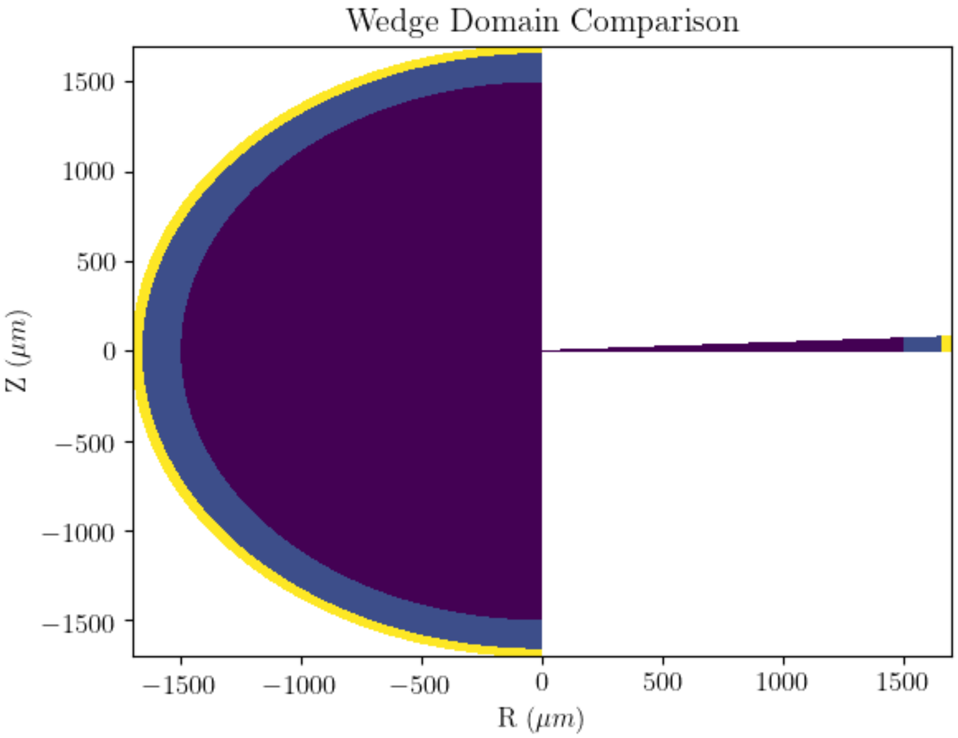

Figure 3.11: The domains of a full hemispherical simulation (left) and a typical *wedge* simulation (right) with an angle of 2.7°, shown next to each other for comparison.

poloidal cells spanning between 0° and 2.7°, a 2D simulation using a full hemispherical domain and 2D ray-tracing, and a 2D domain simulation with 3D ray-tracing. A snapshot showing the comparison of the different simulations is shown in fig. 3.12.

Each simulation is in good agreement, and the 1D and 2D simulations yield identical results. The small difference in density profiles is likely to have arisen from different timing of the output snapshots. The data of *Odin* is given at user-defined intervals, but the timesteps do not always lineup with the requested time, so there is a margin of error, $\sim 0.01ns$, in output timing. In addition, the energy deposition of the ray-tracing scheme is dependent on the path length of the rays between cells. For 3D ray-tracing the path lengths are bound to differ from the 2D version because of the rotated RZ grid, hence the reason for preferring 3D ray-tracing over a 2D RZ projection given that the port arrangement of the beams is inherently 3D. This difference in energy difference between dimensional schemes also leads to differing hydrodynamic timing. Note that the 1D simulation was $\sim \times 10^2$ faster to run than the 2D simulation and another order of magnitude faster than 3D.

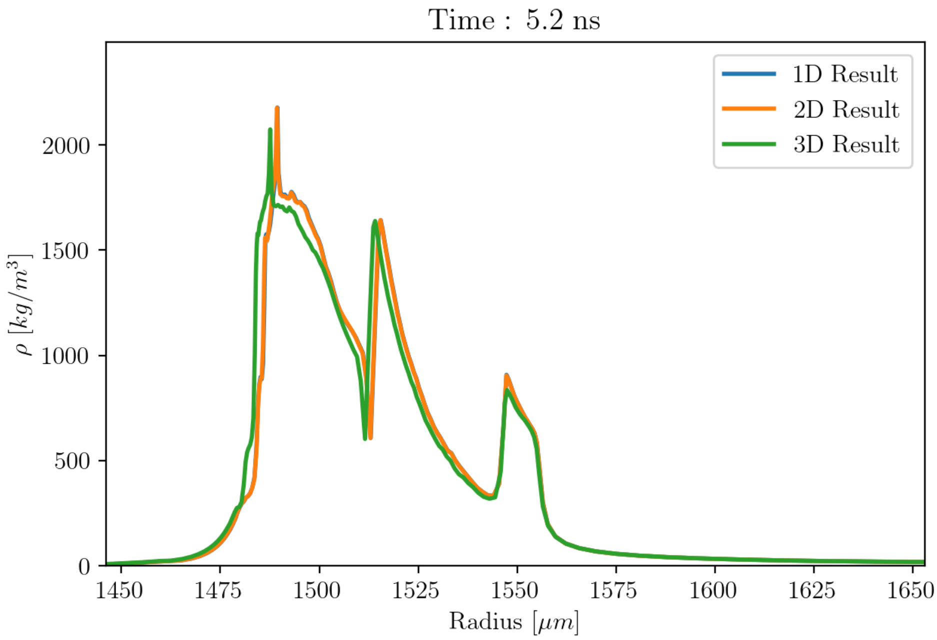

Figure 3.12: A snapshot of 3 different simulations (1D, 2D and 3D), showing a zoomed density profile at $t = 5.2ns$. Each simulation is colour coded and labelled in the legend. The simulation setup is the Craxton *et al.* 3 picket direct-drive as detailed in [Craxton et al., 2015].

3.4 Laser Non-Uniformities

3.4.1 Implementation of l mode perturbations

To replicate the non-uniformities seen on experimental ICF facilities (section 1.6.1), we implemented a series of features into *Odin's* ray-tracing scheme.

Perturbations in the laser illumination on the surface of the target are applied by modifying the power distribution of the lasers in the poloidal direction of the target. It is implemented through the following equation:

$$P_{rel} = P_0 \times \big(1.0 \ + \ a_p \sin(l\pi\theta)\big) \tag{3.31}$$

where P_{rel} and P_0 are the perturbed and initial power values of the laser respectively, a_p is the amplitude of the perturbation, l is the perturbation mode, and θ is the angle of the rays/beam. This perturbation is applied by modulating the power of the beams. For the same perturbation to be applied to the number of rays, the modulation requires a large number of rays (N_{rays}¿1000 at the equatorial cell), therefore, to save on computational cost we modulated the power. Note that there are no limits on the amplitude or mode of perturbation, so high-mode perturbations such as those that occur from speckles can be simulated.

The laser-target offset is implemented by shifting the initial positions of the rays by a user-defined amount in the R and Z directions. This offset has implications on the ray trajectories, since the rays are no longer incident to the surface normal of the target, but face-normal interpolation ensures that the refraction is still executed correctly.

3.4.2 Routine Setup

To set laser non-uniformities in simulations, the options are defined in the input deck of *Odin*. The key parameters for introducing laser non-uniformities are shown in Table 3.2.

Input parameter	**Value**	**Default**	**Use**
use_perturbations	Boolean	False	Laser power perturbation
perturbation_amplitude	Numeric	0.05	Perturbation amplitude fraction
perturbation_mode	Numeric	1.0	l-mode of perturbation
perturbation_file	Character	‘’	File with perturbation values
target_x_offset	Numeric	0.0	x laser offset
target_y_offset	Numeric	0.0	y laser offset

Table 3.2: Table of the *Odin* input deck parameters that are relevant to the laser non-uniformities.

3.4.3 Performance

The implementation of the laser non-uniformities was successful and showed characteristic changes in the energy deposition and plasma parameters.

Simulations with harmonic perturbations in the laser power are shown below in fig. 3.13. Each of these simulations used a domain with a radial resolution of $N_r = 302$ and an angular resolution of $N_\theta = 300$, and had 50 rays per angular cell. The laser rays were distributed uniformly around the capsule and aimed at the centre of the target. The target is a cryogenic DT capsule using the same configuration as described in section 1.4.6. This figure shows a snapshot of 4 different applied l-mode perturbations ($l = 1, 4, 6$ & 8), at $t = 9.5ns$. This time was chosen because the power modulations have had sufficient time to influence the density profile of the targets.

Simulations of an $l = 5$ harmonic perturbation are shown for amplitudes, $a = 1$ & $a = 8$ in the figure below (fig. 3.14). These snapshots were also taken at

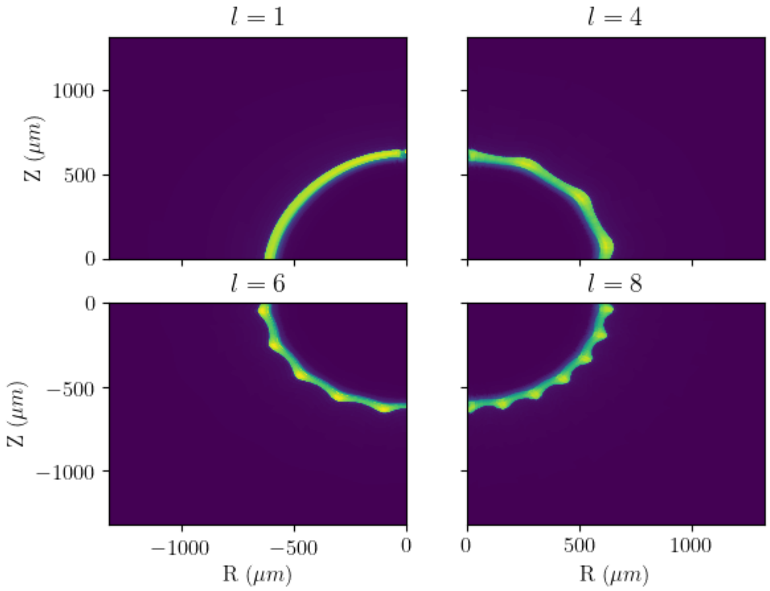

Figure 3.13: The density profiles of imploding capsules at t=9.5ns, with various applied l-mode perturbations in their power profile as specified in their titles. Note that all perturbations have a 5% amplitude.

$t = 9.5ns$. Note that the modulation in the density profile becomes more noticeable for higher amplitude power perturbations.

A simulation with of an unperturbed capsule and capsule with a laser offset of $+50\mu m$ in the y-direction is shown in fig. 3.15. The plot on the right shows that the capsule has been shifted downwards due to the force applied by the laser. Additionally, the plot shows that the simulation with the applied laser offset does not produce such high densities during the implosion phase, when compared to the unperturbed case.

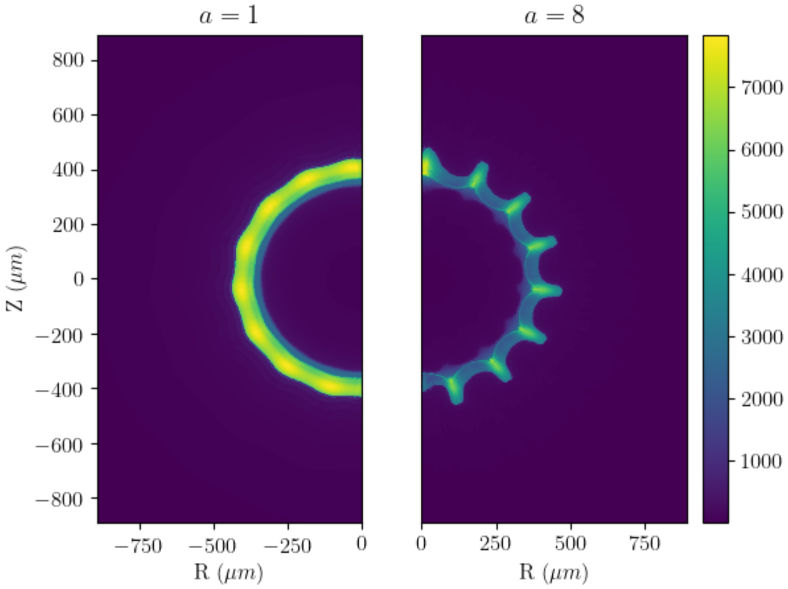

Figure 3.14: The density profiles of imploding capsules with an $l = 5$ perturbation of varying amplitude applied to the laser power. A perturbation amplitude of $a_p = 1\%$ is shown on the left, and a perturbation of $a_p = 8\%$ is shown on the right.

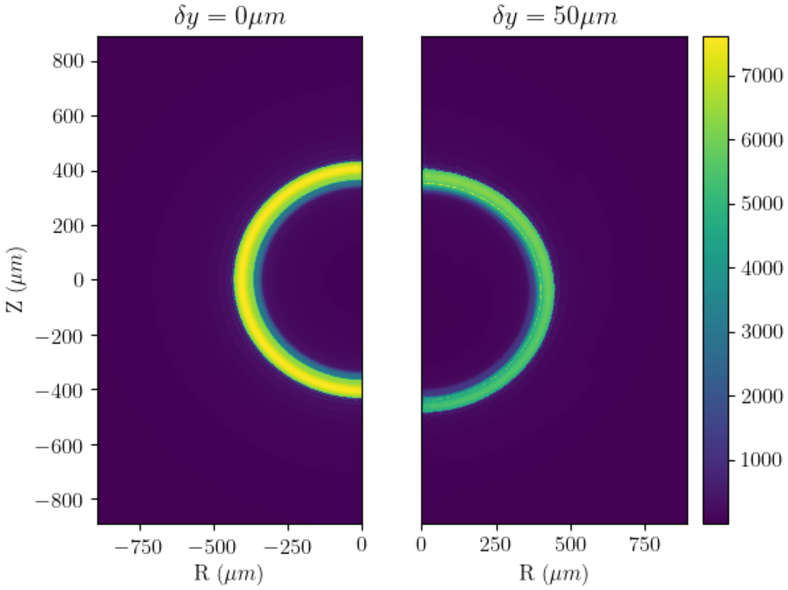

Figure 3.15: The density profiles of imploding capsules with varying applied laser offset in the y-direction. The plot on the left shows the resulting density profile with no offset, and the plot on the right shows the result of an applied offset of $\delta y = 50\mu m$.

3.5 Chapter Summary

We have successfully implemented a number of new features in the source code of *Odin*, which make it more adapted to ICF simulations and improves its predictive and interpretive capabilities. The refractive ray-tracing scheme, combined with face-normal interpolation, and path tracking routines allows for a more accurate representation of single ray trajectories. The scheme does not include beam features such as diffraction, intensity, and polarisation effects. Wedge boundary conditions allow for less computationally expensive, pseudo 1D uniform implosions to be conducted that are able to produce identical results to the 2D equivalent. They can also be used to simulate a highly resolved, section of a capsule, allowing investigation of high-mode perturbations, as are typical of speckles (as discussed in section 1.6.3. Implementation of laser non-uniformities such as laser power perturbations and target offset allows for the impact of such effects on implosion performance to be studied. It also provides a method for testing the robustness of the 2D RZ Lagrangian scheme of *Odin*.

Chapter 4

Implosion asymmetry

This chapter presents the results of a simulation study into the effects of various sources of asymmetry on implosion performance, using the 2D *Odin* radiation-hydrodynamics ALE code. The chapter begins by discussing similar studies that have been conducted using other simulation codes, and their findings. Previous studies of implosion asymmetry have focused on OMEGA experiments or simulations of corresponding setup, this research differs in that it simulates asymmetry for ignition-scale experiments with a larger target capsule and higher laser energies. A description of the various simulations conducted is given, before presenting their results.

4.1 Motivation and Literature review

Implosion symmetry is a crucial criterion for achieving ignition in ICF experiments. As discussed in section 1.6.1, there are two branches of asymmetry: macroscopic and microscopic. These asymmetries are responsible for the deviations we see in experimental results from idealistic 1D simulations. One of the most frequently used indicators of implosion performance is yield-over-clean (YOC); this is the ratio of the experimental neutron yield to its value found from 1D simulations. Macroscopic asymmetries occur at low modes ($l \leq 20$) and arise from large-scale effects from the laser system and target, such as laser-target offset, beam power misbalance, and target roughness. Target roughness can also contribute to high modes, $l \geq 20$. Microscopic asymmetries occur at larger wavenumbers, and mostly occur from in-beam non-uniformities such as speckle patterns within the beams.

Non-uniform laser intensity distributions and their impact on implosion symmetry have been studied since the 1980's with key insights being made by Emery *et al.* [Emery et al., 1991]. Emery *et al.* showed that laser non-uniformities with scale lengths greater than the distance from the ablation surface to the critical surface, have a severe impact on the drive pressure symmetry and pellet gain. More recent studies running simulations with the 3D hydrodynamics code ASTER, have shown that the on-target intensity for direct-drive OMEGA experments needs to be balanced to a few percent root-mean-squared to achieve the desired convergence needed for ignition [Goncharov et al., 2016].

4.1.1 Hu *et al.* Study

One of the most relevant studies, and the inspiration for the series of simulations we conducted came from Hu *et al.* [Hu et al., 2010]. Their paper describes the results of a series of simulations using the 2D DRACO radiation-hydrodynamics code [Radha et al., 2005]. Similar to *Odin*, DRACO is a 2D cylindrical coordinate, Lagrangian code that uses 3D ray tracing with inverse Bremßtrahlung energy deposition and *SESAME* equation-of-state tables for the materials. Radiation transport in DRACO is handled using its multigroup diffusion model, in which opacity and emissivity tables are used. The parameter of interest in their analysis was YOC. Various laser and target perturbations were investigated including:

- Laser nonuniformities
- Target offset
- Ice roughness
- Combined target offset and ice roughness
- Laser imprinting

From their simulations of the capsule design of fig. 4.1, Hu *et al.* quantified the impact of these sources of nonuniformity on YOC. Power imbalance ($l < 10$), target offset ($\delta y > 20\mu m$), and laser imprint ($l = 20 - 150$) were found to decrease the YOC by $\sim 74\%$, $\sim 30\%$, and $\sim 50\%$, respectively. These were the most harmful factors to YOC according to their investigation. A figure showing the effect of varying offset on YOC is shown later on in this chapter, as fig. 4.11. There was consideration given to replicating the simulations conducted by Hu *et al.*, however there was insufficient detail given in the publication to fully replicate them. Despite this, it was possible to obtain similar findings using the comparable simulation setup described in the following section.

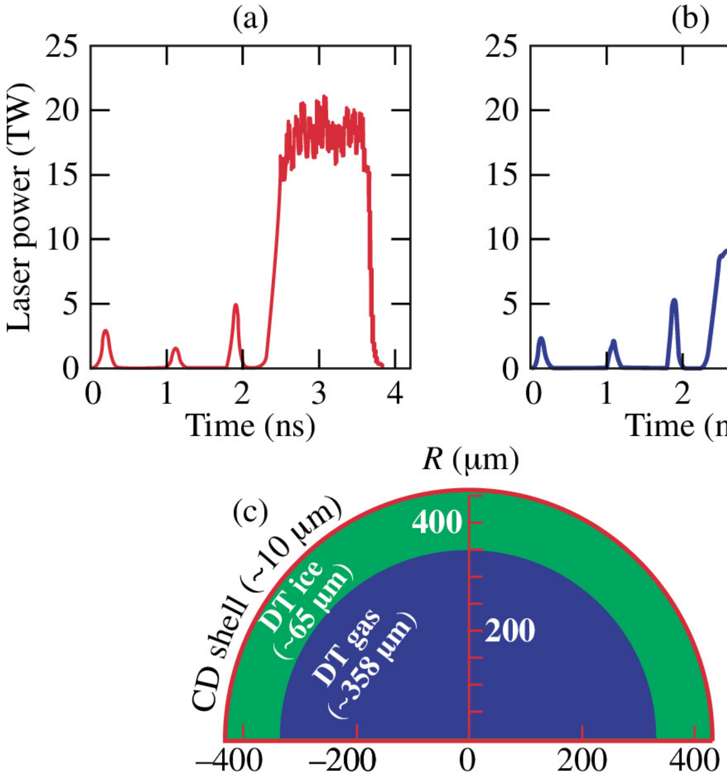

Figure 4.1: (a) The triple-picket plus square main pulse and (b) the triple-picket plus step main pulse used for cryogenic DT implosions on the OMEGA Laser Facility. (c) A schematic diagram of a cryogenic DT target. Reproduced with permission from [Hu et al., 2010].

4.1.2 Craxton *et al.* Simulation Setup

The research in this chapter was conducted using the Odin radiation hydrodynamics ALE code. All simulations were conducted used a 2D RZ grid, with the capsule and triple picket laser profile first described by Goncharov et al. [Goncharov et al., 2010] and revisited for a 1D simulation study by Craxton *et al.* in the direct-drive review [Craxton et al., 2015]. The target design and laser power profile used for these simulations are shown in fig. 4.2. Triple picket designs are utilised to maintain shock heating at reasonable levels so as not to cause adiabat degradation, and to ensure that target preheat is maintained at an acceptable level, as discussed later in Chapter 5. The Craxton *et al.* capsule consists of a 197 μm shell with 37 μm of CH ablator material, and 160 μm of DT ice. Contained within the shell is 1503 μm of DT gas. Note that the laser operates with 3ω Nd:YAG at 351 nm and has an applied resonance absorption fraction of 0.15 in *Odin*. A uniform illumination configuration was chosen for the beams, and all ray-tracing features such as refraction and reflection were used for these simulations. Our initial simulation gave an areal density value of 320mg/cm^2 at peak compression which is slightly higher than the published result of 290mg/cm^2 [Radha et al., 2011]. Given that we were using a simplistic beam geometry for the rays, we decided to conduct our investigation using the 2D ray-tracing scheme, since we had seen, for this simplisitc configuration, that both 2D and 3D schemes were in close agreement with each other (as demonstrated in Figure 3.9). The reduction in computational cost would allow us to conduct more simulations and to further investigate nonuniformities.

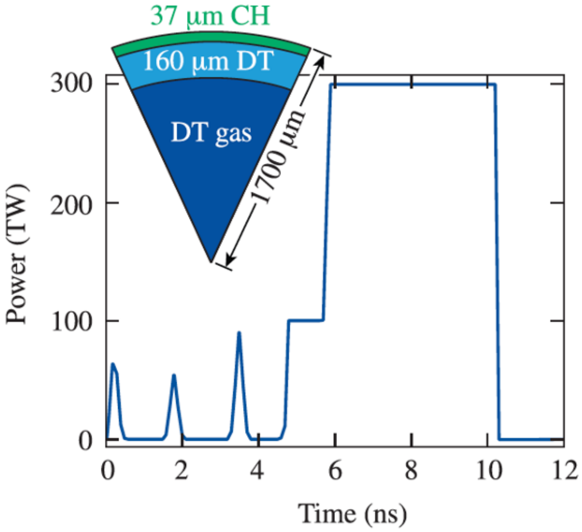

Figure 4.2: Pulse shape and target dimensions for a 1.5-MJ triple-picket design for the NIF that is predicted to achieve a 1D-gain of 48. Reproduced with permission from [Craxton et al., 2015].

4.2 Capsule Setup for the Craxton target

As mentioned above, the simulation used the target and laser from Craxton *et al.*. To resolve the domain effectively, 302 radial cells were used that were mass-matched (section 2.3.8) and separated into 4 different regions: a region of DT gas (ρ=0.6 mg/cm^3), 2 regions of DT ice (ρ=250 mg/cm^3) to optimise the cell mass profile, and 1 region for CH ablator (ρ=1050 mg/cm^3). Two regions of DT ice were needed to gradually change the cell masses between the low density gas region and the dense CH ablator region. The DT ice layer is cryogenic and the target has an initial temperature of 17K. Convergence tests were performed to find the required radial

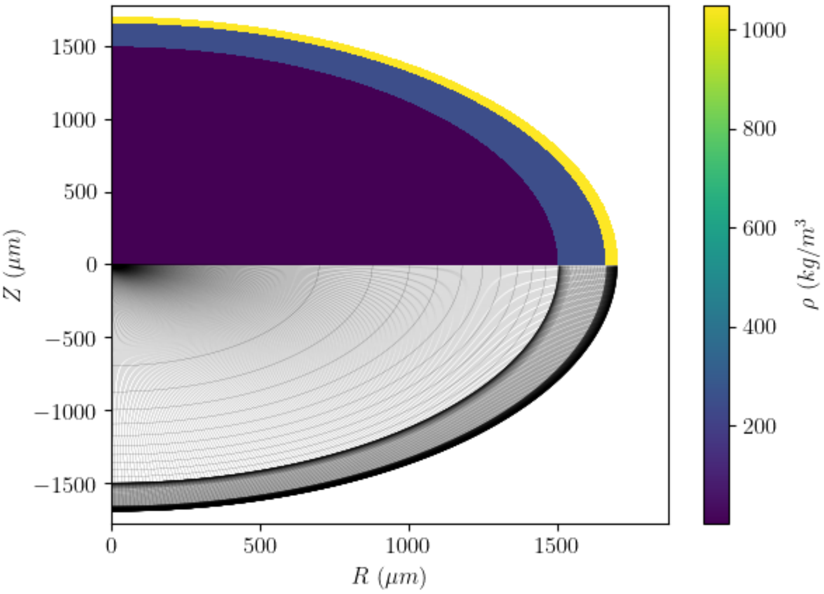

Figure 4.3: The initial grid domain utilised for the *Odin* simulations for investigating implosion asymmetry. Note that the density of the capsule is shown as a colour-map, with its scale shown on the right hand side. The yellow, purple, and blue regions indicate the CH ablator, DT ice, and DT gas regions respectively. For the lower half of the capsule, the grid lines have been plotted to show the reader the resolution of the domain, $N_r = 302$ and $N_\theta = 200$.

resolution for these simulations. These convergence tests were simplified versions of the Craxton *et al.* simulation setup with limited thermal conduction and no radiation transport. The results of these tests are shown in section 4.2 and show that results begin to converge at $N_r = 200$, however to account for the impact of limited physics, we used a value of 302 radial cells for our simulations. In addition, a full hemispherical domain with 200 poloidal cells was used and a minimum of 20 rays per cell (the offset simulations required larger ray numbers up to 100 rays per cell). The rays were uniformly distributed around the hemisphere, and initially interacted with the target radially. As the simulations evolved then perturbations in the density of the target meant that refraction of the rays became more prominent. Figure 4.3 shows the initial setup of a default simulation. Any deviations from this setup are discussed in the relevant subsections.

For the symmetric implosion case, the results are shown in Figure 4.4. Note that this simulation reaches peak implosion at 10.3ns, which is 1ns earlier than the published results shown in Craxton *et al.*. These differences occur because of

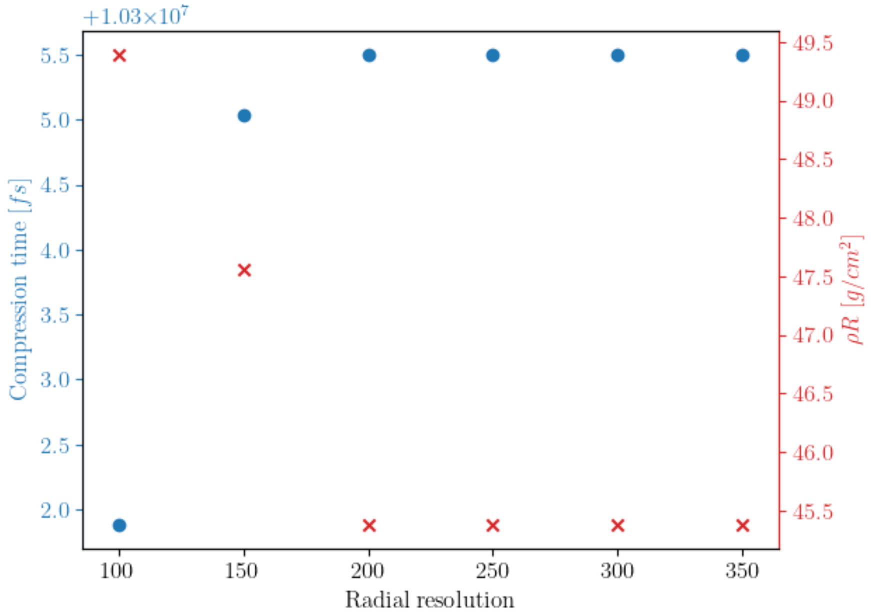

Figure 4.4: Convergence testing. The measured peak compression time (blue) and corresponding areal density , ρR, (red) values for simulations with limited physics for a range of radial cell resolutions between $N_r = 100 - 350$. These results show that results begin to converge after $N_r = 200$. Note that the y-axis on the left hand side has units of fs in order to show the minute difference in peak compression time for these simulations.

differences between *Odin* and *DRACO* such as ray-tracing scheme, beam geometries, EoS tables, thermal conduction, to name a few. DRACO uses a ray-based model to replicate the reduction of hydrodynamic coupling efficiency due to cross-beam energy transfer (CBET). In *Odin* this is done by applying a 10% reduction to the laser power during the main pulse.

4.3 Hotspot Analysis

In their investigation of the impact of laser non-uniformities on implosion performance, Hu *et al.* used the yield-over-clean (YOC). This metric relies upon the simulation code having a burn package, which *Odin* does not currently have. As an alternative metric to represent yield, we decided to investigate the hotspot areal density, $(\rho R)_h$. This is calculated by considering the cell-volume-weighted average density of the

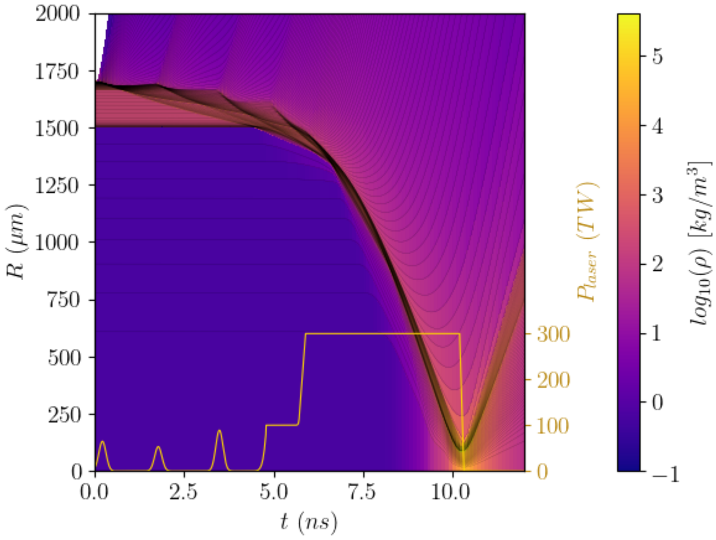

Figure 4.5: Results from a 2D *Odin* symmetric implosion showing the radial density of the target plotted as a function of time throughout the implosion, using the initial conditions of [Craxton et al., 2015]. Note that the laser power profile has been plotted on the lower part of the graph, to show the hydrodynamic reaction at different stages.

hotspot, for each poloidal, j, and radial, i, index as described by:

$$(\rho R)_h = \sum_{j}^{N_\theta} \left(\sum_{i}^{N_r(j)} V_{i,j} \rho_{i,j} \right) R_j \bigg/ V_j \tag{4.1}$$

where N_{theta} is the total number of poloidal cells, $N_r(j)$ is the total number of radial cells that contain the hotspot for poloidal index j, $V_{i,j}$ and $\rho_{i,j}$ are the volume and density of the cell with indices i and j, V_j and R_j are the total volume and the radial extent of the hotspot for poloidal component j, respectively.

In addition, the neutron yield, N, in cryogenic DT implosions, is known to scale with the hotspot parameters as [Hu et al., 2010]:

$$N \propto V_h \times t_b \times \rho^2 \times T_i^4, \tag{4.2}$$

where V is the hotspot volume, t_b is the burn time, ρ is the density of the hotspot, and T_i is the hotspot ion temperature. Therefore, we will also consider the impact of applied nonuniformities on these parameters.

The hotspot of an imploding capsule is characterised by a sharp drop in the

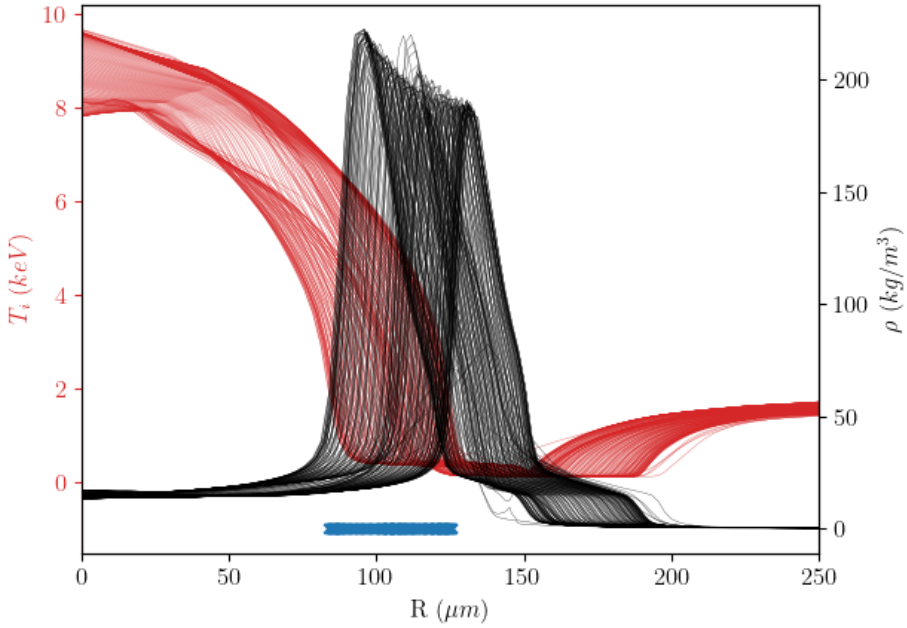

Figure 4.6: The density (black) and electron temperature (red) profiles of a hotspot at peak compression ($t = 10.3ns$), with an applied $l = 1$ laser power perturbation of $a = 3\%$. Blue markers have been added to show the radial extent of the hotspot according to its definition.

ion temperature profile, followed by an immediate increase in density. In our analysis, we defined the extent of the hotspot as the point at which the ion temperature has fallen and has minimum gradient, $R_h = R(dT/dR)_{\mathrm{min}}$. An image of the ion temperature T_i and density ρ profiles, for a perturbed hotspot ($l = 1, a_p = 3\%$) at peak compression, is shown in fig. 4.6. Note that the radial extent of the hotspot for each poloidal angle of the grid domain is shown by the blue markers, which are scattered between 80-130μm.

By tracing the radial extent of the hotspot for all poloidal angles, we can generate an outline to visualise the impact of the non-uniformity on the implosion, as plotted in Figure 4.5. A 2D outline of this hotspot is shown in Figure 4.6. Additionally, for each poloidal angle around the hotspot, we evaluate the volume-weighted density and calculate the areal density $(\rho R)_h$ as described by eq. (4.1). We also consider the volume-weighted parameters included in eq. (4.2), as they are related to the burn of DT and provide good metrics of implosion performance. A histogram of $(\rho R)_h$ and T_h and measured values around the capsule is shown in fig. 4.8.

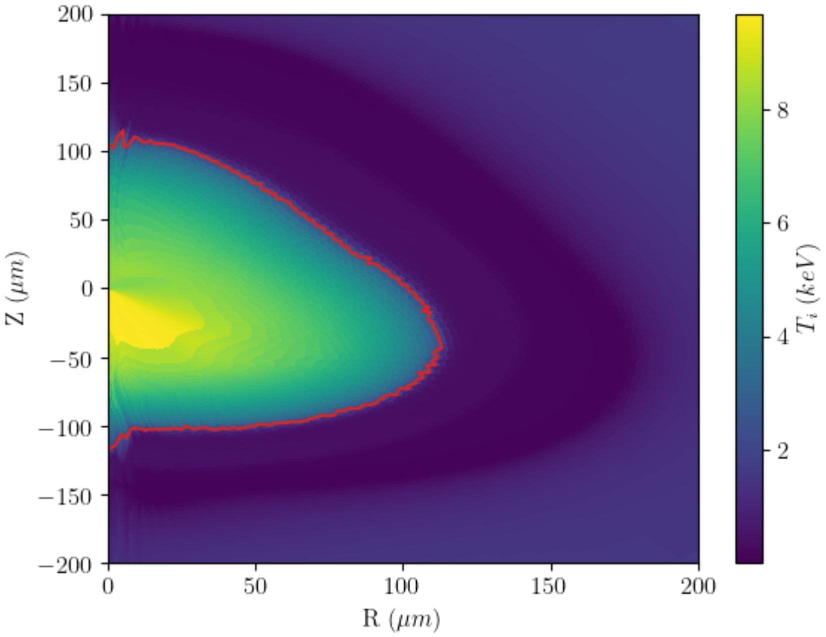

Figure 4.7: A colormap of the ion temperature profile of a perturbed imploding target at peak compression, $t = 10.3ns$, with a $l = 1$, $a_p = 3\%$ power perturbation applied. The outline of the hotspot is shown in red.

4.4 Low-mode Power Perturbations

4.4.1 Theory

As discussed in section 3.4, a routine for adding laser non-uniformities has been implemented into *Odin*. The application of a harmonic perturbation to the laser power profile has the effect of recreating the consequences of beam power-misbalance, laser mis-timing, and surface roughness. When the density profile of a laser-driven target is perturbed, the imploding shock breaks out unevenly across the target, and this causes certain regions to be *overdriven* and reach higher densities compared with the rest of the target.

In their investigation of low-mode laser nonuniformities, Hu *et al.* applied their perturbations to both the laser pickets and main pulse. They found that applying higher amplitude perturbations during the laser pickets (as shown in fig. 4.1) was more detrimental to the YOC measurement than applying the same perturbation during the main pulse of the laser. As discussed in their paper, the reason that perturbing the picket power is more detrimental to YOC is because the nonuniformity

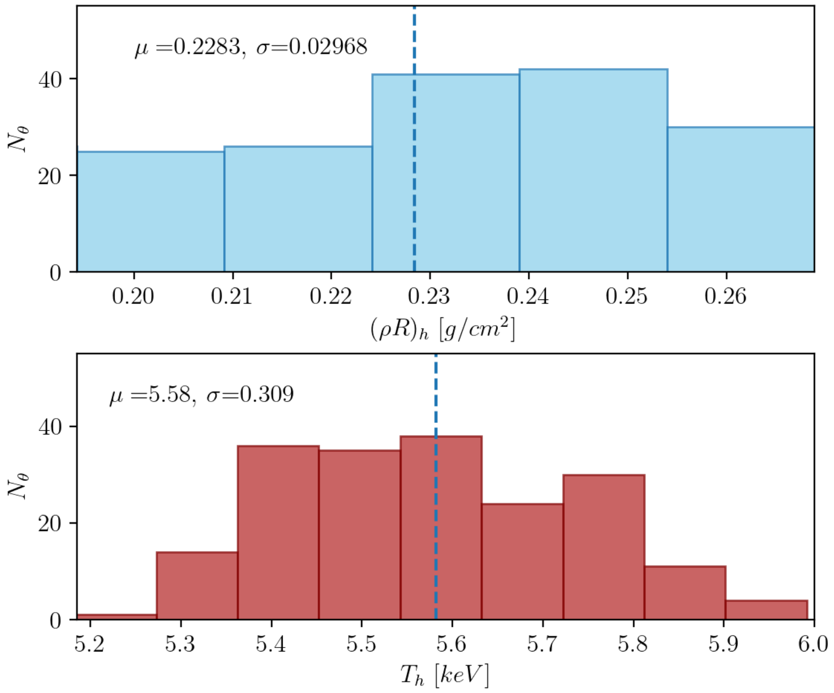

Figure 4.8: Histograms of the hotspot showing the number of poloidal cells, N_θ, with (above) areal density, $(\rho R)_h$, and (below) ion temperature, T_h, values within a specified range. The mean values, μ, and standard deviations, σ, of the distributions are plotted in dotted lines and their values shown on the corresponding figures.

can be more efficiently seeded during this earlier stage of the implosion, as is the case with speckles. This is likely because the distance between the ablation front and critical surface is shorter during the picket stage, compared with the distance during the main pulse. Therefore, according to eq. (1.54), thermal smoothing is less effective during the picket phase. For our investigations, we studied perturbations that occur during the main pulse of the laser. Attempts to simulate laser nonuniformities applied during the picket stage of the laser drive were unsuccessful as the thermal conduction routine failed. This is an unresolved issue in *Odin* that is currently being rectified.

4.4.2 Simulation Details

Using the standard grid domain, defined in Figure 4.3, these simulations applied a l=1 harmonic perturbation to the laser power profile ranging from a_p = 0% to 5%. This range was chosen based on experimental data of the $l = 1$ non-uniformities amplitude [Knauer et al., 2000]. Note that for simulations with higher amplitude perturbations ($a \geq 3\%$), it was necessary to dynamically remap the grid several times during the ramp up of intensity during the main pulse. For the $a_p = 4\%$ and $a_p = 5\%$ simulations, it was necessary to run in fully Eulerian mode from $t = 10.1$ns and $t = 9.5$ns, respectively, to reach peak compression at $t = 10.3$ns.

4.4.3 Results

In our simulations, the perturbations were applied such that the highest laser intensities were experienced in the upper quadrant of the capsule at 45°, and the lowest intensities at -45°. The impact of these perturbations on the hotspot profile is shown below in fig. 4.9. In this figure, we see that increasing amplitude more heavily distorts the target, and reduces the symmetry of the hotspot.

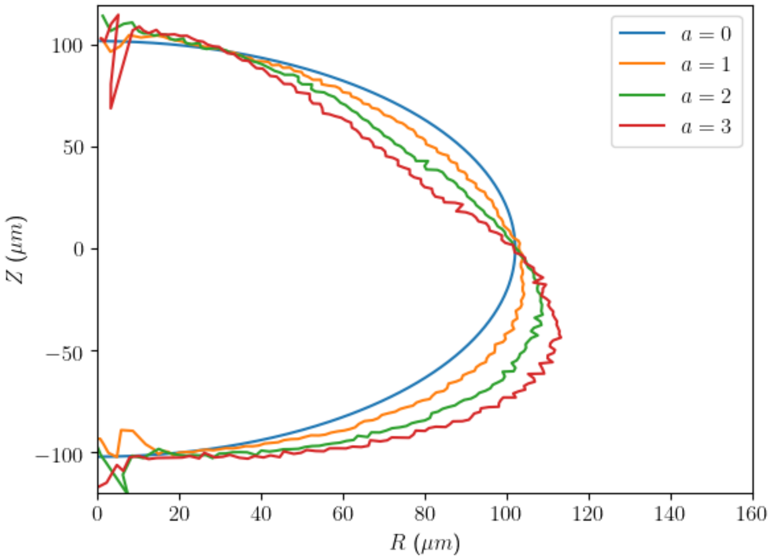

Figure 4.9: The outline of the hotspot at peak compression for different amplitude perturbations from $a = 0 - 3\%$ applied to the Craxton *et al.* capsule.

Our simulations show that the applied perturbations reduce the areal density of the target at peak compression, as seen in fig. 4.10. This figure shows the hotspot areal density as a function of the $l = 1$ perturbation amplitude. Note that the error bars show the extent of areal density measurements across the target, as discussed in section 4.3. The symmetric implosion has an areal density at peak compression of $(\rho R)_0 = 0.320$g/cm^2, which decreases with increasing perturbation amplitude. We see a *shoulder*, where there is little change in areal density measurements up to $a_p = 1\%$. For a perturbation <1%, there is little change in areal density measurement. Beyond this point, perturbations have more impact on areal density, with reductions in $(\rho R)_h$ of 20% or greater. In addition, the range of areal density values measured across the target increases with amplitude. This is to be expected since, as the amplitude of the perturbation increases, there is a higher disparity in the compression of regions of the target. A 5% perturbation results in a ~37% reduction in areal density. Beyond this amplitude, simulations had to be ran in fully Eulerian mode, at earlier times, $t < 9.5$ns, meaning that there was insufficient resolution at the centre of the domain to perform the hotspot analysis and obtain measurements of areal density and other implosion metrics.

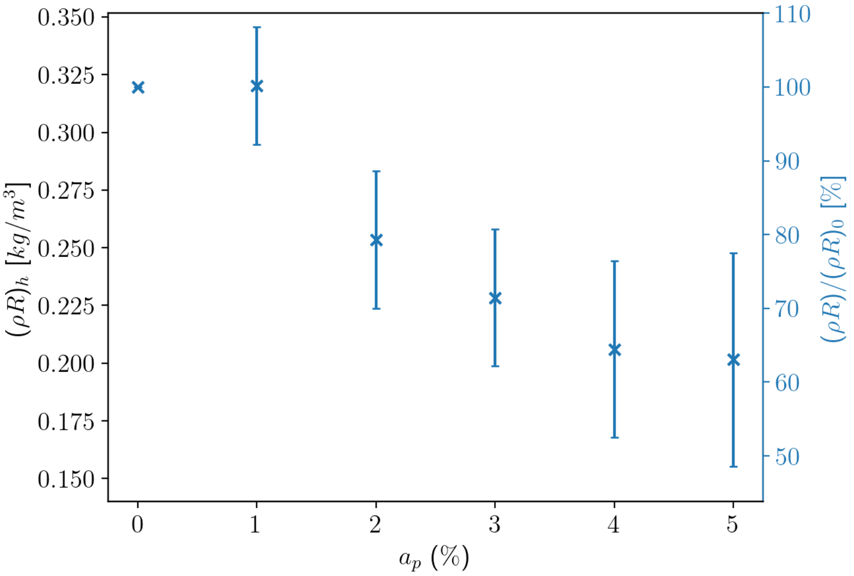

Figure 4.10: Peak areal density, $(\rho R)_h$, plotted as a function of perturbation amplitude. Each cross shows the cell-volume-averaged areal density measurement and the bars show the range of values across the target.

An overview of the $l = 1$ harmonic perturbation results, for a range of amplitudes, is shown in the table below. In this table, we include a metric, Y_{eff}, based on eq. (4.2) as a proxy for the effective yield of the implosion which is described by:

$$Y_{eff} = V_h \rho_h^2 T_{i,h}^4 \tag{4.3}$$

where V_h is the hotspot volume, ρ_h is the average hotspot density, and $T_{i,h}$ is the average ion temperature of the hotspot. In our analysis, all hotspot parameters included in the above equation were cell-volume-weighted. Note that we have not included burn time, t_b, as we have no means of measuring this metric. In the tables presented in this chapter, and later in Chapter 5, we consider the normalised value of the effective yield with respect to the symmetric result.

As amplitude increases, we see that the effective yield, Y_{eff}, of the target decreases, as generally both the density and temperature of the hotspot decrease. The effective yield in the symmetric case has a value of 6.99×10^{11}kg^2 eV^{-4} m^{-3}. To contextualise this parameter, the values presented in the tables of this chapter are normalised. This reinforces the previous results of fig. 4.10 showing that implosion performance decreases with perturbation amplitude. The volume of the hotspot varies inconsistently with increasing amplitude, which is likely due to the distortion of the computational grid from the applied perturbation. At an amplitude of $a_p = 5\%$ the hotspot has failed to form, and although the hotspot has a larger volume of 1.36×10^{-12}m^3, the densities and temperature of the hotspot are insufficient for fusion reactions to occur as is reflected in its Y_{eff} value.

Laser power misbalance				
Amplitude (%)	V_h $[m^3]$	ρ_h $[kg/m^3]$	$T_{i,h}$ $[keV]$	Y_{eff} (%)
0.0	7.09×10^{-13}	3.13×10^{4}	5.63	100
1.0	7.26×10^{-13}	3.13×10^{4}	5.19	73.8
2.0	7.57×10^{-13}	2.43×10^{4}	5.68	66.5
3.0	7.79×10^{-13}	2.16×10^{4}	5.58	50.7
4.0	3.96×10^{-13}	2.46×10^{4}	6.03	45.3
5.0	1.36×10^{-12}	5.49×10^{3}	1.57	35.7

Table 4.1: The results of a parameter scan in power misbalance ($l = 1$ perturbation), showing the effect of increasing perturbation amplitude on a series of important implosion metrics including hotspot volume, V_h, density, ρ_h, ion temperature, $T_{i,h}$ and effective yield, Y_{eff}.

4.4.4 Discussion

Our simulations show that low mode perturbations can be damaging to implosion performance beyond 1%, and are catastrophic from 5%. Measurements of hotspot areal density from the *Odin* simulations revealed a decline with perturbation amplitude over the range considered, and reached a minimum value of 0.2015g/cm^2; 63% of the symmetric implosion value. We also predicted the effective yield of the target from the parameters needed for its calculation. Increasing perturbation amplitude was found to decrease the effective yield of the target with the most significant drop occurring between $a_p = 1\%$ and 2%.

For comparison, the findings of Hu *et al.* using a smaller OMEGA scale capsule design, suggested that there was less impact of low mode perturbations on target implosion. For a 3% beam imbalance during the picket stage and a 10% imbalance during the main pulse, they found a decrease of only 9.7% in YOC. This discrepancy is likely due to the beam geometry utilised in their simulations. Hu *et al.* applied the experimental configuration of the beams of OMEGA, in which the beam width is similar to the initial size of the ICF pellet. With this configuration, at least half of the outer surface of the target is illuminated by each beam, and macroscopic nonuniformities are smoothed by these overlapping beam profiles. This was not the case for the *Odin* simulations described above. The beams illuminate the pellet radially and perturbations are applied directly onto the surface of the target. Without the inclusion of overlapping beams, these results show the worst-case scenario of the $l = 1$ perturbation in laser power.

4.5 Laser-Target Offset

4.5.1 Context

Laser-target offset is a common occurrence in inertial fusion experiments (as described in section 1.6.1) and is a source of degraded implosion. Offset works to preferentially heat part of the target, which imposes an asymmetric compression of the ICF pellet. Experimentally, the OMEGA laser facility are able to maintain offset to values of $\sim 9\mu$m [Forties and Marshall, 2005]. The effect of laser offset on yield was investigated by Hu *et al.*. They studied its impact for two laser profiles: one with a square pulse, and another with a step pulse, as shown in fig. 4.1. Combined with laser offset, each laser profile had a differing effect on the implosion performance, as shown in fig. 4.11.

In Hu *et al.*'s simulation results, the step pulse laser profile is more sensitive to laser offset than the square main pulse, and adds a twofold reduction in YOC measurements that have also been observed experimentally. Our simulations used the setup described by Craxton *et al.* with a triple picket and stepped laser pulse, as seen in the blue line of fig. 4.1. Therefore, it is possible that our setup is also more sensitive to laser offset. The stepped main pulse in the laser power profile is needed to avoid an increase in the adiabat, α, of the inner shell surface due to pressure amplification [Goncharov et al., 2010].

4.5.2 Simulation Details

This series of simulations used the same standard setup as described in section 4.2, and performed a parameter scan of laser offsets varying between 5-30μm. For simulations

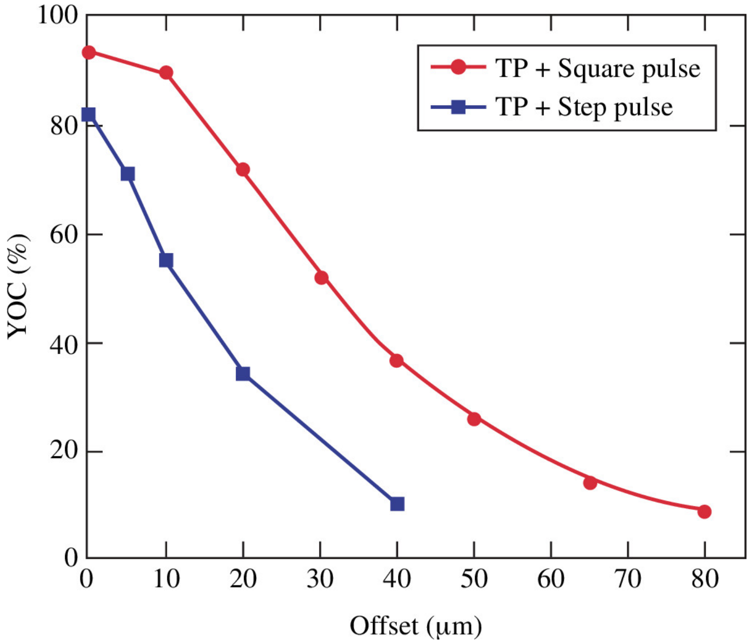

Figure 4.11: The YOC is plotted as a function of the target offset for the two types of pulses shown in fig. 4.1. Reproduced with permission from [Hu et al., 2010]. Note that TP is an acronym for Triple Picket.

with $\delta y \geq 15\mu m$, dynamic remapping in Lagrangian mode was prominent at 6.0ns, when the laser power increases from the step to the main pulse. Note that for laser offsets of $\delta y \geq 20\ \mu m$, it was necessary to remap the simulation and run with fully Eulerian hydrodynamics from $t \sim 9.0$ns.

4.5.3 Results

Our simulations showed that increasing the laser offset in the Z direction of the capsule resulted in more energy being deposited above the equator of the capsule. This preferential heating of the upper half of the capsule led to a shifted and distorted hotspot. Measurements of areal density at peak compression ($t = 10.3$ns) for a range of laser offsets are plotted below in fig. 4.12. Note that these asymmetric implosions are likely to reach peak compression at slightly different times to the idealised symmetric case, and that these measurements of areal density (and other implosion parameters) have a margin of errors associated with this timing difference.

Generally, we see a decrease in hotspot areal density for increasing laser offset. Implosion performance is affected by minor laser offsets, and even for $\delta y = 5\mu m$, there is a 5% decrease in areal density. Between small values of laser offset, $\delta y < 15\mu m$, we see changes in areal density, suggesting a tolerance level for this particular setup.

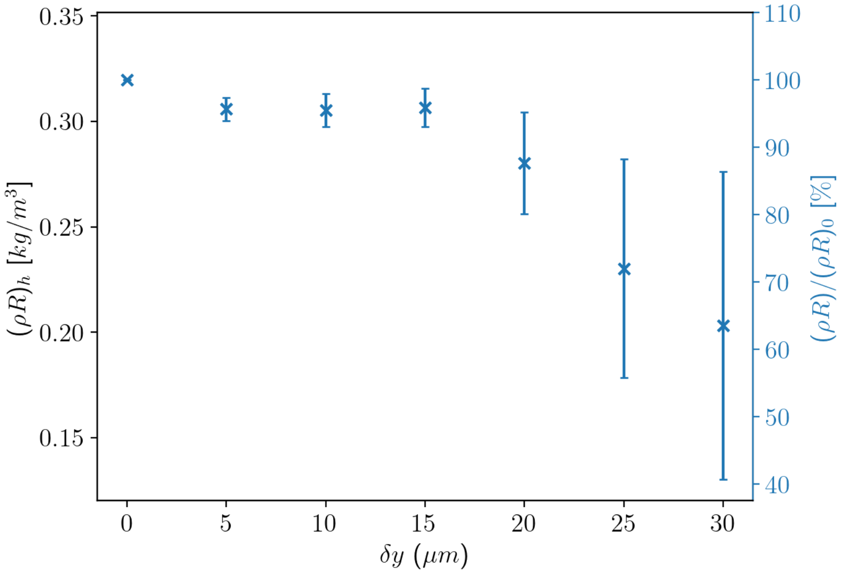

Figure 4.12: Volume-averaged hotspot areal density, $(\rho R)_h$, plotted as a function of laser offset. Each cross shows the cell-volume-averaged areal density measurement and the bars show the range of values across the target.

Beyond this point, laser offset is detrimental to the implosion performance of the capsule and we see a sharp decrease in areal density. At $\delta y = 30\mu$m, the areal density has decreased by 36% from the uniform result with 30keV hot electrons. From $\delta y = 15\mu m$, we see an increase in the range of measured areal densities, suggesting that the hotspot is becoming more distorted as offset increases.

Table 4.2 presents the changing values of hotspot parameters relevant to yield. As offset increases, we see a decrease in the effective yield of the simulation, which is linked to the decrease in hotspot temperature and density. There is no clear correlation between hotspot volume and increased offset. For small values of offset, the hotspot volume decreases, but beyond $\delta y = 20\mu m$, the volume increases but has a lower density.

4.5.4 Discussion

Our results set a threshold for the laser offset of an experiment at $\delta y < 30$ μm. For simulations with this amount of offset, the implosion is able to obtain a hotspot areal density of $(\rho R)_h \simeq 0.203$ g/cm^2. With an areal density of this value, the burn fraction is only 3.3% using eq. (1.33).

Note that our simulations indicate a less significant impact due to laser-target

Laser Offset				
Offset, δy (μm)	V_h [m^3]	ρ_h [kg/m^3]	$T_{i,h}$ [keV]	Y_{eff} (%)
0	7.09×10^{-13}	3.13×10^4	5.63	100
5	6.93×10^{-13}	3.02×10^4	5.30	71.3
10	6.94×10^{-13}	3.02×10^4	5.29	70.8
15	6.94×10^{-13}	3.02×10^4	5.29	70.9
20	7.43×10^{-13}	2.85×10^4	5.32	69.2
25	7.52×10^{-13}	2.28×10^4	5.58	54.1
30	4.70×10^{-13}	2.29×10^4	2.91	25.3

Table 4.2: The results of a parameter scan in laser-target offset, showing the effect of increasing offset on a series of important implosion metrics including hotspot volume, V_h, density, ρ_h, ion temperature, $T_{i,h}$ and effective yield, Y_{eff}.

offset in comparison with the results presented by Hu *et al.*. This is likely down to the differing configurations of both setups. In their study, Hu *et al.* simulated a smaller ICF pellet of radius 433 μm, whereas the Craxton *et al.* setup we chose to model, had a pellet of radius 1700 μm. In addition, their simulations used the experimental beam configuration of OMEGA, not a simplified illumination.

Current inertial fusion facilities can reduce laser offset to below 30 μm, however these experiments are set up over the course of several days and have a low repetition rate. For high-repetition rate experiments, as would be necessary for laser fusion to become a significant energy source, it is likely that suppression of the laser offset to that extent is unfeasible. These results show that larger targets can offer more tolerance to laser offset, but it is still detrimental to implosion performance.

4.6 Chapter Summary

We have presented the results of applied laser nonuniformities to an ignition-scale direct-drive experiment. By investigating the areal density and the effective yield metric, Y_{eff}, as described by eq. (4.3), we quantified the impact of the $l = 1$ mode laser power perturbation and laser offset on implosion performance.

Our simulations show that the $l = 1$ perturbation above $a_p = 1\%$ can be damaging for implosion performance, and beyond a 5% amplitude, it is difficult for a hotspot to form since the target has become significantly distorted and the temperature and density of the core are insufficient for fusion reactions to occur. By plotting our measurements of areal density as a function of applied perturbation amplitude, as shown in fig. 3.14, we found an overall negative correlation between both parameters, although there the profile is flat at low amplitudes ($a_p < 1\%$). In addition, the effective yield, Y_{eff}, showed a decrease as higher amplitude perturbations were applied. It is likely that these nonuniformities will have altered the time of peak compression for the simulations, and that the measurements obtained at 10.3ns are not truly indicative of peak compression.

A similar decline in implosion performance was found for increasing values of laser offset. Our results showed some tolerance to small offset ($\delta y < 15\mu m$), but beyond that point the areal density of the hotspot decreased by ~12% and the range of areal densities around the target was also found to increase.

The impact of laser nonuniformities from our simulations is higher than those reported in [Hu et al., 2010]. This difference is the result of differing beam configurations and target sizes. The beam configuration for *Odin* evenly distributed the beams over the outer surface of the target, and illuminate each radial angle, whereas Hu *et al.* used the experimental beam configuration of OMEGA, in which each beam illuminates the entire target. Their results show a higher tolerance to nonuniformities because the overlapping beam geometry tends to smooth out any perturbations that can form. Our results indicate that larger ICF targets could be more sensitive to low-mode perturbations, but further investigation is needed to confirm this. Given more time and the necessary input data, it would have been useful to implement the beam geometry of Hu *et al.* and repeat this study.

An additional avenue of investigation would be to simulate ICF targets with applied DT ice roughness, as was presented in [Hu et al., 2010]. *Odin* does not currently have the functionality to perturb material surfaces, however it would be possible to add fluctuations in the density of a given material as a proxy to the additional mass that ice roughness introduces.

Chapter 5

Implosion asymmetry with Hot-Electrons

In Chapter 4, we presented the results of implosion performance in the presence of laser non-uniformities for ignition-scale ICF experiments. Similar simulations have been conducted for this chapter but with the inclusion of hot-electrons. Hot-electrons arise indirectly as a consequence of laser plasma instabilities as discussed in section 1.6.5, and are detrimental to implosion performance. Few radiation-hydrodynamic codes have the functionality of including hot electrons, and, combined with the various sources of asymmetry, the results of this chapter are novel and quantify the impact of these hot electrons on implosion performance.

5.1 Motivation and Literature Review

Understanding and quantifying the role of hot-electrons, generated by LPIs, on fuel preheat has been a key issue in direct-drive fusion experiments. Hot-electrons are typically characterised as electrons with temperature distributions between 30-80keV [Rosenberg et al., 2018, Campbell et al., 2017]. Strictly speaking, hot-electron distributions are those that remain after subtracting the background plasma distribution (typically of temperature $\sim 3keV$), from the total electron distribution. Simulations of OMEGA direct-drive experiments have shown that only low levels of laser energy conversion to hot-electrons ($\leq$0.1%) can be tolerated before electron preheat degrades the implosion adiabat and impairs implosion performance [Goncharov et al., 2016].

Studies of DT fuel preheat from hot-electrons were conducted using experimental data and 1D LILAC hydrodynamic simulations, by Cristopherson *et al.* [Christopherson et al., 2021]. They found that hot-electrons degraded the performance of laser-driven implosions by preheating the DT fuel and reducing the compressibility of the target. In their study, Christopherson *et al.* measured the increasing value of adiabat due to hot-electrons, and the decrease in areal density, ρR. Their simulations were in agreement with the scaling law found by [Shvarts et al., 2008]:

$$\frac{(\rho R)_{hot}}{(\rho R)_{nohot}} \simeq \left(1 + 1.16\frac{E^{preheat}_{stag}}{IE_{shell}}\right)^{-4/3} \tag{5.1}$$

where $(\rho R)_{hot}$ is the areal density of the hotspot from experiments that include hot-electrons, and $(\rho R)_{nohot}$ is the areal density from 1D LILAC simulations without hot-electrons. $E^{preheat}_{stag}$ is the preheat energy to the stagnated shell and IE_{shell} is the shell internal energy at peak implosion velocity.

Current direct-drive inertial fusion experiments conducted at the 30kJ OMEGA laser facility, which operate at relatively low laser intensities in comparison to NIF, are subject to LPI and the problematic generation of hot-electrons. Ignition-scale direct drive experiments, with higher intensities, are expected to have a longer density scale length and will result in a larger, and possible more energetic population of hot-electrons being generated.

Experiments conducted at the 1.8MJ National Ignition Facility (NIF), using planar targets, have investigated the production of hot-electrons in ignition-scale direct-drive ICF experiments [Rosenberg et al., 2018]. Using laser intensities between (6-16)$\times 10^{14}$W/cm^2, they accessed hot-electron regimes with density scale length ($\sim$ 500-700μm) and temperatures between 3-5 keV. They found that a fraction of laser energy as high as 2.9% was converted to hot-electrons. This is a relatively significant increase in the conversion fraction typically observed at the 30kJ OMEGA laser facility, which sees a maximum of 1% of its laser energy converted to hot-electrons at peak irradiation [Rosenberg et al., 2018]. Measurements of hot-electrons in laser-irradiated plasmas at the OMEGA facility estimate that temperatures between 20-60keV can be expected for direct-drive ICF experiments [Solodov et al., 2016, Rosenberg et al., 2018], and PIC simulations of TPD found similar results [Vu et al., 2012]. Note that SRS is believed to be the more dominant source of hot-electrons for ignition-scale direct drive experiments [Michel et al., 2016].

There is a difference in the temperature of hot-electrons generated by TPD and SRS [Kruer, 2003], and a more accurate representation of LPI in laser-driven ICF would include two populations of hot-electrons with thermal distributions representative of each instability. There is also a difference in the divergence of hot-electrons produced by each instability [Yaakobi et al., 2013]. The divergence of hot-electrons, along with their temperature, determine the amount of fuel preheat.

A larger divergence causes less preheat of the fuel and is less damaging to implosion asymmetry, because fewer electrons reach the shell and core of the pellet. In their experiments, Yaakobi *et al.* found that for wide-divergence hot-electrons, produced as a result of TPD, only $\sim 1/4$ of the electrons reach the cold fuel and preheat it. Unfortunately, this does not provide an angular spread for the cone of hot-electrons generated, since it depends on the density scale length and the position at which the hot-electrons are generated.

5.2 Laser Nonuniformities Simulation Setup

Using the same grid domain as described in the previous chapter (shown in fig. 4.3), and an equal number of rays per cell, we included hot-electrons to our simulations. For each ray, 100 electron macro-particles were generated at each timestep with a specified electron temperature distribution, that is within experimental measurements [Solodov et al., 2016], and are uniformly distributed over a narrow cone angle of $\sim 11.5°$, and with scattering capability enabled, as described by eq. (2.23). This narrow angle was chosen as a reflection of the narrow divergence hot-electrons that are generated as a result of SRS [Rosenberg et al., 2018]. The electrons were not generated until the main pulse of the laser began ($t > 6.0$ns) when intensities exceed the threshold ($I > 10^{14}$W/cm^2) above which LPIs are expected and can produce hot-electrons. The threshold laser intensities associated with each instability are [Rosenberg et al., 2018],

$$I_{14}^{SRS,thr} = \frac{2377}{L_{n,\mu m}^{4/3}}, \tag{5.2}$$

and,

$$I_{14}^{TPD,thr} = \frac{233 T_{e,keV}}{L_{n,\mu m}}. \tag{5.3}$$

Here, I_{14} is the threshold intensity for each instability in units of 10^{14}Wcm^{-2}, $L_{n,\mu m}$ is the density scale length in μm, and $T_{e,keV}$ is the electron temperature in units of keV. We also applied a cutoff temperature of 150keV for the electron distribution as insignificant numbers exist above this. Hot-electrons generated from LPI in laser-driven ICF experiments are not well-constrained by experiments, and the configuration above is an estimate of the properties we expect them to have.

5.3 Symmetric Implosion with Hot-electrons

To quantify the impact of hot-electrons alone on implosion performance, we performed a simulation of a symmetric implosion with no applied nonuniformities. As discussed above, hot-electrons preheat the DT fuel and increase the implosion adiabat, thereby reducing the compressibility of the target. We simulated the symmetric implosion with hot-electrons with thermal distributions ranging between 10-60keV. Since we were considering a symmetric implosion, we reduced the number of angular cells to 100 and only used 5 rays per cell. All simulations were able to run to peak compression using only the Lagrangian scheme. The refractive and reflective capabilities of the ray-tracing scheme were enabled, although they were unnecessary given that there was no perturbations in the poloidal density distribution.

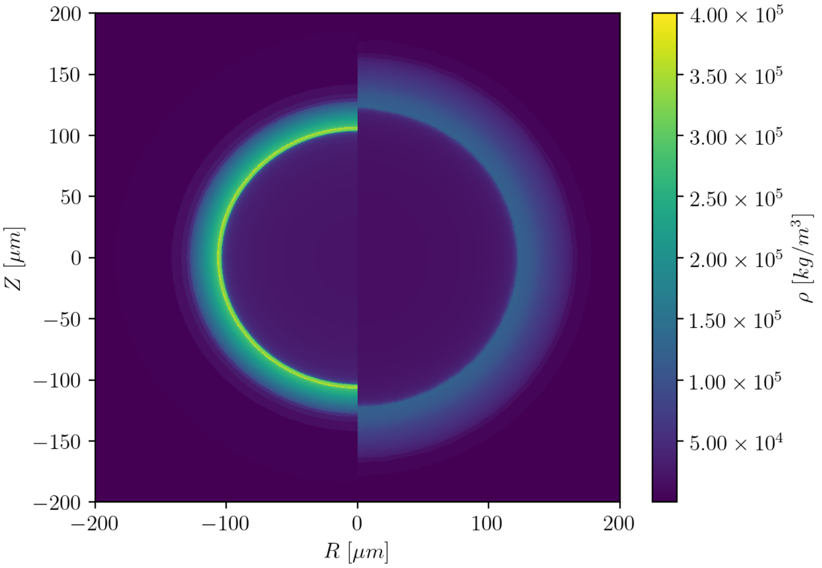

Figure 5.1: A density colour-map of simulation targets at peak compression ($t =$ 10.3ns) by the laser alone (left) and with the addition of 30keV hot-electrons (right). The density scale is shown on the colour-bar on the right of the figure.

Simulations including hot-electrons were found to reduce the density and compression of the hotspot at peak compression. An image showing the comparison in the density profiles of each simulations without hot-electrons and with 30keV electrons is shown in fig. 5.1. Notice that for the simulation with hot-electrons, the density of the imploding shell is reduced. The capsules maintain symmetry during implosion and electron scattering across the target are found to cancel out any preferential heating.

Hot-electrons from 10keV and above were found to preheat the target and reduce the implosion performance. The radial profile of temperature and density for the investigated range of electron temperatures is shown below in fig. 5.2 and fig. 5.3. We can see that increasing electron temperature further reduces the temperature of the core and density of the imploding shell. Note that both the 30keV and 40keV profiles are very similar, and it appears that the impact of hot-electrons beyond these temperatures does not change significantly for symmetric drive.

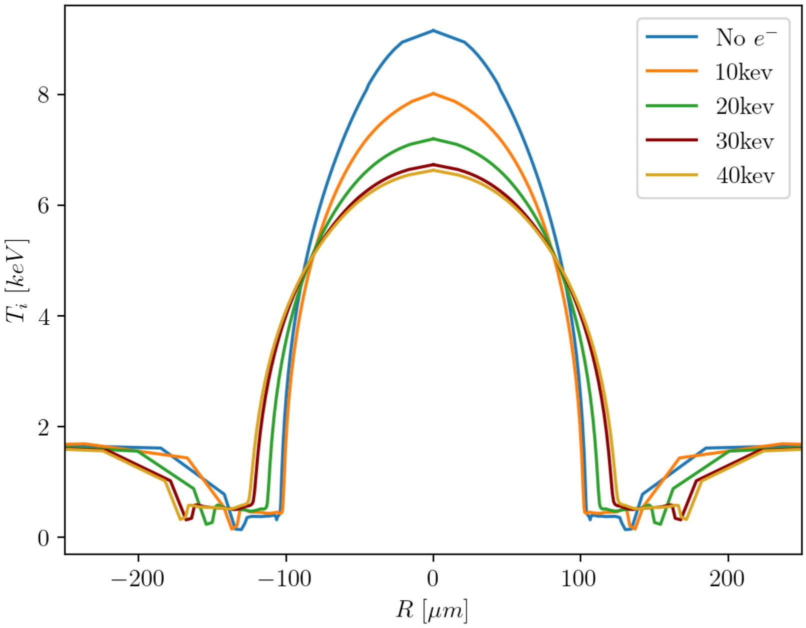

Figure 5.2: The hotspot radial profile of temperature (solid line) for a range of hot-electron temperatures is shown.

Measurements of areal density as a function of electron temperature are presented in fig. 5.4 and a table of other hotspot parameters including effective yield are shown in Table 5.1. At 10keV there appears little degradation to areal density, suggesting that the suprathermal electrons do not have sufficient temperatures to preheat the DT fuel. Beyond this, with electrons of temperature 20keV, the areal density drops by 16%. This result suggest that a threshold temperature at which hot-electrons are damaging to areal density exists between 10-20keV. Areal density continues to decrease until 40keV, at which it has dropped by $\sim$ 30% from its maximum value. Temperatures above this show little difference in areal density or other hotspot parameters. Our results show a slight increase in implosion performance

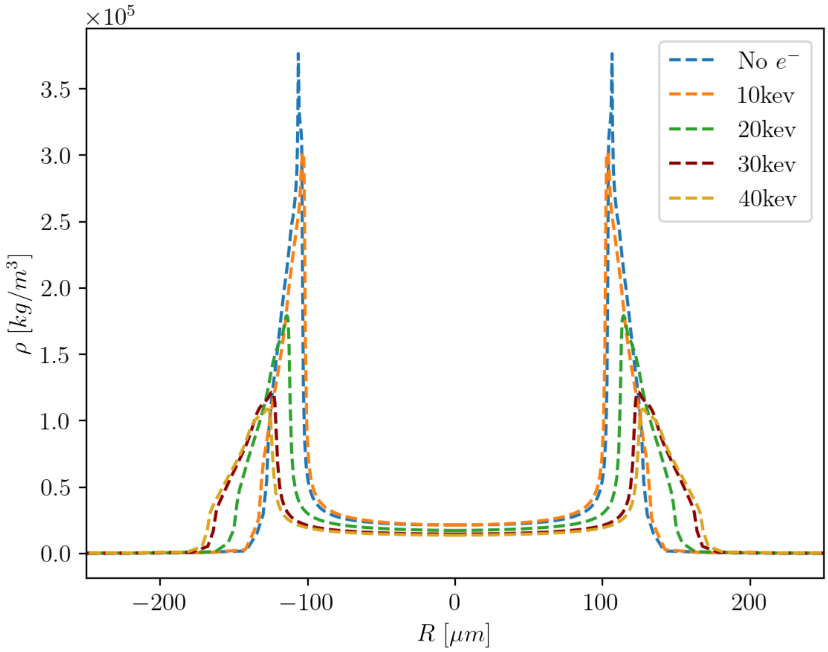

Figure 5.3: The hotspot radial profile of density (dashed line) for a range of hot-electron temperatures is shown.

going from 40keV to 60keV.

Table 5.1 shows that increasing electron temperatures, up to 40keV, reduces the density and ion temperature of the hotspot before they reach an equilibrium range. The hotspot volume increases with hotter electrons. An explanation for this trend could be that the target compression is not as effective, and that the imploding shock is stagnated further away from the core of the target. What these implosions gain in volume is outweighed by the cost of lower densities and temperatures. Since yield scales with T_i^4 and ρ^2, it is more important that these parameters are sustained at high values.

These simulations show to some extent the impact of hot-electron distributions of varying temperature on implosion performance, however further simulations are required to fully quantify their effect. For each distribution temperature, it would be useful to investigate the change in hotspot areal density with changing hot-electron cone angles. In addition, it would be useful to generate two independent distributions of hot-electrons that could represent the populations that arise from SRS and TPD respectively.

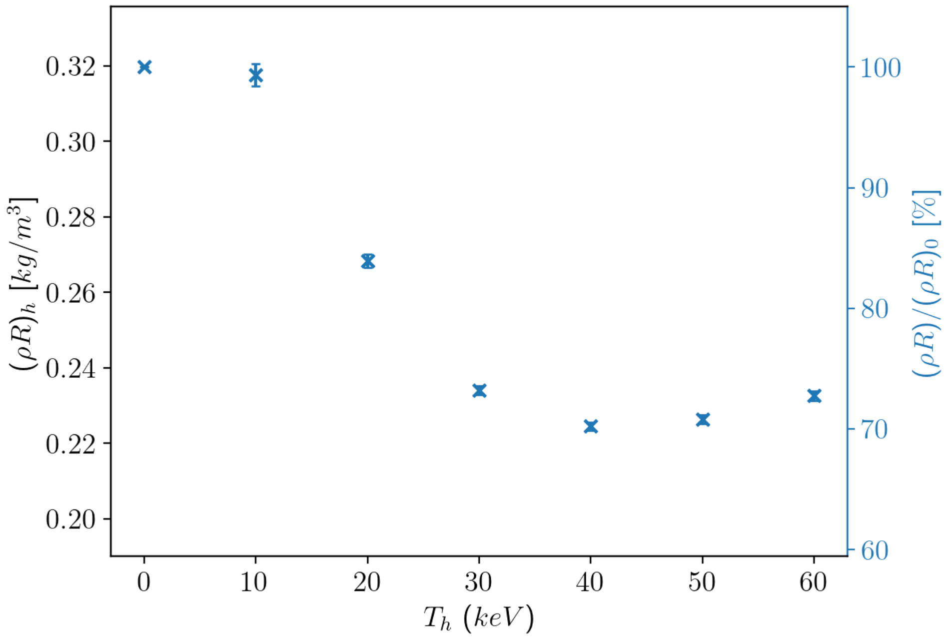

Figure 5.4: Hotspot areal density as a function of hot-electron temperature, T_h. Note that the range of areal density values are so small that they are not visible on this plot.

5.4 Low-mode Power Perturbations

5.4.1 Simulation Details

For this investigation, we conducted a series of simulations with varying amplitudes of the $l = 1$ mode perturbation. A population of hot-electrons, with a 30keV thermal distribution, was generated at the quarter-critical density from $t = 6.0$ns, as the main pulse of the laser begins. As the hot-electrons are generated with an energy proportional to the laser energy, the applied laser power perturbation will also be experienced by the hot-electron distribution across the target. Although dynamic remapping was present near peak-compression, it was not necessary to run any of these simulations in fully Eulerian mode.

5.4.2 Results

Our simulations show that hot-electrons reduce the harmful impact of laser power perturbations on the areal density of an imploding target. Although there is a significant decrease in the areal density compared with simulations that do not

Laser power misbalance				
Temperature (keV)	V_h $[m^3]$	ρ_h $[kg/m^3]$	$T_{i,h}$ $[keV]$	Y_{eff} (%)
0 (no e^-)	7.09×10^{-13}	3.13×10^4	5.63	100
10	6.57×10^{-13}	3.19×10^4	5.32	76.5
20	8.47×10^{-13}	2.48×10^4	4.87	41.8
30	1.04×10^{-12}	2.02×10^4	4.59	26.8
40	1.11×10^{-12}	1.90×10^4	4.52	23.8
50	1.09×10^{-12}	1.92×10^4	4.55	24.7
60	1.05×10^{-12}	2.00×10^4	4.62	27.2

Table 5.1: The results of a parameter scan of hot-electron temperature, showing the effect of increasing temperature on a series of important cell-volume-weighted implosion metrics including hotspot volume, V_h, density, ρ_h, ion temperature, $T_{i,h}$ and effective yield, Y_{eff}.

include hot-electrons, as the amplitude of the perturbation increases there is little change in the average areal density value around the capsule, as shown in fig. 5.5.

Figure 5.4 shows fluctuating values of hotspot areal density, $(\rho R)_h$, with increasing perturbation amplitude, a_p. Overall, the trend of results show no strong correlation with changing amplitude, with areal densities staying within the range of 0.22-0.25g/cm^2. This suggest that the electrons smooth perturbations, and that asymmetries in the hotspot are not as strongly set, relative to when the implosion is driven by lasers alone. As amplitude increases there is an increase in the range of measured values, suggesting that the perturbations are still present, but they are not deteriorating the overall areal density of the hotspot. The range of areal density values around the capsule is similar to those found in section 4.4.3, with a range of ∼10% at $a_p = 1\%$ and increasing to ∼17% at $a_p = 5\%$.

An overview of the hotspot parameters is shown in Table 5.2. The inclusion of hot-electrons in simulations are shown to decrease the implosion performance, but way if compensation, it does offer a higher tolerance to the $l = 1$ perturbation. The effective yield of the symmetric implosion with 30keV hot-electrons is 1.88×10^{11} kg^2 eV^4 m^{-3} and values relative to this are shown in brackets in Tables 5.2 and 5.3. As the perturbation amplitude increases, the hotspot volume is stable and stays around 1.0×10^{-12}m^3. For each set of results, temperature and density values are inversely proportional to each other, and an increase in one parameter results in the reduction of the other. The effective yield of the implosion also appears fairly stable in the range of 1.6-2$\times10^{11}$ kg^2 eV^4 m^{-3} (85-110%).

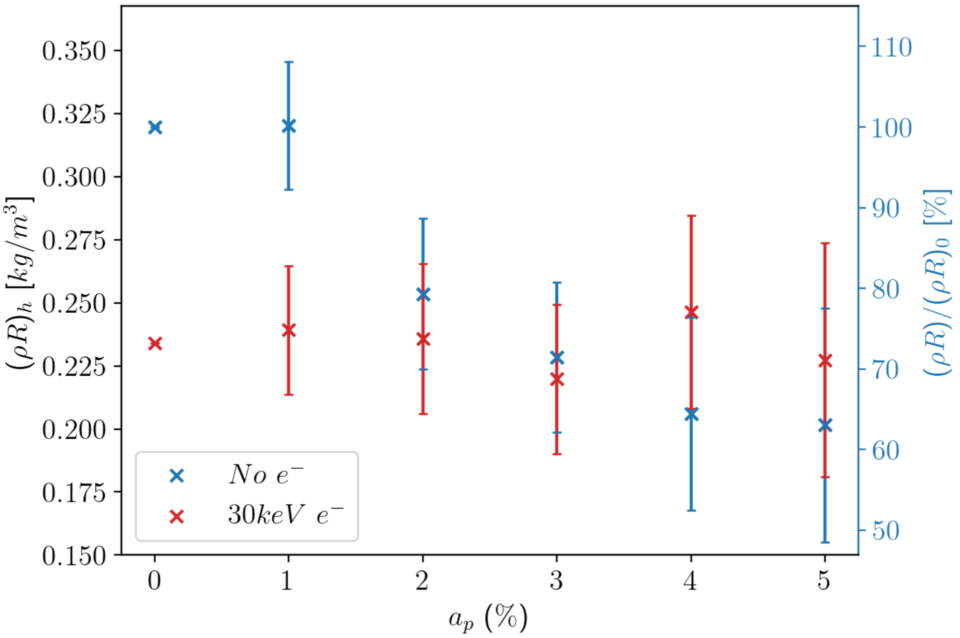

Figure 5.5: Including hot-electrons. Average hotspot areal density, $(\rho R)_h$, plotted as a function of perturbation amplitude. The values obtained from simulations with $30keV$ hot electrons are shown in red, and the results from simulations excluding hot electrons are shown in blue. Each cross shows the cell-volume-weighted areal density measurement and the bars show the range of values across the target.

5.4.3 Discussion

The inclusion of hot-electrons in simulations are shown to decrease the implosion performance, but they offset a higher tolerance to the $l = 1$ mode perturbation. It is possible that hot-electrons more effectively diffuse the energy of the laser across the target and reduce the presence of perturbations in the overall energy deposition. Additionally, laser preheat reduces the peak density of the imploding shockwave, and therefore dampens the structure of any perturbations that form. Although hot-electrons have the benefit of increasing hotspot robustness, this does not outweigh the cost they inflict to implosion performance.

Laser power misbalance				
Amplitude (%)	V_h $[m^3]$	ρ_h $[kg/m^3]$	$T_{i,h}$ $[keV]$	Y_{eff} (%)
0 (no e^-)	7.09×10^{-13}	3.13×10^4	5.63	100
0.0	1.04×10^{-12}	2.02×10^4	4.59	26.8 (100)
1.0	1.00×10^{-12}	2.10×10^4	4.63	29.1(108)
2.0	1.02×10^{-12}	2.08×10^4	4.57	27.5 (102)
3.0	1.08×10^{-12}	1.89×10^4	4.50	22.8 (85.2)
4.0	1.15×10^{-12}	2.10×10^4	4.22	23.1 (86.1)
5.0	1.10×10^{-12}	1.93×10^4	4.59	26.0 (97.0)

Table 5.2: The results of a parameter scan in power misbalance ($l = 1$ perturbation), showing the effect of increasing amplitude on a series of important implosion metrics including hotspot volume, V_h, density, ρ_h, ion temperature, $T_{i,h}$ and effective yield, Y_{eff}.

5.5 Laser-Target Offset

5.5.1 Simulation Setup

For this investigation, we conducted a similar scan of laser offset values from $5\mu m$ to 30 μm but with the inclusion of 30keV hot-electrons during the main laser pulse. Although the majority of the simulations were conducted using the Lagrangian scheme, for some simulations it was necessary to run in fully Eulerian mode with a fixed grid to reach peak compression. The $\delta y = 25\mu m$ and $\delta y = 30\mu m$ simulations used a fixed grid from 9.8ns and 10.1ns, respectively.

5.5.2 Results

The results of our offset simulations show once again that the presence of hot-electrons reduces the effect of applied laser offset on implosion performance. Figure 5.5 shows a slight negative correlation with increasing laser offset, but it is only beyond $\delta y = 20\mu m$, that this becomes apparent. These results show that small offset can cause an increase in areal density of the hotspot. This could indicate that the offset causes more of the electrons to miss the cold shell, compared with the standard case. For an offset of $30\mu m$, there is a 23% decrease in areal density with respect to the case where there is no laser offset. In the absence of hot-electrons, an offset of $30\mu m$ causes a more significant decrease of 36% in areal density. Note that the range of areal density values increases with offset, as previously seen in section 4.5.3, indicating that there is a larger asymmetry in the shape of the hotspot at peak compression.

Other implosion parameters, and the effective yield of the simulations are

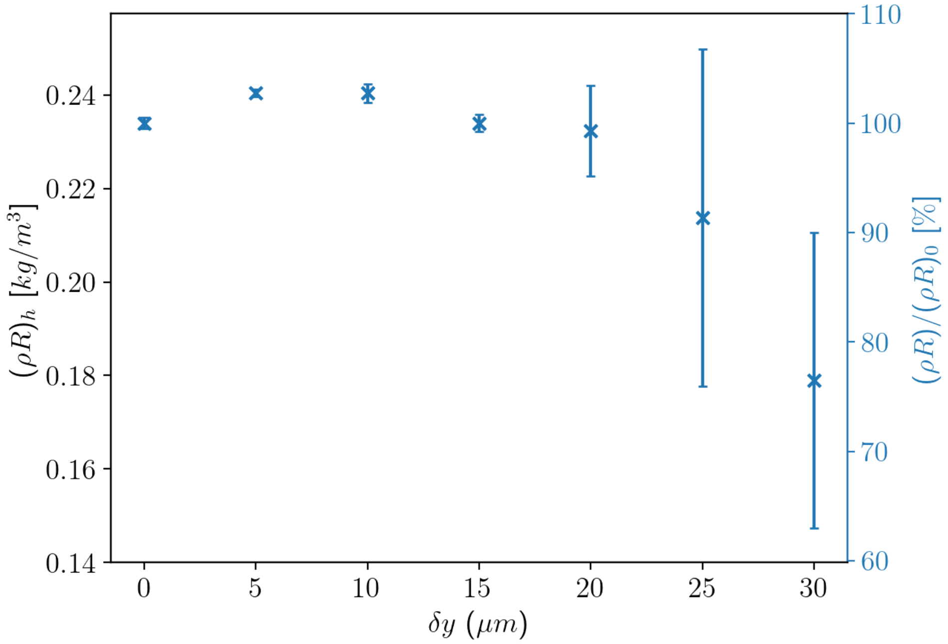

Figure 5.6: Including hot-electrons. Average hotspot areal density, $(\rho R)_h$, plotted as a function of laser offset. Each cross shows the cell-volume-averaged areal density measurement and the bars show the range of values across the target.

shown below in Table 5.3. As offset increases, we see a general decrease in the effective yield along with the hotspot temperature, volume and density. These parameters are more sensitive to laser nonuniformities than areal density, and increasing offset is detrimental to them. The most indicative parameter of reduced implosion performance with offset appears to be hotspot density, which reduces with increasing amplitude.

5.5.3 Discussion

Our simulations with the inclusion of 30keV hot-electrons show a negative correlation between areal density and laser offset. The spread of hot-electrons throughout the target is likely to reduce the preferential heating of the upper quadrant of the target, and lead to less significant asymmetry. The distance between the critical surface and ablation front at 6ns, when the hot electrons are generated by the high intensity spike of the laser drive, is $\sim 330\mu m$. This distance can be travelled by hot electrons with temperatures of the order keV as modelled in our simulations and was verified by viewing the paths of a sample of the hot electrons. Laser offset appears to be

Laser Offset				
Offset, δy (μm)	V_h [m^3]	ρ_h [kg/m^3]	$T_{i,h}$ [keV]	Y_{eff} (%)
0 (no e^-)	7.09×10^{-13}	3.13×10^4	5.63	100
0	1.04×10^{-12}	2.02×10^4	4.59	26.8 (100)
5	9.98×10^{-13}	2.10×10^4	4.66	29.7 (111)
10	9.98×10^{-13}	2.08×10^4	4.66	29.6 (111)
15	1.04×10^{-12}	1.89×10^4	4.59	26.8 (100)
20	1.05×10^{-12}	2.10×10^4	4.56	26.2 (97.9)
25	1.80×10^{-12}	1.93×10^4	4.26	28.1 (105)
30	5.13×10^{-12}	1.93×10^4	3.04	8.58 (32.0)

Table 5.3: The results of a parameter scan in laser-target offset, showing the effect of increasing offset on a series of important implosion metrics including hotspot volume, V_h, density, ρ_h, ion temperature, $T_{i,h}$ and effective yield, Y_{eff}.

impose a higher degree of asymmetry on capsule implosion which is likely down to a larger number of rays missing the target as offset increases. Measurements of areal density demonstrate a similar robustness to small laser offset, as was the case for simulations of implosions driven solely by the laser energy deposition. For higher values of laser offset, $\delta y > 20\mu m$, the impact to implosion performance is more noticeable and all implosion parameters are effected, and we see a larger spread of hotspot areal density values. A comparison of the measured areal density for offset simulations with and without hot-electrons is shown in fig. 5.7.

5.6 Chapter Summary

The results presented in this chapter show that although hot-electrons reduce implosion performance, they can mitigate the impact of nonuniformities. Laser offset simulations showed a less significant correlation with reduced hotspot areal density. Our measurements of areal density for varying amplitudes of the $l = 1$ power perturbation showed no correlation. Distributions of electrons with higher temperatures are more detrimental on target compression up to 30keV, at which point the areal density has dropped by 30%. Beyond this temperature implosions appear to have a similar performance, and there is a slight improvement in implosion parameters with hot-electrons of 50keV and 60keV.

Since hot-electrons of temperatures, ranging between 20-60keV [Solodov et al., 2016], are known to be present in direct-drive ICF experiments, we can state that they are a limiting factor for achieving optimised compression of DT fuel. Our simulations have shown that the inclusion of 30keV hot-electrons reduces the areal density at peak compression by $\sim 27\%$. We suggest the reason for

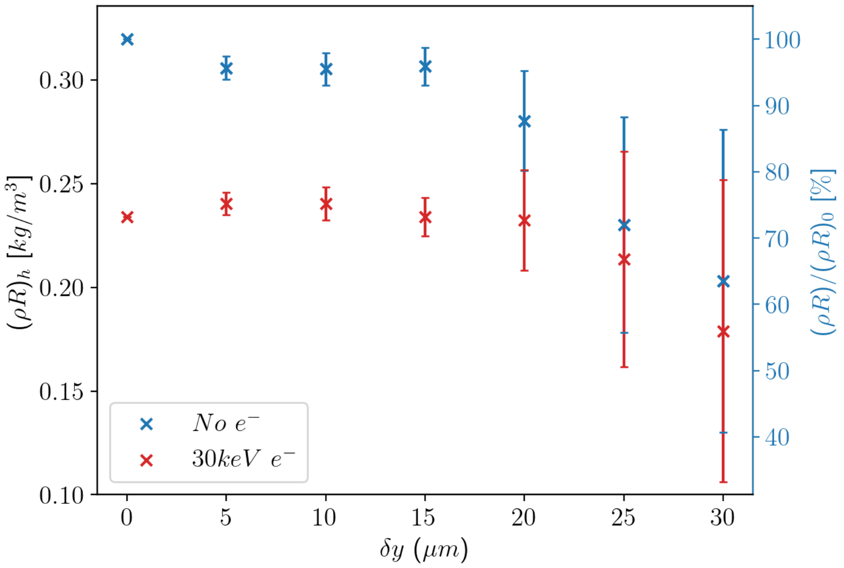

Figure 5.7: Average hotspot areal density, $(\rho R)_h$, plotted as a function of laser offset for simulations with (red) and without (blue) $30keV$ hot-electrons. Each cross shows the average areal density measurement and the bars show the range of values across the target.

hot-electrons offering resistance to laser nonuniformities is that preheat reduces the density of the imploding shockwave and makes perturbations less influential on the implosion structure. In addition, electron scattering allows energy deposition across all regions of the capsule and smooths out any regions of preferential heating.

Chapter 6

Conclusions and Future Work

In this thesis, the results of 2D radiation-hydrodynamic code development and simulation are presented, and are used to investigate the impact of laser nonuniformities on implosion performance for ignition-scale direct-drive experiments. Building on previous studies that have been conducted into sources of implosion asymmetry for direct-drive facilities, the work and simulations presented in this thesis are novel in that they investigate these issues for ignition-scale experiments, and have included hot-electrons to account for those created as a result of laser plasma instabilities. Chapter 3 describes the implementation of new features to the 2D radiation-hydrodynamics code *Odin* to improve its capability for running simulations of laser-driven inertial confinement fusion. Using these new features, we conducted investigations into the impact of various sources of laser and target non-uniformities on implosion performance as discussed in Chapter 4. In Chapter 5, a similar analysis was conducted with the inclusion of *Odin's* hot electron routine, a novel feature that is not often present in radiation-hydrodynamic codes. In this final chapter, we summarise the findings of this thesis, and discuss possible avenues of investigation for future work.

6.1 Conclusions

The main investigation of this thesis was to understand and quantify the impact of laser nonuniformities on ignition-scale direct-drive implosions. Previous studies investigating are predominantly focused on OMEGA scale experiments and corresponding simulations, this work presents one of the first attempts to see the impact of implosion asymmetry in ignition-scale direct drive ICF experiments. By implementing new features into the 2D radiation-hydrodynamics code *Odin*, as discussed in Chapter

3, we conducted a series of simulations to study the effect of the $l = 1$ laser power perturbation, and laser offset over a range of amplitudes. Chapter 4 discusses the results of these simulations without the inclusion of hot electrons, and Chapter 5 presents the result of simulation with the inclusion of hot electrons. The results show that these sources of asymmetry will still be problematic at ignition-scale and future facilities will want to reduce the presence of laser non-uniformities and hot-electrons.

The addition of multiple features to *Odin* was discussed in Chapter 3. In summary, the features are as follows. A refractive 3D ray-tracing model was implemented, with energy deposition through inverse bremßtrahlung, and a simplified resonance absorption model. The ray-tracing scheme is merged with the previously existing hot electron routine, and can therefore be used to generate a thermally distributed population of electrons at the quarter-critical density to emulate the effect of LPIs, as discussed in section 1.6.5. To improve ray trajectories and energy deposition, face-normal interpolation and binomial filtering were added to the ray-tracing model. Note that although binomial filtering has been implemented, for most simulations it is not required since face-normal interpolation eliminates artificial filamentation. In a planar test case with a linear density profile and uniformly spaced cells, the ray paths were found to be accurate to within 2% of the turning point on average, over a range of angles of incidence, for resolutions of 100 cells and above. For resolutions of 600 cells and above, the deviation of the ray-tracing path from the analytic solution was reduced to less than 0.4%.

Coupled with the ray-tracing routine, we described the implementation of artificial laser non-uniformities in *Odin*. A harmonic perturbation of chosen amplitude and mode can be applied to the laser power profile to replicate the response of macroscopic and microscopic non-uniformities that arise in laser fusion experiments (section 1.6.1). The addition of a laser-target offset tool to displace the position of all rays by a chosen amount was also made.

Using the features described above, we investigated the impact of such laser non-uniformities on the implosion performance. The areal density of the hotspot at peak compression was used as a proxy for the yield and performance of the implosion. A $l = 1$ harmonic perturbation was applied to the laser power profile to emulate the effect of macroscopic nonuniformities such as laser mistiming, beam power misbalance and stalk connection. Low l-mode perturbations are reduced least by thermal smoothing, and can be present through all stages of ICF implosions. Our simulations show that an increasing amplitude of this perturbation led to a decrease in implosion performance and the areal density of the hotspot. Over a range of amplitudes between 0.5-5%, we found a decrease in areal density as a function of the perturbation amplitude. At an amplitude of 5%, the areal density of the hotspot reduced by ∼37% compared to uniform compression. A similar decrease was found from simulating target implosions for a range of laser offsets between $5\mu m$ and $30\mu m$.

Chapter 5 presented the results of asymmetric implosions with the inclusion of hot electrons. *Odin's* hot electron routine is a novel feature that is not generally included in radiation-hydrodynamic codes, therefore, the simulations presented in this chapter are likely the first of its kind. The simulations showed that hot electrons are detrimental to implosion performance and, in preheating the DT fuel, they reduced the compression of the target. In the symmetric case, hot electrons of 30keV and above deteriorated the areal density of the hotspot at peak compression by ∼27%. This shows that electron preheat is problematic to ICF experiments. Although hot electrons were found to deteriorate implosion performance, they did reveal some tolerance to laser nonuniformities. For simulations which included 30keV hot-electrons, the reduction in hotspot areal density at peak compression with an applied $a_p = 5\%$ power perturbation, and a symmetric implosion was only 1%. This suggests that hot-electrons work to distribute their energy throughout the target and can smooth any perturbations that form.

6.2 Future Work

The implementations added to *Odin*, open many possible avenues of investigation and might also improve the accuracy of ICF simulations. We quantified the impact of laser nonuniformities on hotspot areal density and effective yield. The beam configuration used in our simulations gives an exaggerated result for the impact of laser nonuniformities on target implosion since each beam was directed towards a relatively small region of the capsule. Experimental configurations have beams which overlap on the surface of the target and are not as susceptible to perturbations forming in the profile of the imploding shockwave. Future studies could investigate the effect of laser nonuniformities applied to such configurations.

Implementing experimental beam configurations into *Odin* would allow us to replicate experiments conducted at laser facilities such as OMEGA, NIF, Laser Mégajoule, Vulcan, and ORION. Using experimental data from these facilities, it would be possible to fine-tune user-defined parameters in *Odin*, such as resonance absorption, CBET power loss, and the flux-limiter value. With optimised values, we could then perform predictive simulations.

In their paper, Hu *et al.* [Hu et al., 2010], simulated implosions with an applied ice roughness of varying widths. Ice roughness is known to seed hydrodynamic instabilities and is detrimental to implosion performance. Given more time, the author would have conducted similar simulations to quantify the impact of this feature on ICF experiments. Hu *et al.* also presented the combined impact of multiple sources of asymmetry, such as laser offset and ice roughness.

It was also hoped that, using the *wedge* boundary conditions, it would be possible to simulate a high mode laser power perturbation ($l \geq 200$) as a proxy to study the effect of speckles in ICF implosions. Unfortunately, these simulations cause the current thermal conduction routine to fail, and further development to *Odin* is needed to handle the distortions seen in these simulations.

Although we also conducted simulations to investigate the impact of hot electrons of varying temperature on ICF implosions, we used a fixed angular spread throughout. In future, it would be useful to perform a sensitivity analysis of hot-electrons and to investigate the impact of electron spread on target preheat and implosion performance. We would expect a larger spread of electrons to cause less preheat of the DT fuel and have a less detrimental effect on implosion performance. To simulate the populations of hot-electrons generated from each LPI, they could be separated and modelled as independent distributions with unique temperatures and angular spread.

Another useful extension of this work would be to conduct similar simulations for alternative direct-drive ICF schemes, such as shock ignition [Scott et al., 2021] and shock-augmented ignition [Scott et al., 2020]. Such schemes use high laser intensities, with significant contrast, that stimulate LPIs and the generation of hot electrons. Using *Odin*'s hot electron routine, we could simulate the effect of such laser nonuniformites on these schemes of ICF.

Bibliography

[GEO, 2022] (2022). Mineral commodity summaries 2022. Technical report, US Geological Survey.

[Aglitskiy et al., 2010] Aglitskiy, Y., Velikovich, A. L., Karasik, M., Metzler, N., Zalesak, S. T., Schmitt, A. J., Phillips, L., Gardner, J. H., Serlin, V., Weaver, J. L., and Obenschain, S. P. (2010). Basic hydrodynamics of richtmyer–meshkov-type growth and oscillations in the inertial confinement fusion-relevant conditions. *Philosophical Transactions of the Royal Society As*, 368:1739–1768.

[Anderson, 2006] Anderson, K. S. (2006). *Adiabat Shaping in Direct-Drive Inertial Confinement Fusion Implosions.* PhD thesis, University of Rochester.

[Arber et al., 2001] Arber, T. D., Longbottom, A. W., Gerrard, C. L., and Milne, A. M. (2001). A staggered grid, Lagrangian-Eulerian remap code for 3-D MHD simulations. *Journal of Computational Physics*, 171(1):151–181.

[Ascoli-Bartoli, 1965] Ascoli-Bartoli, U. (1965). Plasma diagnostics based on refractivity. *International Atomic Energy Agency, Vienna.*

[Atzeni et al., 2009] Atzeni, S., Schiavi, A., and Davies, J. R. (2009). Stopping and scattering of relativistic electron beams in dense plasmas and requirements for fast ignition. *Plasma Physics and Controlled Fusion*, 51:015016.

[Atzeni and ter Vehn, 2004] Atzeni, S. and ter Vehn, J. M. (2004). *The Physics of Inertial Fusion.* Oxford University Press.

[Baldwin et al., 1999] Baldwin, C., Brown, P. N., Falgout, R., Graziani, F., and Jones, J. (1999). Iterative linear solvers in a 2d radiation–hydrodynamics code: Methods and performance. *Journal of Computational Physics*, 154(1):1–40.

[Barlow, 2021] Barlow, D. (2021). *Inertial Confinement Fusion: Energy Transport and Shock Ignition.* PhD thesis, University of Warwick.

[Barlow et al., 2022] Barlow, D., Goffrey, T., Bennett, K., Scott, R. H. H., Glize, K., Theobald, W., Anderson, K., Solodov, A. A., Rosenberg, M. J., Hohenberger, M., Woolsey, N. C., Bradford, P., Khan, M., and Arber, T. D. (2022). Role of hot electrons in shock ignition constrained by experiment at the national ignition facility. *Physics of Plasmas*, 29:082704.

[Barnes and Lyon, 1988] Barnes, J. and Lyon, S. (1988). Sesame: The los alamos national laboratory equation of state database. Technical report, Los Alamos National Laboratory.

[Bennett et al., 2021] Bennett, K., Goffrey, T., and Arber, T. (2021). User manual for the odin code.

[Benson, 1992] Benson, D. J. (1992). Computational methods in Lagrangian and Eulerian hydrocodes. *Computer Methods in Applied Mechanics and Engineering*, 99(2-3):235–394.

[Benson, 2013] Benson, D. J. (2013). *Introduction to Arbitrary Lagrangian-Eulerian in Finite Element Methods*. Arbitrary Lagrangian-Eulerian and Fluid Structure interaction.

[Betti and Hurricane, 2016] Betti, R. and Hurricane, O. (2016). Inertial-confinement fusion with lasers. *Nature Physics*, 12:435–448.

[Biermann, 1950] Biermann, L. (1950). Über den Ursprung der Magnetfelder auf Sternen und im interstellaren Raum. *Zeitschrift für Naturforschung. A. Physik, Physikalische Chemie, Kosmophysik*, 5:65–71.

[Bodner, 1981] Bodner, S. E. (1981). Critical elements of high gain laser fusion. *J. Fusion Energy*, 1:221–240.

[Boehly et al., 1999] Boehly, T. R., Smalyuk, V. A., Meyerhofer, D. D., Knauer, J. P., Bradley, D. K., Craxton, R. S., Guardalben, M. J., Skupsky, S., and Kessler, T. J. (1999). Reduction of laser imprinting using polarization smoothing on a solid-state fusion laser. *Journal of Applied Physics*, 85:3444–3447.

[Braginskii, 1965] Braginskii, S. I. (1965). Transport processes in a plasma. *Reviews of Plasma Physics*, 1:205.

[Burton et al., 2013] Burton, D. E., Morgan, N. R., and Carney, T. C. (2013). On the question of area weighting in cell-centered hydrodynamics. Technical report, Los Alamos National Laboratory.

[Campbell et al., 2017] Campbell, E., Goncharov, V., Sangster, T., Regan, S., Radha, P., Betti, R., Myatt, J., Froula, D., Rosenberg, M., Igumenshchev, I., Seka, W., Solodov, A., Maximov, A., Marozas, J., Collins, T., Turnbull, D., Marshall, F., Shvydky, A., Knauer, J., McCrory, R., Sefkow, A., Hohenberger, M., Michel, P., Chapman, T., Masse, L., Goyon, C., Ross, S., Bates, J., Karasik, M., Oh, J., Weaver, J., Schmitt, A., Obenschain, K., Obenschain, S., Reyes, S., and Van Wonterghem, B. (2017). Laser-direct-drive program: Promise, challenge, and path forward. *Matter and Radiation at Extremes*, 2(2):37–54.

[Caramana et al., 1998] Caramana, E. J., Burton, D. E., Shashkov, M. J., and Whalen, P. P. (1998). The construction of compatible hydrodynamics algorithms utilizing conservation of total energy. *Journal of Computational Physics*, 146(1):227–262.

[Casey et al., 2021] Casey, D., MacGowan, B., Sater, J., Zylstra, A., Landen, O., Milovich, J., Hurricane, O., Kritcher, A., Hohenberger, M., Baker, K., Pape, S. L., Döppner, T., Weber, C., Huang, H., Kong, C., Biener, J., Young, C., Haan, S., Nora, R., Ross, S., Robey, H., Stadermann, M., Nikroo, A., Callahan, D., Bionta, R., Hahn, K., Moore, A., Schlossberg, D., Bruhn, M., Sequoia, K., Rice, N., Farrell, M., and Wild, C. (2021). Evidence of three-dimensional asymmetries seeded by high-density carbon-ablator nonuniformity in experiments at the national ignition facility. *Physical Review Letters*, 126(2):025002.

[Charney et al., 1950] Charney, J. G., FjÖrtoft, R., and Neumann, J. V. (1950). Numerical integration of the barotropic vorticity equation. *Taylor Francis*, 2:237–254.

[Christensen et al., 2004] Christensen, C. R., Wilson, D. C., Barnes, C. W., Grim, G. P., Morgan, G. L., Wilke, M. D., Marshall, F. J., Glebov, V. Y., and Stoeckl, C. (2004). The influence of asymmetry on mix in direct-drive inertial confinement fusion experiments. *Physics of Plasmas*, 11(5):2771–2777.

[Christopherson et al., 2021] Christopherson, A. R., Betti, R., Forrest, C. J., Howard, J., Theobald, W., Delettrez, J. A., Rosenberg, M. J., Solodov, A. A., Stoeckl, C., Patel, D., Gopalaswamy, V., Cao, D., Peebles, J. L., Edgell, D. H., Seka, W., Epstein, R., Wei, M. S., Gatu Johnson, M., Simpson, R., Regan, S. P., and Campbell, E. M. (2021). Direct measurements of dt fuel preheat from hot electrons in direct-drive inertial confinement fusion. *Physical review letters*, 127:055001.

[Christopherson et al., 2020] Christopherson, A. R., Betti, R., Miller, S., Gopalaswamy, V., Mannion, O. M., and Cao, D. (2020). Theory of ignition and burn propagation in inertial fusion implosions. *Physics of Plasmas*, 27:052708.

[Clark et al., 2010] Clark, D. S., Haan, S. W., Hammel, B. A., Salmonson, J. D., Callahan, D. A., and Town, R. P. J. (2010). Plastic ablator ignition capsule design for the national ignition facility. *Physics of Plasmas*, 244:022010.

[Clery, 2022] Clery, D. (2022). European fusion reactor sets record for sustained energy. *Science*, 375:600–600.

[Colaïtis et al., 2016] Colaïtis, A., Hüller, S., Pesme, D., Duchateau, G., and Tikhonchuk, V. T. (2016). Crossed beam energy transfer: Assessment of the paraxial complex geometrical optics approach versus a time-dependent paraxial method to describe experimental results. *Physics of Plasmas*, 23(3):032118.

[Courant et al., 1986] Courant, R., Friedrichs, K., and Lewy, H. (1986). On the partial difference equations of mathematical physics.

[Craxton et al., 2015] Craxton, R. S., Anderson, K. S., Boehly, T. R., Goncharov, V. N., Harding, D. R., Knauer, J. P., McCrory, R. L., McKenty, P. W., Meyerhofer, D. D., Myatt, J. F., Schmitt, A. J., Sethian, J. D., Short, R. W., Skupsky, S., Theobald, W., Kruer, W. L., Tanaka, K., Betti, R., Collins, T. J. B., Delettrez, J. A., Hu, S. X., Marozas, J. A., Maximov, A. V., Michel, D. T., Radha, P. B., Regan, S. P., Sangster, T. C., Seka, W., Solodov, A. A., Soures, J. M., Stoeckl, C., and Zuegel, J. D. (2015). Direct-drive inertial confinement fusion: A review. *Physics of Plasmas*, 22(11):110501.

[Day, 1990] Day, M. A. (1990). The no-slip condition of fluid dynamics. *Erkenntnis*, 33:285–296.

[Debayle et al., 2019] Debayle, A., Ruyer, C., Morice, O., Masson-Laborde, P.-E., Loiseau, P., and Benisti, D. (2019). A unified modeling of wave mixing processes with the ray tracing method. *Physics of Plasmas*, 26(9):092705.

[Denisov, 1956] Denisov, N. G. (1956). On a singularity of the field of an electromagnetic wave propagated in an inhomogeneous plasma. *Soviet Physics, JETP*, 4:544–553.

[Denton and Hu, 2009] Denton, R. E. and Hu, Y. (2009). Symmetry boundary conditions. *Journal of Computational Physics*, 228(13):4823–4835.

[Ding et al., 2020] Ding, J., Yang, P., Mishchenko, M. I., and Nevels, R. D. (2020). Identify the limits of geometric optics ray tracing by numerically solving the vector kirchhoff integral. *Optics Express*, 28:10670.

[EIA, 2021] EIA (2021). Net zero by 2050. Technical report.

[Emery et al., 1991] Emery, M. H., Gardner, J. H., Lehmberg, R. H., and Obenschain, S. P. (1991). Hydrodynamic target response to an induced spatial incoherence-smoothed laser beam. *Physics of Fluids B*, 3:2640–2651.

[Epperlein and Short, 1991] Epperlein, E. M. and Short, R. W. (1991). A practical nonlocal model for electron heat transport in laser plasmas. *Physics of Fluids B: Plasma Physics*, 3(11):3092–3098.

[Estabrook et al., 1975] Estabrook, K. G., Valeo, E. J., and Kruer, W. L. (1975). Two-dimensional relativistic simulations of resonance absorption. *Physics of Fluids*, 18(9):1151.

[Faik et al., 2018] Faik, S., Tauschwitz, A., and Iosilevskiy, I. (2018). The equation of state package FEOS for high energy density matter. *Comput. Phys. Commun.*, 227:117–125.

[Forslund et al., 1975] Forslund, D. W., Kindel, J. M., Lee, K., Lindman, E. L., and Morse, R. L. (1975). Theory and simulation of resonant absorption in a hot plasma. *Physical Review A*, 11(679).

[Forties and Marshall, 2005] Forties, R. A. and Marshall, F. J. (2005). In situ characterization of high-intensity laser beams on omega. *Review of Scientific Instruments*, 76(7):073505–073505–4.

[Fraley et al., 1974] Fraley, G. S., Linnebur, E. J., Mason, R. J., and Morse, R. L. (1974). Thermonuclear burn characteristics of compressed deuterium–tritium microspheres. *The Physics of Fluids.*

[Frederikse et al., 2020] Frederikse, T., Landerer, F., Caron, L., Adhikari, S., Parkes, D., Humphrey, V. W., Dangendorf, S., Hogarth, P., Zanna, L., Cheng, L., and Wu, Y.-H. (2020). The causes of sea-level rise since 1900. *Nature*, 584:393–397.

[Froula et al., 2012] Froula, D. H., Michel, D. T., Igumenshchev, I. V., Hu, S. X., Yaakobi, B., Myatt, J. F., Edgell, D. H., Follett, R., Glebov, V. Y., Goncharov, V. N., Kessler, T. J., Maximov, A. V., Radha, P. B., Sangster, T. C., Seka, W., Short, R. W., Solodov, A. A., Sorce, C., and Stoeckl, C. (2012). Laser–plasma interactions in direct-drive ignition plasmas. *Plasma Physics and Controlled Fusion*, 54:124016.

[Gaffney et al., 2018] Gaffney, J. A., Hu, S. X., Arnault, P., Becker, A., Benedict, L. X., Boehly, T. R., Celliers, P. M., Ceperley, D. M., Čertík, O., Clérouin, J., Collins, G. W., Collins, L. A., Danel, J. F., Desbiens, N., Dharma-wardana, M. W. C., Ding, Y. H., Fernandez-Pañella, A., Gregor, M. C., Grabowski, P. E., Hamel, S., Hansen, S. B., Harbour, L., He, X. T., Johnson, D. D., Kang, W., Karasiev, V. V., Kazandjian, L., Knudson, M. D., Ogitsu, T., Pierleoni, C., Piron, R., Redmer, R., Robert, G., Saumon, D., Shamp, A., Sjostrom, T., Smirnov, A. V., Starrett, C. E., Sterne, P. A., Wardlow, A., Whitley, H. D., Wilson, B., Zhang, P., and Zurek, E. (2018). A review of equation-of-state models for inertial confinement fusion materials. *High Energy Density Physics*, 28:7–24.

[Gibney, 2022] Gibney, E. (2022). Nuclear-fusion reactor smashes energy record. *Nature*, 602:371–371.

[Glassner, 1989] Glassner, A. S. (1989). *An Introduction to Ray tracing (The Morgan Kaufmann Series in Computer Graphics)*. The Morgan Kaufmann Series in Computer Graphics. Morgan Kaufmann, Saint Louis. Description based upon print version of record.

[Goffrey, 2014] Goffrey, T. (2014). *A cylindrical magnetohydrodynamic arbitrary Lagrangian Eulerian code*. PhD thesis, University of Warwick.

[Goncharov et al., 2006] Goncharov, V. N., Gotchev, O. V., Vianello, E., Boehly, T. R., Knauer, J. P., McKenty, P. W., Radha, P. B., Regan, S. P., Sangster, T. C., Skupsky, S., Smalyuk, V. A., Betti, R., McCrory, R. L., Meyerhofer, D. D., and Cherfils-Clérouin, C. (2006). Early stage of implosion in inertial confinement fusion: Shock timing and perturbation evolution. *Physics of Plasmas*, 13:012702.

[Goncharov et al., 2016] Goncharov, V. N., Regan, S. P., Campbell, E. M., Sangster, T. C., Radha, P. B., Myatt, J. F., Froula, D. H., Betti, R., BOehly, T. R., and Delettrez, J. A. (2016). National direct-drive program on omega and the national ignition facility. *Plasma Physics and Controlled Fusion*, 59(014008).

[Goncharov et al., 2010] Goncharov, V. N., Sangster, T. C., Boehly, T. R., Hu, S. X., Igumenshchev, I. V., Marshall, F. J., McCrory, R. L., Meyerhofer, D. D., Radha, P. B., Seka, W., Skupsky, S., Stoeckl, C., Casey, D. T., Frenje, J. A., and Petrasso, R. D. (2010). Demonstration of the highest deuterium-tritium areal density using multiple-picket cryogenic designs on omega. *Physical Review Letters*, 104.

[Goncharov et al., 2008] Goncharov, V. N., Sangster, T. C., Radha, P. B., Betti, R., Delettrez, J. A., Epstein, R., Harding, D. R., Hu, S. X., Igumenshchev, I. V., Marshall, F. J., McCrory, R. L., McKenty, P. W., Meyerhofer, D. D., Regan, S. P., Seka, W., Shvarts, D., Skupsky, S., Smalyuk, V. A., Stoeckl, C., Frenje, J. A., Li, C. K., and Petrasso, R. D. (2008). Modeling high-compression, direct-drive, icf experiments. In *Journal of Physics Conference Series*, volume 112 of *Journal of Physics Conference Series*, page 022002.

[Gopalaswamy et al., 2019] Gopalaswamy, V., Betti, R., Knauer, J. P., Luciani, N., Patel, D., Woo, K. M., Bose, A., Igumenshchev, I. V., Campbell, E. M., Anderson, K. S., Bauer, K. A., Bonino, M. J., Cao, D., Christopherson, A. R., Collins, G. W., Collins, T. J. B., Davies, J. R., Delettrez, J. A., Edgell, D. H., Epstein, R., Forrest, C. J., Froula, D. H., Glebov, V. Y., Goncharov, V. N., Harding, D. R., Hu, S. X., Jacobs-Perkins, D. W., Janezic, R. T., Kelly, J. H., Mannion, O. M., Maximov, A., Marshall, F. J., Michel, D. T., Miller, S., Morse, S. F. B., Palastro, J., Peebles, J., Radha, P. B., Regan, S. P., Sampat, S., Sangster, T. C., Sefkow, A. B., Seka, W., Shah, R. C., Shmyada, W. T., Shvydky, A., Stoeckl, C., Solodov, A. A., Theobald, W., Zuegel, J. D., Johnson, M. G., Petrasso, R. D., Li, C. K., and Frenje, J. A. (2019). Tripled yield in direct-drive laser fusion through statistical modelling. *Nature*, 565(7741):581–586.

[Haines et al., 2020] Haines, B. M., Keller, D. E., Marozas, J. A., McKenty, P. W., Anderson, K. S., Collins, T. J. B., Dai, W. W., Hall, M. L., Jones, S., Jr, M. D. M., Rauenzahn, R. M., and Woods, D. N. (2020). Coupling laser physics to radiation-hydrodynamics. *Computers Maths: Fluids*, 201:104478.

[Harding, 2005] Harding, D. R. (2005). Forming smooth cryogenic targets for omega direct-drive icf implosions and prospects for direct-drive targets for the nif. In *47th Annual Meeting of the American Physical Society, Division of Plasma Physics*. 47th Annual Meeting of the American Physical Society, Division of Plasma Physics.

[Harding et al., 2009] Harding, E. C., Hansen, J. F., Hurricane, O. A., Drake, R. P., Robey, H. F., Kuranz, C. C., Remington, B. A., Bono, M. J., Grosskopf, M. J., and Gillespie, R. S. (2009). Observation of a kelvin-helmholtz instability in a high-energy-density plasma on the omega laser. *Physical Review Letters*, 103.

[Hu et al., 2010] Hu, S. X., Goncharov, V. N., Radha, P. B., Marozas, J. A., Skupsky, S., Boehly, T. R., Sangster, T. C., Meyerhofer, D. D., and McCrory, R. L. (2010). Two-dimensional simulations of the neutron yield in cryogenic deuterium-tritium implosions on omega. *Physics of Plasmas*, 17(10):102706.

[Hu et al., 2009] Hu, S. X., Radha, P. B., Marozas, J. A., Betti, R., Collins, T. J. B., Craxton, R. S., Delettrez, J. A., Edgell, D. H., Epstein, R., Goncharov, V. N., Igumenshchev, I. V., Marshall, F. J., McCrory, R. L., Meyerhofer, D. D., Regan, S. P., Sangster, T. C., Skupsky, S., Smalyuk, V. A., Elbaz, Y., and Shvarts, D. (2009). Neutron yield study of direct-drive, low-adiabat cryogenic d2 implosions on omega laser system. *Physics of Plasmas*, 16:112706.

[Hu et al., 2008] Hu, S. X., Smalyuk, V. A., Goncharov, V. N., Knauer, J. P., Radha, P. B., Igumenshchev, I. V., Marozas, J. A., Stoeckl, C., Yaakobi, B., Shvarts, D., Sangster, T. C., McKenty, P. W., Meyerhofer, D. D., Skupsky, S., and McCrory, R. L. (2008). Studies of plastic-ablator compressibility for direct-drive inertial confinement fusion on omega. *Physical Review Letters*, 100.

[Huang and Li, 2018] Huang, C. and Li, L. (2018). Magnetic confinement fusion: a brief review. *Frontiers in Energy*, 12(2):305–313.

[Igumenshchev et al., 2010] Igumenshchev, I. V., Edgell, D. H., Goncharov, V. N., Delettrez, J. A., Maximov, A. V., Myatt, J. F., Seka, W., Shvydky, A., Skupsky, S., and Stoeckl, C. (2010). Crossed-beam energy transfer in implosion experiments on omega. *Physics of Plasmas*, 17:122708.

[Iwan, 1984] Iwan, L. (1984). Illumination-uniformity considerations for direct-drive fusion reactors. *LLE Review Quarterly Report*, 19:120.

[Jacquemot, 2017] Jacquemot, S. (2017). Inertial confinement fusion for energy: overview of the ongoing experimental, theoretical and numerical studies. *Nuclear Fusion*, 57(10):102024.

[Johnson et al., 2018] Johnson, M. G., Appelbe, B. D., Chittenden, J. P., Delettrez, J., Forrest, C., Frenje, J. A., Glebov, V. Y., Grimble, W., Haines, B. M., Igumenshchev, I., Janezic, R., Knauer, J. P., Lahmann, B., Marshall, F. J., Michel, T., Séguin, F. H., Stoeckl, C., Walsh, C., Zylstra, A. B., and Petrasso, R. D. (2018). Impact of asymmetries on fuel performance in inertial confinement fusion. *Physical Review E*, 98(5):051201.

[Kaiser, 2000] Kaiser, T. B. (2000). Laser ray tracing and power deposition on an unstructured three-dimensional grid. *Physical Review E*, 61:895–905.

[Kato, 1975] Kato, K. (1975). Frequency conversion of nd:yag laser radiation in rda. *Optics Communications*, 13(2):93–95.

[Kato et al., 1984] Kato, Y., Mima, K., Miyanaga, N., Arinaga, S., Kitagawa, Y., Nakatsuka, M., and Yamanaka, C. (1984). Random phasing of high-power lasers for uniform target acceleration and plasma-instability suppression. *Physical Review Letters*, 53:1057–1060.

[Kawata, 2021] Kawata, S. (2021). Direct-drive heavy ion beam inertial confinement fusion: a review, toward our future energy source. *Advances in Physics: X*, 6(1).

[Kessler et al., 1993] Kessler, T. J., Lin, Y., Armstrong, J. J., and Velazquez, B. (1993). Phase conversion of lasers with low-loss distributed phase plates. *Proceedings of Laser Coherence Control: Technology and Applications*, 1870:95–104.

[Knauer et al., 2000] Knauer, J. P., Betti, R., Bradley, D. K., Boehly, T. R., Collins, T. J. B., Goncharov, V. N., McKenty, P. W., Meyerhofer, D. D., Smalyuk, V. A., Verdon, C. P., Glendinning, S. G., Kalantar, D. H., and Watt, R. G. (2000). Single-mode, rayleigh-taylor growth-rate measurements on the omega laser system. *Physics of Plasmas*, 7:338–345.

[Kravtsov and Berczynski, 2007] Kravtsov, Y. A. and Berczynski, P. (2007). Gaussian beams in inhomogeneous media: A review. *Studia Geophysica et Geodaetica*, 51(1):1–36.

[Kruer, 2003] Kruer, W. L. (2003). *The physics of laser plasma interactions*. Frontiers in physics. Westview Press, Boulder, Colo. [u.a.]. Formerly CIP.

[Kuropatenko, 1963] Kuropatenko, V. F. (1963). On a difference method for the calculation of shock waves. *USSR Computational Mathematics and Mathematical Physics*, 3(1):268–273.

[Laney, 1998] Laney, C. B. (1998). *Computational Gasdynamics*. Cambridge University Press, Cambridge. Title from publisher's bibliographic system (viewed on 05 Oct 2015).

[Larsen, 1989] Larsen, J. T. (1989). Why cryogenic inertial confinement fusion targets? *Journal of Vacuum Science &amp Technology A: Vacuum, Surfaces, and Films*, 7(3):1150–1156.

[Lawson, 1957] Lawson, J. D. (1957). Some criteria for a power producing thermonuclear reactor. *Proceedings of the Physical Society*, 70:6–10.

[Li et al., 2019] Li, B., Nie, Q., Wang, X., Wang, Z., Mao, A., and Chen, P. (2019). Resonant absorption of incident electromagnetic waves in collisional inhomogeneous plasma slabs. *AIP Advances*, 9(9):095020–095020–10.

[Li et al., 2004] Li, C. K., Séguin, F. H., Frenje, J. A., Petrasso, R. D., Delettrez, J. A., McKenty, P. W., Sangster, T. C., Keck, R. L., Soures, J. M., Marshall, F. J., Meyerhofer, D. D., Goncharov, V. N., Knauer, J. P., Radha, P. B., Regan, S. P., and Seka, W. (2004). Effects of nonuniform illumination on implosion asymmetry in direct-drive inertial confinement fusion. *Physical Review Letters*, 92.

[Lindl, 1995] Lindl, J. (1995). Development of the indirect-drive approach to inertial confinement fusion and the target physics basis for ignition and gain. *Physics of Plasmas*, 2(11):3933–4024.

[Lindl and Mead, 1975] Lindl, J. D. and Mead, W. C. (1975). Two-dimensional simulation of fluid instability in laser-fusion pellets. *Physical Review Letters*, 34:1273–1276.

[MacFarlane et al., 2006] MacFarlane, J. J., Golovkin, I. E., and Woodruff, P. R. (2006). Helios-cr – a 1-d radiation-magnetohydrodynamics code with inline atomic kinetics modeling. *Journal of Quantitative Spectroscopy and Radiative Transfer*, 99(1-3):381–397.

[Manheimer et al., 2008] Manheimer, W., Colombant, D., and Goncharov, V. (2008). The development of a krook model for nonlocal transport in laser produced plasmas i. basic theory. In *APS Division of Plasma Physics Meeting Abstracts*, volume 50 of *APS Meeting Abstracts*, page TO4.014.

[Martínez-Val et al., 1993] Martínez-Val, J. M., Eliezer, S., Velarde, G., Hora, H., Honrubia, J. J., Piera, M., Velarde, P., Perlado, J. M., Minguez, E., and Aragonés, J. M. (1993). Numerical and theoretical studies on the ignition of icf plasmas driven by ion beams. *Il Nuovo Cimento A*, 106(12):1873–1881.

[Mazzucato, 1989] Mazzucato, E. (1989). Propagation of a gaussian beam in a nonhomogeneous plasma. *Physics of Fluids B: Plasma Physics*, 1:1855–1859.

[Michel et al., 2016] Michel, P., Rosenberg, M., Myatt, J., Solodov, A., Seka, W., Chapman, T., Hohenberger, M., Masse, L., Goyon, C., Turnbull, D., Regan, S., and Moody, J. D. (2016). Srs analyses of direct-drive icf experiments at the national ignition facility. In *APS Division of Plasma Physics Meeting Abstracts*, volume 2016 of *APS Meeting Abstracts*, page UO9.004.

[Mihalas and Mihalas, 1984] Mihalas, D. and Mihalas, B. W. (1984). *Foundations of radiation hydrodynamics*. Oxford University Press, New York [u.a.]. Literaturangaben.

[Miley et al., 1974] Miley, G. H., Towner, H., and Ivich, N. (1974). Fusion cross sections and reactivities.

[Montes and Hubbard, 1979] Montes, A. and Hubbard, M. (1979). Resonance absorption in non-planar plasmas. *Plasma Physics*, 21(10):885–894.

[Murakami and Nishi, 2017] Murakami, M. and Nishi, D. (2017). Optimization of laser illumination configuration for directly driven inertial confinement fusion. *Matter and Radiation at Extremes*, 2:55–68.

[Nuckolls et al., 1972] Nuckolls, J., Wood, L., Thiessen, A., and Zimmerman, G. (1972). Laser compression of matter to super-high densities: Thermonuclear (ctr) applications. *Nature*, 239:139–142.

[Olson et al., 2000] Olson, G. L., Auer, L. H., and Hall, M. L. (2000). Diffusion, p1, and other approximate forms of radiation transport. *Journal of Quantitative Spectroscopy and Radiative Transfer*, 64(6):619–634.

[Olson et al., 2012] Olson, R. E., Suter, L. J., Kline, J. L., Callahan, D. A., Rosen, M. D., Dixit, S. N., Landen, O. L., Meezan, N. B., Moody, J. D., Thomas, C. A., Warrick, A., Widmann, K., Williams, E. A., and Glenzer, S. H. (2012). X-ray conversion efficiency in vacuum hohlraum experiments at the national ignition facility. *Physics of Plasmas*, 19:053301.

[Phillips, 1999] Phillips, A. C. (1999). *The Physics of Stars*. The @Manchester physics series. John Wiley, Chichester, 2 edition. Includes bibliographical references (p. [241]-242] and index.

[Qinghong et al., 2011] Qinghong, Z., Wenbing, P., Juan, C., Heng, Y., and Chuanlei, Z. (2011). Radiation hydrodynamics code lared-h for laser fusion simulation.

[Radha et al., 2011] Radha, P. B., Betti, R., Boehly, T. R., Delettrez, J. A., Edgell, D. H., Goncharov, V. N., Igumenshchev, I. V., Knauer, J. P., Marozas, J. A., Marshall, F. J., McCrory, R. L., Meyerhofer, D. D., Regan, S. P., Sangster, T. C., Seka, W., Skupsky, S., Solodov, A. A., Stoeckl, C., Theobald, W., Frenje, J. A., Casey, D. T., Li, C. K., and Petrasso, R. D. (2011). Inertial confinement fusion using the omega laser system. *IEEE Transactions on Plasma Science*, 39(4):1007–1014.

[Radha et al., 2005] Radha, P. B., Collins, T. J. B., Delettrez, J. A., Elbaz, Y., Epstein, R., Glebov, V. Y., Goncharov, V. N., Keck, R. L., Knauer, J. P., Marozas, J. A., Marshall, F. J., McCrory, R. L., McKenty, P. W., Meyerhofer, D. D., Regan,

S. P., Sangster, T. C., Seka, W., Shvarts, D., Skupsky, S., Srebro, Y., and Stoeckl, C. (2005). Multidimensional analysis of direct-drive, plastic-shell implosions on omega. *Physics of Plasmas*, 12(5):056307.

[Regan et al., 2005] Regan, S. P., Marozas, J. A., Craxton, R. S., Kelly, J. H., Donaldson, W. R., Jaanimagi, P. A., Jacobs-Perkins, D., Keck, R. L., Kessler, T. J., Meyerhofer, D. D., Sangster, T. C., Seka, W., Smalyuk, V. A., Skupsky, S., and Zuegel, J. D. (2005). Performance of 1-thz-bandwidth, two-dimensional smoothing by spectral dispersion and polarization smoothing of high-power, solid-state laser beams. *Journal of the Optical Society of America B*, 22:998.

[Richtmyer, 1960] Richtmyer, R. D. (1960). Taylor instability in shock acceleration of compressible fluids. *Communications on Pure and Applied Mathematics*, 13(2):297–319.

[Ridgers et al., 2021] Ridgers, C. P., Arran, C., Bissell, J. J., and Kingham, R. J. (2021). The inadequacy of a magnetohydrodynamic approach to the biermann battery. *Philosophical Transactions of the Royal Society A: Mathematical, Physical and Engineering Sciences*, 379(2189):20200017.

[Robinson et al., 2014] Robinson, A. P. L., Strozzi, D. J., Davies, J. R., Gremillet, L., Honrubia, J. J., Johzaki, T., Kingham, R. J., Sherlock, M., and Solodov, A. A. (2014). Theory of fast electron transport for fast ignition. *Nuclear Fusion*, 54:054003.

[Rosen, 1999] Rosen, M. D. (1999). The physics issues that determine inertial confinement fusion target gain and driver requirements: A tutorial. *Physics of Plasmas*, 6(5):1690–1699.

[Rosenberg et al., 2018] Rosenberg, M., Solodov, A., Myatt, J., Seka, W., Michel, P., Hohenberger, M., Short, R., Epstein, R., Regan, S., Campbell, E., Chapman, T., Goyon, C., Ralph, J., Barrios, M., Moody, J., and Bates, J. (2018). Origins and scaling of hot-electron preheat in ignition-scale direct-drive inertial confinement fusion experiments. *Physical Review Letters*, 120.

[Ruyer et al., 2022] Ruyer, C., Loiseau, P., Riazuelo, G., Riquier, R., Debayle, A., and Masson-Laborde, P. E. (2022). Accounting for speckle scale beam-bending in classical ray tracing schemes for propagating realistic pulses in indirect drive ignition conditions. *arXiv e-prints*, page arXiv:2209.01035.

[Schwabl, 2006] Schwabl, F. (2006). *Statistical mechanics*. Springer-Verlag, Berlin, second edition edition. Literaturangaben.

[Scott et al., 2020] Scott, R., Barlow, D., Antonelli, L., Khan, M., Nutter, A., Glize, K., Arber, T., and Woolsey, N. (2020). Shock-augmented ignition. In *APS Division of Plasma Physics Meeting Abstracts*, volume 2020 of *APS Meeting Abstracts*, page GO09.010.

[Scott et al., 2021] Scott, R., Glize, K., Antonelli, L., Khan, M., Theobald, W., Wei, M., Betti, R., Stoeckl, C., Seaton, A., Arber, T., Barlow, D., Goffrey, T., Bennett, K., Garbett, W., Atzeni, S., Casner, A., Batani, D., Li, C., and Woolsey, N. (2021). Shock ignition laser-plasma interactions in ignition-scale plasmas. *Physical Review Letters*, 127.

[Seltzer and Berger, 1984] Seltzer, S. M. and Berger, M. J. (1984). Improved procedure for calculating the collision stopping power of elements and compounds for electrons and positrons. *The International Journal of Applied Radiation and Isotopes*, 35:665–676.

[Shashkov and Steinberg, 1996] Shashkov, M. and Steinberg, S. (1996). Solving diffusion equations with rough coefficients in rough grids. *Journal of Computational Physics*, 129(2):383–405.

[Shvarts et al., 2008] Shvarts, D., Smalyuk, V. A., Betti, R., Delettrez, J. A., Edgell, D. H., Glebov, V. Y., Goncharov, V. N., McCrory, R. L., McKenty, P. W., Meyerhofer, D. D., Marshall, F. J., Radha, P. B., Regan, S. P., Sangster, T. C., Seka, W., Skupsky, S., Stoeckl, C., Yaakobi, B., Frenje, J. A., Li, C. K., Petrasso, R. D., and Sĕguin, F. H. (2008). The role of fast-electron preheating in low-adiabat cryogenic implosions on omega. *Journal of Physics: Conference Series*, 112:022005.

[Skupsky et al., 1984] Skupsky, S., McCrory, R. L., Craxton, R. S., Delettrez, J., Epstein, R., Lee, K., and Verdon, C. (1984). Uniformity of energy deposition for laser driven fusion. In *Laser Interaction and Related Plasma Phenomena, Volume 6*, volume 6, page 751.

[Skupsky et al., 1989] Skupsky, S., Short, R. W., Kessler, T., Craxton, R. S., Letzring, S., and Soures, J. M. (1989). Improved laser-beam uniformity using the angular dispersion of frequency-modulated light. *Journal of Applied Physics*, 66:3456–3462.

[Smalyuk et al., 2005] Smalyuk, V. A., Goncharov, V. N., Boehly, T. R., Delettrez, J. A., Li, D. Y., Marozas, J. A., Maximov, A. V., Meyerhofer, D. D., Regan, S. P., and Sangster, T. C. (2005). Measurements of laser-imprinting sensitivity to relative beam mistiming in planar plastic foils driven by multiple overlapping laser beams. *Physics of Plasmas*, 12(7):072703.

[Solodov et al., 2016] Solodov, A. A., Yaakobi, B., Edgell, D. H., Follett, R. K., Myatt, J. F., Sorce, C., and Froula, D. H. (2016). Measurements of hot-electron temperature in laser-irradiated plasmas. *Physics of Plasmas*, 23(10):102707.

[Spencer, 2021] Spencer, S. J. (2021). *Particle-in-cell simulations of stimulated Raman scattering in the kinetic regime for direct-drive inertial confinement fusion*. PhD thesis, University of Warwick.

[Spitzer and Härm, 1953] Spitzer, L. j. and Härm, R. (1953). Transport phenomena in a completely ionized gas. *Physical Review, II. Series*, 89:977–981.

[Takabe et al., 1985] Takabe, H., Mima, K., Montierth, L., and Morse, R. L. (1985). Self-consistent growth rate of the rayleigh-taylor instability in an ablatively accelerating plasma. *Physics of Fluids*, 28(12):3676–3682.

[Temporal et al., 2001] Temporal, M., Jacquemot, S., Bonnet, L., and Decoster, A. (2001). A three-dimensional ray-tracing code dedicated to x-ray laser amplification simulation. *Physics of Plasmas*, 8:1363.

[Theaker and Gorder, 2013] Theaker, K. A. and Gorder, R. A. V. (2013). Hyper-riccati equations and integrable reductions permitting stationary solutions for complex hyperbolic field equations. *Appl. Math. Comput.*, 219(16):8525–8541.

[Treichel et al., 2017] Treichel, R., Luttmann, J., Morasch, V., Hoffmann, H.-D., Nicklaus, K., and Wührer, C. (2017). Highly-efficient, frequency-tripled nd:yag laser for spaceborne lidars. *Proceedings of International Conference on Space Optics*.

[Trkov et al., 2018] Trkov, A., Herman, M., and Brown, D. A. (2018). Evaluated nuclear data file, iaea (brookhaven national laboratory). Database.

[von Neumann and Richtmyer, 1950] von Neumann, J. and Richtmyer, R. D. (1950). A method for the numerical calculation of hydrodynamic shocks. *Journal of Applied Physics*, 21:232–237.

[Vu et al., 2012] Vu, H. X., DuBois, D. F., Myatt, J. F., and Russell, D. A. (2012). Hot-electron production and suprathermal heat flux scaling with laser intensity from the two-plasmon–decay instability. *Physics of Plasmas*, 19:102703.

[Walsh and Clark, 2021] Walsh, C. A. and Clark, D. S. (2021). Biermann battery magnetic fields in icf capsules: Total magnetic flux generation. *Physics of Plasmas*, 28:092705.

[Walsh et al., 2020] Walsh, C. A., Crilly, A. J., and Chittenden, J. P. (2020). Magnetized directly-driven icf capsules: increased instability growth from non-uniform laser drive. *Nuclear Fusion*, 60:106006.

[W.H.O, 2021] W.H.O (2021). Household air pollution and health. *World Health Organisation Report*.

[Wilkins, 1980] Wilkins, M. L. (1980). Use of artificial viscosity in multidimensional fluid dynamic calculations. *Journal of Computational Physics*, 36(3):281–303.

[Willi et al., 1981] Willi, O., Rumsby, P. T., and Duncan, C. (1981). Megagauss magnetic fields on laser irradiated spherical targets. *Optics Communications*, 37(1):40–44.

[Wilson et al., 1998] Wilson, D. C., Bradley, P., Hoffman, N. M., and Swenson, F. J. (1998). The development and advantages of beryllium capsules for the national ignition facility. *Physics of Plasmas*, 5(5):1953–1959.

[Xu et al., 2020] Xu, C., Kohler, T. A., Lenton, T. M., Svenning, J.-C., and Scheffer, M. (2020). Future of the human climate niche. *Proceedings of the National Academy of Sciences*, 117(21):11350–11355.

[Yaakobi et al., 2013] Yaakobi, B., Solodov, A. A., Myatt, J. F., Delettrez, J. A., Stoeckl, C., and Froula, D. H. (2013). Measurements of the divergence of fast electrons in laser-irradiated spherical targets. *Physics of Plasmas*, 20:092706.

[Zel'dovich and Raizer, 2012] Zel'dovich, Y. B. and Raizer, Y. P. (2012). Physics of shock waves and high-temperature hydrodynamic phenomena. Ursprüngliches Erscheinungsjahr: 1966/67.

[Zohuri, 2017] Zohuri, B. (2017). *Magnetic Confinement Fusion Driven Thermonuclear Energy*. Springer-Verlag GmbH, Cham, 1 edition.

[Zylstra et al., 2022] Zylstra, A. B., Hurricane, O. A., Callahan, D. A., Kritcher, A. L., Ralph, J. E., Robey, H. F., Ross, J. S., Young, C. V., Baker, K. L., Casey, D. T., Döppner, T., Divol, L., Hohenberger, M., Le Pape, S., Pak, A., Patel, P. K., Tommasini, R., Ali, S. J., Amendt, P. A., Atherton, L. J., Bachmann, B., Bailey, D., Benedetti, L. R., Berzak Hopkins, L., Betti, R., Bhandarkar, S. D., Biener, J., Bionta, R. M., Birge, N. W., Bond, E. J., Bradley, D. K., Braun, T., Briggs, T. M., Bruhn, M. W., Celliers, P. M., Chang, B., Chapman, T., Chen, H., Choate, C., Christopherson, A. R., Clark, D. S., Crippen, J. W., Dewald, E. L., Dittrich, T. R., Edwards, M. J., Farmer, W. A., Field, J. E., Fittinghoff, D., Frenje, J., Gaffney, J., Gatu Johnson, M., Glenzer, S. H., Grim, G. P., Haan, S., Hahn, K. D., Hall, G. N., Hammel, B. A., Harte, J., Hartouni, E., Heebner, J. E., Hernandez, V. J., Herrmann, H., Herrmann, M. C., Hinkel, D. E., Ho, D. D., Holder, J. P., Hsing, W. W., Huang, H., Humbird, K. D., Izumi, N., Jarrott, L. C., Jeet, J., Jones, O., Kerbel, G. D., Kerr, S. M., Khan, S. F., Kilkenny, J., Kim, Y., Geppert Kleinrath, H., Geppert Kleinrath, V., Kong, C., Koning, J. M., Kroll, J. J., Kruse, M. K. G., Kustowski, B., Landen, O. L., Langer, S., Larson, D., Lemos, N. C., Lindl, J. D., Ma, T., MacDonald, M. J., MacGowan, B. J., Mackinnon, A. J., MacLaren, S. A., MacPhee, A. G., Marinak, M. M., Mariscal, D. A., Marley, E. V., Masse, L., Meaney, K., Meezan, N. B., Michel, P. A., Millot, M., Milovich, J. L., Moody, J. D., Moore, A. S., Morton, J. W., Murphy, T., Newman, K., Di Nicola, J.-M. G., Nikroo, A., Nora, R., Patel, M. V., Pelz, L. J., Peterson, J. L., Ping, Y., Pollock, B. B., Ratledge, M., Rice, N. G., Rinderknecht, H., Rosen, M., Rubery, M. S., Salmonson, J. D., Sater, J., Schiaffino, S., Schlossberg, D. J., Schneider, M. B., Schroeder, C. R., Scott, H. A., Sepke, S. M., Sequoia, K., Sherlock, M. W., Shin, S., Smalyuk, V. A., Spears, B. K., Springer, P. T., Stadermann, M., Stoupin, S., Strozzi, D. J., Suter, L. J., Thomas, C. A., Town, R. P. J., Tubman, E. R., Trosseille, C., Volegov, P. L., Weber, C. R., Widmann, K., Wild, C., Wilde, C. H., Van Wonterghem, B. M., Woods, D. T., Woodworth, B. N., Yamaguchi, M., Yang, S. T., and Zimmerman, G. B. (2022). Burning plasma achieved in inertial fusion. *Nature*, 601:542–548.